Event Reconstruction in JUNO-TAO using Graph Convolutional Networks & Optimization of Horn Geometry in ESSnuSB+ using Genetic Algorithm

Dissertation
to obtain Doctoral Degree at the Faculty of Mathematics,
Informatics and Natural Sciences
Department of Physics
of the University of Hamburg

submitted by

Vidhya Hariharan

Hamburg
2025

Gutachter/innen der Dissertation:	Prof. Dr. Caren Hagner Dr. Daniel Bick
Zusammensetzung der Prüfungskommission:	Prof. Dr. Caren Hagner Prof. Dr. Dieter Horns Prof. Dr. Gudrid Moortgat-Pick Prof. Dr. Johannes Haller Dr. Daniel Bick
Vorsitzende/r der Prüfungskommission:	Prof. Dr. Dieter Horns
Datum der Disputation:	26.02.2025
Vorsitzender des Fach-Promotionsausschusses PHYSIK:	Prof. Dr. Wolfgang J. Parak
Leiter des Fachbereichs PHYSIK:	Prof. Dr. Markus Drescher
Dekan der Fakultät MIN:	Prof. Dr.-Ing. Norbert Ritter
Document Identifier:	urn:nbn:de:gbv:18-ediss-126929

Abstract

The primary goal of JUNO is to resolve the neutrino mass hierarchy using precision spectral measurements of reactor antineutrino oscillations. To achieve this goal a precise knowledge of the reactor spectrum is required. Since the existing reference spectra show a deficit in measured reactor fluxes, TAO, a ton-level, liquid scintillator detector with a baseline of 44 m, is set up as a reference detector to JUNO. With a set of 4024 Silicon Photomultipliers (SiPM) and an operating temperature at -50°C, TAO is expected to record about 2000 antineutrino events per day and aims to achieve a resolution of less than 2% at 1 MeV. For that, a precise reconstruction of the reactor antineutrino events is necessary. These events occur through the Inverse Beta Decay (IBD), producing a prompt positron and delayed neutron signal. Since positron events carry most of the energy, this thesis focuses on the vertex and energy reconstruction of positron events generated by the official TAO offline software. The reconstruction was carried out through Graph Convolutional Networks (GCNs). A graph, resembling the detector with 4024 nodes representing SiPMs with features, first hit time and hit counts was modeled. The model was trained and validated on 5 million events covering energies from 1-10 MeV. The final evaluation on the 1 MeV subset resulted in a vertex resolution of 8 mm and energy resolution of 1.8 %. Notably, both vertex and energy resolutions even increased for higher energies.

The ESSnuSB+ aims to precisely measure neutrino interaction cross sections below 600 MeV. The 2 GeV proton beam from the ESS hits the titanium target, resulting in a secondary hadron beam predominantly consisting of pions. The focusing of charged pions is done by the magnetic horns and is critical for generating intense neutrino beams. In this study, the horn is simulated using FLUKA and its configuration is optimized utilizing a Genetic Algorithm (GA). Dimensions of the horn like the lengths, radii, heights, and current were optimized for 50 generations, after which no significant improvement was observed. The fitness score, a measure of detection efficiency, improved from 0.725 to 0.860, resulting in a 20% increase in pion concentration, with the optimized horn configuration. This enhanced focusing will improve neutrino flux and precision in measurements of neutrino cross sections.

Zusammenfassung

Das Hauptziel von JUNO ist die Auflösung der Neutrinomassenhierarchie durch präzise Messung des Oszillationspektrums von Reaktor-Antineutrinos. Um dieses Ziel zu erreichen, ist allerdings eine genaue Kenntnis des unoszillierten Reaktorspektrums erforderlich. Da das vorhandene Referenzspektrum ein Defizit in den gemessenen Reaktorflüssen aufweist, wird das TAO-Experiment als Referenzdetektor für JUNO eingesetzt. TAO ist ein Flüssigszintillatordetektor im Tonnenbereich mit einem Abstand von $44\,\mathrm{m}$ zu einem Reaktor. Mit einer Anordnung aus 4024 Silizium-Photomultiplier (SiPMs) und einer Betriebstemperatur von $-50^\circ\,\mathrm{C}$ wird erwartet, dass TAO etwa 2000 Antineutrino-Ereignisse pro Tag messen wird mit einer gewünschten Energieauflösung von weniger als $2\,\%$ bei einem MeV Energie. Dafür ist eine präzise Rekonstruktion der Reaktor-Antineutrino-Ereignisse notwendig. Diese Ereignisse finden als Inverser Betazerfall statt, der ein promptes Positron- und ein verzögertes Neutronsignal zur Folge hat. Da die meiste Energie von den Positronen weggetragen wird, ist der Fokus dieser Arbeit die Energie- und Vertexrekonstruktion von Positronenereignssen, die von der offiziellen TAO offline Software generiert werden. Die Rekonstruktion wurde mithilfe von Graph Convolutional Networks (GCNs) durchgeführt. Der Graph besteht dabei aus 4024 Knoten, die die SiPMs repräsentieren, wobei jeder Knoten die Zeit des ersten Photontreffers und die Anzahl der Photontreffer als Eigenschaften hat. Das Modell wurde auf fünf Millionen Ereignisse mit Energien zwischen einem und zehn MeV trainiert und validiert. Die finale Evaluation auf dem $1\,\mathrm{MeV}$-Datensatz resultierte in einer Vertexauflösung von $8\,\mathrm{mm}$ und einer Energieauflösung von $1,8\,\%$, wobei sich beide Auflösungen für höhere Energien weiter verbesserten.

Das Experiment ESSnuSB+ zielt darauf ab, die Neutrino-Wechselwirkungsquerschnitte für unter $600\,\mathrm{MeV}$ zu messen. Dafür wird ein Strahl aus Protonen mit einer Energie von $2\,\mathrm{GeV}$ aus dem ESS auf ein Titaniumtarget gelenkt, wodurch ein sekundärer Strahl aus Hadronen, hauptsächlich Pionen, entsteht. Das Fokussieren dieser Pionen via Magnete (sogenannter magnetic horns) ist essentiell für einen intensiven Neutrinostrahl. In dieser Studie wird ein solcher Magnet mit FLUKA simuliert und seine Spezifikationen mithilfe von einem genetischen Algorithmus optimiert. Dabei wurden Größen wie Längen, Radien, Höhen und der elektrische Strom in 50 Generationen optimiert, nach denen keine weitere signifikante Verbesserung festgestellt werden konnte. Die Kenngröße für die Höhe der Detektionseffizienz konnte dabei von $0,725$ auf $0,860$ verbessert werden. Das entspricht einer Zunahme der Pionenkonzentration von $20\,\%$ mit der optimierten Magnetkonfiguration. Mit der verbesserten Fokussierung verbessert sich auch der Neutrinofluss und damit die Präzision für die Vermessung der Neutrino-Wechselwirkungsquerschnitte.

Contents

Contents I
1 Introduction 1
2 Neutrino Physics 3
2.1 Neutrinos in Standard Model 3
2.2 Neutrino Oscillation Theory 5
2.2.1 Neutrino Oscillations in Vacuum 5
2.2.2 Neutrino Oscillations in Matter 7
2.3 Mixing Parameters 10
2.4 Neutrino Sources 10
2.4.1 Solar 10
2.4.2 Atmospheric 13
2.4.3 Reactor 15
2.4.4 Accelerator 16
2.5 Open Questions 17
2.5.1 Nature of Neutrinos 17
2.5.2 Mass Ordering 17
2.5.3 CP Violating Phase 18
2.5.4 Sterile Neutrinos 19
3 Liquid Scintillator Experiments: JUNO & TAO 21
3.1 Physics of Liquid Scintillator Detectors 21
3.1.1 Primary Interaction 21
3.1.2 Emission, Propagation & Detection of Light 22
3.2 JUNO 25
3.3 Experimental Framework of TAO 27
3.3.1 Detector Layout 27
3.3.2 Signal & Background 31
3.4 Physics Goals 32
3.4.1 Fine Structure Measurement 33
3.4.2 Reference Spectrum for JUNO 34
3.4.3 Other Goals 35
4 Deep Learning and Genetic Algorithm 37
4.1 Deep Learning 37
4.1.1 Structure of Neural Networks 37
4.1.2 Key steps in Building Neural Networks 39
4.1.3 Layers in the Architecture 44
4.1.4 Role of GCN in Neutrino Event Reconstruction 48
4.2 Genetic Algorithm (GA) 48
4.2.1 Basic Structure of GA 48
4.2.2 Role of GA in Optimizing Horn Geometry 52

5 Event Reconstruction . . . 55
5.1 Simulation . . . 55
5.2 Data Generation . . . 59
5.3 Reconstruction . . . 60
5.3.1 Vertex Reconstruction . . . 61
5.3.2 Energy Reconstruction . . . 70
6 Optimization of Horn Geometry in ESSnuSB+ . . . 75
6.1 Physics Motivation . . . 75
6.2 Experimental Layout . . . 79
6.3 Motivation to Optimize Horn Geometry . . . 82
6.4 Implementation of GA . . . 83
6.4.1 Work Flow . . . 84
6.4.2 Definition of Individuals . . . 84
6.4.3 Evaluation & Propagation of Individuals . . . 86
6.4.4 Optimization results . . . 87
7 Results and Conclusions . . . 91
List of Figures . . . 97
List of Tables . . . 103
List of Abbreviations . . . 105
Bibliography . . . 107
Declaration on oath . . . 121

1 Introduction

Neutrinos are the elusive and light elementary particles that interact via weak force. Since their first proposal in 1930 [1] to explain the continuous energy spectrum and the conservation of angular momentum in β-decays, neutrinos have fascinated researchers. They were experimentally confirmed in 1956 by the Cowan-Reines Neutrino Experiment [2]. The confirmation later led to thre discovery the Solar Neutrino problem in the 1960s as a discrepancy was noticed between the measured and predicted solar neutrino flux. The discrepancy was later settled by the experimental evidence of neutrinos oscillations as observed by the Sudbury Neutrino Observatory (SNO) [3] and the Super-Kamiokande [4]. It was discovered that neutrinos oscillate between their three detected flavors—electron, muon, and tau—a discovery which won the Nobel Prize in 2015 [5].

Following the confirmation of neutrino oscillations, numerous experiments have been conducted to precisely measure them with great success. However, many questions in the field of neutrino physics remain unanswered, such as nature of neutrinos, Neutrino Mass Ordering (NMO) and Charge Parity Violation (CPV). The main objective of the Jiangmen Underground Neutrino Observatory (JUNO) [6] experiment is to determine the NMO with $3\,\sigma$ significance over six years, focusing primarily on measuring vacuum neutrino oscillations [7]. To achieve this goal, JUNO uses a 20 kton liquid scintillator detector to measure the electron anti-neutrino flux from two nuclear power plants, located at 53 km baseline. Monitored by 17,612 large 20" and 25,600 small 3"-Photomultiplier Tubes (PMTs), it aims for an energy resolution of about 3 % at 1 MeV. For this level of precision, a precise knowledge of the reactor neutrino flux is crucial. A reference spectrum can be provided by the existing reactor antineutrino experiments like Daya Bay [7], RENO [8] and Double CHOOZ [9]. However, the obtained reactor neutrino spectrum reveal an approximate 3 % deficit in measured reactor fluxes. Additionally, data from experiments demonstrate an unexplained excess in the neutrino flux from 5 MeV to 6 MeV. This unreliable nature of the model predictions for the reactor neutrino flux demands an additional detector for JUNO to measure the flux near the source. Hence a reference detector, Taishan Antineutrino Observatory (TAO) [10] is set up at 44 m from the reactor core (4.6 GW) to provide the benchmark spectrum for JUNO. TAO uses 2.8 tons of gadolinium-doped liquid scintillator, and a set of 4024 SiPM resulting in a photoelectron yield of about 4500/MeV. The detector operates at -50°C to minimize the dark noise of the SiPMs and is expected to record roughly 2000 antineutrino emissions per day. The TAO experiment should surpass JUNO's resolution to serve as an effective reference detector. With a resolution of less than 2% at 1 MeV, TAO will be able to resolve the fine spectral structures and reduce the dependence on theoretical models in JUNO's

analysis. To achieve this resolution a precise reconstruction of the neutrino events is essential. Such an event consists of a neutrino interacting with the detector via IBD resulting in a prompt signal from the positron and a delayed signal from the neutron. Since the positron carries most of the energy and is well-suited to find the event's vertex, this thesis focuses solely on positron events. The position and energy of these positron events are reconstructed via GCNs resembling the detector topography. A graph containing 4024 nodes with each node having information of first hit time and number of hits was developed. The network was trained and evaluated on five million events generated from the TAO offline software. The results were compared with the center of charge method as mentioned in [10].

The other experiment that is studied in this thesis is the European Spallation Source neutrino Super Beam+ (ESSnuSB+) which aims to precisely measure neutrino interaction cross sections below 600 MeV, to aid the European Spallation Source neutrino Super Beam (ESSnuSB) to measure the leptonic CPV at the second oscillation maximum. It utilizes the European Spallation Source (ESS), a powerful neutron facility, designed to operate at 5 MW and is under construction in Lund, Sweden[11]. The high-energy proton beam from the ESS hits the titanium target, resulting in a secondary hadron beam predominantly consisting of pions. The focusing of charged pions is done by the magnetic horns and is critical for generating intense neutrino beams, that is essential for measuring neutrino interaction cross sections. In this study, the horn is simulated using FLUKA [12] to provide the pion profile corresponding to each horn configuration. The configuration is optimized over fifty generation utilizing a genetic algorithm. The optimization process was terminated as no further improvement was observed. The final horn configuration produced a denser pion profile as compared to the initial configuration.

The thesis is structured as follows. Chapter 2 introduces the fundamentals of neutrino physics, highlighting the key discoveries made and addressing open questions that currently exist in the field. Chapter 3 follows, and introduces the JUNO and TAO experiments. It highlights the benefits of having TAO as JUNO's reference detector and discusses the experimental setup and the potential physics goals of the TAO experiment. Chapter 4 is the introduction to deep learning and the genetic algorithm. It covers the basics and specific techniques utilized in this study. The implementation of deep learning methods to reconstruct events in the TAO detector is explained in Chapter 5. It describes the simulation involved, the data generated and the analysis using deep learning tools. Following this is chapter 6 giving a concise introduction to the ESSnuSB+ experiment and its physics goals. The chapter then shows the implementation of genetic algorithm to optimize the horn geometry of the ESSnuSB+ experiment. The obtained results of both studies are discussed in chapter 7, drawing conclusions and outlining future research directions.

2 Neutrino Physics

Neutrinos are the second most abundant particles in the universe after photons but detecting them is challenging due to their weak interactions with matter. From the building of the neutrino hypothesis to its experimental confirmation, and to the discovery of the phenomenon of neutrino oscillations, much has been learned about neutrinos. This chapter provides a brief overview of the current understanding of neutrinos. In section 2.1, a brief overview of the Neutrinos in the Standard Model (SM) is presented, and in section 2.2, the theoretical description of neutrino oscillations. In section 2.3 the experimental observations of neutrino oscillation, other key historical development and current state are discussed. Lastly, section 2.5 provides a brief review of some open questions in the neutrino sector and discusses ongoing and future experimental activities.

2.1 Neutrinos in Standard Model

Neutrinos are matter particles within SM [13] of particle physics, and come in three generations. The SM is a gauge theory with local symmetry group $SU(3)SU(2) \times U(1)$ [14]. This gauge group determines how particles interact and the number of gauge bosons representing the carriers of the interactions. It is built of three components, $SU(3)$ describes Quantum Chromodynamics (QCD), the theory of strong interactions, exchanged by eight gluons, $SU(2) \times U(1)$ describes electroweak interactions with $SU(2)$ responsible for W_1, W_2, W_3 bosons and $U(1)$ for B boson. The W_1 and W_2 mix to form the charges bosons W^+ and W^- bosons. W_3 and B mix to form Z^0 boson and γ. Figure 1 shows the fundamental particles in the SM that are comprised of quarks, leptons and bosons. Quarks and leptons are grouped in three generations, and classified as fermions having a spin 1/2. Quarks appear in six flavors and take part in all three interactions described in the SM. Charged leptons, electrons, muons and taus interact via electromagnetic and weak forces. There are also three flavors of neutrinos corresponding to charged leptons: electron, muon and tau neutrinos. Neutrinos interact through weak force. The gauge bosons are fundamental particles that act as force carriers for fermions. They are photons (for electromagnetism), gluons (for the strong force) and W and Z bosons (for the weak force). All gauge bosons have spin 1. The SM has also a scalar boson, the so-called Higgs boson, that is responsible for giving masses to weak bosons and to fermions through the well-known Higgs mechanism [15] [16].

Neutrinos in the SM are electrically neutral, spin$-\frac{1}{2}$ Dirac fermions with zero mass and no color charge, therefore, they only interact through the Charged Current (CC)

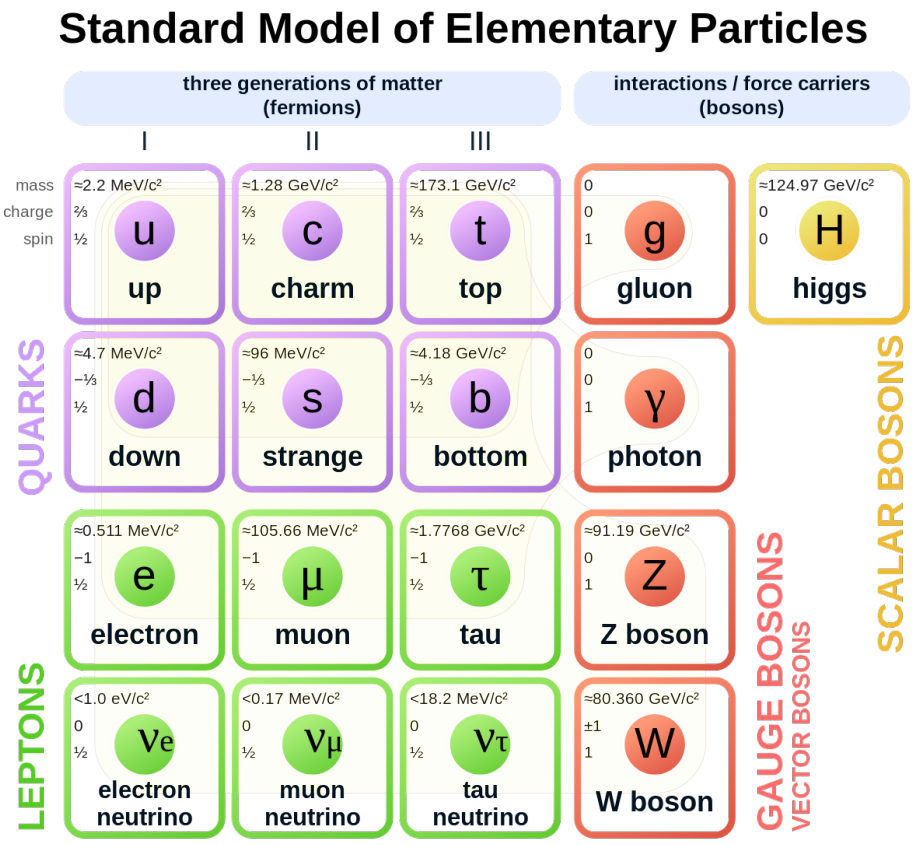

Figure 1: A schematic view of the Standard model that illustrates elementary particles and their interactions [17].

and the Neutral Current (NC) of the weak force, which are mediated by the massive bosons $W^{\pm}$ ($m_W = 80.4\,\text{GeV}$) and Z^0 ($m_Z = 91.2\,\text{GeV}$), respectively [18]. The three neutrinos are the counterparts of the three charged leptons e, μ and τ, which define the so-called flavor of a neutrino (ν) and its antiparticle ($\overline{\nu}$): ν_e ($\overline{\nu}_e$), ν_μ ($\overline{\nu}_\mu$) and ν_τ ($\overline{\nu}_\tau$). A neutrino ν_l being of the Lorentz invariant flavor associated with the charged lepton $l = e, \mu, \tau$ is produced from l^- or together with l^+ in a CC weak interaction. The opposite holds for the antineutrino $\overline{\nu}_l$. According to the chiral V-A theory, only the left-handed component of a neutrino or the right-handed component of an antineutrino interact weakly [19]. Because the chirality of neutrinos matches their helicity, the SM includes only left-handed neutrinos with negative helicity and right-handed antineutrinos with positive helicity. This means that the standard Higgs mechanism, which needs a change in handedness to generate masses, doesn't apply to neutrinos within the SM.

In contrast to the previously mentioned characteristics of neutrinos in the SM, experimentally observed neutrino flavour transformation indicate that neutrinos possess mass. These oscillations arise from the non-zero masses of neutrinos and the mixing between different mass and flavor eigenstates. To account for neutrino masses, ex-

tensions to the SM are being explored. Even after discovering neutrino oscillations, many aspects of neutrinos remain mysteries. Key questions include their absolute mass scale, mass ordering, whether they are Dirac or Majorana particles, and the extent of CP-violation in their mixing. These topics are subsequently discussed in section 2.5.

2.2 Neutrino Oscillation Theory

Although it was long thought that neutrinos were massless, early theoretical work attempted to describe massive neutrinos and study neutrino mixing and oscillation. The idea of masses, mixing, and oscillations for neutrinos was proposed by Bruno Pontecorvo in 1957 with analogies of leptons and hadrons, suggesting oscillations similar to the $K^0 \rightleftharpoons \overline{K^0}$ system [20]. The similarity between the$K^0 \rightleftharpoons \overline{K^0}$ system and neutrino oscillations is that they involve flavor transformation of particles, known as flavor mixing. Initially, with only one type of neutrino, oscillations were limited to neutrinos and antineutrinos. After the discovery of the muon-neutrino, Pontecorvo developed this concept into two neutrinos [21]. This groundbreaking idea predated the phenomenon of solar neutrino oscillations, which was subsequently confirmed through the Homestake experiment at the end of 1960 [22]. Pontecorvo together with V. Gribov later introduced the first phenomenological theory of two-neutrino mixing in 1969. Apart from that, in 1962, Z. Maki, M. Nakagawa, and S. Sakata introduced the theory of two neutrino mixing by defining "true neutrinos" ν_1 and ν_2 as combinations of ν_e and ν_μ. This led to the Pontecorvo, Maki, Nakagawa, and Sakata (PMNS) Pontecorvo, Maki, Nakagawa, and Sakata (PMNS) [23]. So far, the theory of three neutrino oscillation has been both experimentally and theoretically well explored and confirmed [24]–[30]. However, some aspects are still to be understood.

2.2.1 Neutrino Oscillations in Vacuum

Under the assumption [31], [32] of two mass eigenstates, ν_1 and ν_2, having masses m_1 and m_2 and flavour states ν_e and ν_μ, the connection between flavor and mass eigenstates can be described by

$$\begin{bmatrix} \nu_e \\ \nu_\mu \end{bmatrix} = \begin{bmatrix} \cos\theta & \sin\theta \\ -\sin\theta & \cos\theta \end{bmatrix} \begin{bmatrix} \nu_1 \\ \nu_2 \end{bmatrix}. \tag{2.1}$$

The evolved neutrino state at a certain time t can be expressed as

$$|\nu(t)\rangle = \cos\theta|\nu_1(0)\rangle e^{-iE_1 t} + \sin\theta|\nu_2(0)\rangle e^{-iE_2 t} \tag{2.2}$$

where $|\nu_1(0)\rangle$ and $|\nu_2(0)\rangle$ are the neutrino states at time $t = 0$ and E_1 and E_2 are the energy of the mass eigenstates. Therefore the time-evolved state projected onto ν_e and ν_μ can be derived as follows

$$\begin{aligned}\langle\nu_e|\nu(t)\rangle &= \cos\theta\langle\nu_e|\nu_1(0)\rangle e^{-iE_1t} + \sin\theta\langle\nu_e|\nu_2(0)\rangle e^{-iE_2t} \\ &= \cos^2\theta e^{-iE_1t} + \sin^2\theta e^{-iE_2t}\end{aligned} \tag{2.3}$$

$$\begin{aligned}\langle\nu_\mu|\nu(t)\rangle &= \cos\theta\langle\nu_\mu|\nu_1(0)\rangle e^{-iE_1t} + \sin\theta\langle\nu_\mu|\nu_2(0)\rangle e^{-iE_2t} \\ &= \cos\theta\sin\theta(e^{-iE_2t} - e^{-iE_1t}).\end{aligned} \tag{2.4}$$

Hence the probability of observing ν_μ after time t is

$$|\langle\nu_\mu|\nu(t)\rangle|^2 = \sin^2 2\theta \sin^2\left(\frac{(E_2 - E_1)t}{2}\right). \tag{2.5}$$

The energy mass eigenstate of neutrinos can be approximated as $E_i = p_i^2 + \frac{m_i^2}{2p_i}$ where p_i and m_i are the momentum and mass of the i-th eigenstate respectively. The two mass eigenstates may have differing momenta, but approximating their momenta as equal yields a qualitatively similar expression for the probability. Thus, it can be assumed that the neutrino momentum is $p = p_1 = p_2$. Neglecting neutrino mass relative to momentum implies $E = p$. Hence, $(E_2 - E_1) = \frac{m_2^2 - m_1^2}{2E} = \frac{\Delta}{2E}$. Given the ultra-relativistic nature of neutrinos, $t = L/c \sim L$, where $'L'$ is the source-detector distance and $'c'$ is the neutrino velocity close to the speed of light in vacuum. Consequently, the probability of detecting ν_μ after time t, starting from an initial state of ν_e, can be expressed as

$$P_{e\mu} = \sin^2 2\theta \sin^2\left(\frac{\Delta L}{4E}\right). \tag{2.6}$$

Hence from equation (2.6) to observe a neutrino oscillation the masses of the eigenstates have to be different, and the probability of oscillation heavily depends on the factor $\frac{\Delta L}{4E}$.

With the discovery of ν_τ the two flavour oscillation was extended to a three flavour formalism with three mass eigenstates ν_1, ν_2, ν_3 having masses m_1, m_2, m_3 and flavour eigenstates ν_e, ν_μ and ν_τ respectively. This results in a 3×3 unitary matrix which is a linear superposition between the mass and flavour eigenstates represented as

$$\begin{bmatrix}\nu_e \\ \nu_\mu \\ \nu_\tau\end{bmatrix} = U \begin{bmatrix}\nu_1 \\ \nu_2 \\ \nu_3\end{bmatrix}, \tag{2.7}$$

where U is the PMNS matrix that is parameterized as

$$U = \underbrace{\begin{bmatrix} 1 & 0 & 0 \\ 0 & c_{23} & s_{23} \\ 0 & -s_{23} & c_{23} \end{bmatrix}}_{\text{atmospheric}} \underbrace{\begin{bmatrix} c_{13} & 0 & s_{13}e^{-i\delta_{CP}} \\ 0 & 1 & 0 \\ -s_{13}e^{i\delta_{CP}} & 0 & c_{13} \end{bmatrix}}_{\text{reactor}} \underbrace{\begin{bmatrix} c_{12} & s_{12} & 0 \\ -s_{12} & c_{12} & 0 \\ 0 & 0 & 1 \end{bmatrix}}_{\text{solar}} \tag{2.8}$$

where δ_{CP} represents the CP violating phase. The three regimes in the matrix are named after the primary neutrino sources used to determine the mixing angles within each regime. The 3 $\times$ 3 unitary matrix requires nine parameters. Within these parameters, three represent mixing angles (θ_{12}, θ_{13}, θ_{23}), while the remaining six are phases. Among these phases, five phases can be absorbed into the neutrino flavor eigenstates (ν_e, ν_μ, ν_τ) through a process called 'rephasing', leaving one as the Dirac CP-violating phase, δ_{CP}. In the scenario where neutrinos behave as Dirac particles, experimental measurements can solely access the Dirac CP-violating phase δ_{CP}. However, if neutrinos exhibit Majorana properties, along with δ_{CP}, two additional phases can be observed. This is explained in section 2.5.1.

The oscillation probability from ν_α to ν_β can be written as

$$\begin{aligned} P_{\alpha\beta} = \delta_{\alpha\beta} - 4\sum_{i>j} Re(U^*_{\alpha i}U_{\beta i}U_{\alpha j}U^*_{\beta j}) \sin^2\left(\frac{\Delta_{ij}L}{4E}\right) \\ +2\sum_{i>j} Im(U^*_{\alpha i}U_{\beta i}U_{\alpha j}U^*_{\beta j}) \sin^2\left(\frac{\Delta_{ij}L}{2E}\right). \end{aligned} \tag{2.9}$$

If $\alpha = \beta$ then $P_{\alpha\beta}$ denotes survival probability. For antineutrinos, all $U_{\alpha i}$ are replaced by their complex conjugate. With the knowledge of the energy and path length, one can find the oscillation or the survival probability using equation (2.9).

2.2.2 Neutrino Oscillations in Matter

When neutrinos traverse through dense mediums such as the sun or the earth's core, they undergo coherent forward scattering with particles they encounter on the way. Consequently, the likelihood of oscillation can deviate from what is observed in a vacuum. This interaction gives rise to an additional potential term in the neutrino Hamiltonian which was identified by Mikhaev, Smirnov, and Wolfenstein (MSW) [33]. The MSW effect arises from the distinct interactions ν_e (and $\overline{\nu_e}$) in comparison to other neutrino flavors within matter as it propagates through it. While ν_e can engage in both CC and NC elastic scattering with electrons, ν_μ or ν_τ solely undergo NC interactions with electrons. For two flavor oscillations, the potential in flavor basis

can be written as following

$$\begin{aligned} V &= \begin{bmatrix} V_{CC+NC} & 0 \\ 0 & V_{NC} \end{bmatrix} \\ &= V_{NC} I + \begin{bmatrix} V_{CC} & 0 \\ 0 & 0 \end{bmatrix} \end{aligned} \tag{2.10}$$

where I is a 2×2 identity matrix. The diagonal terms in the matrix represent the matter potential experienced by the neutrino, where V_{NC} represents the NC potential, which is the same for all neutrinos and V_{CC} represents the CC potential experienced only by ν_e. The potential term V_{NC} is proportional to the identity matrix and is the same for both flavours because the NC interaction for ν_e and ν_μ is the same, hence it is neglected in oscillation probability expressions. In vacuum, the two flavour propagation can be expressed as

$$i\frac{d}{dt}\begin{bmatrix} \nu_1 \\ \nu_2 \end{bmatrix} = \left(p + \frac{(m_1^2 + m_2^2)}{4E} \right) I + \frac{1}{4E} \begin{bmatrix} -\Delta & 0 \\ 0 & \Delta \end{bmatrix} \begin{bmatrix} \nu_1 \\ \nu_2 \end{bmatrix} \tag{2.11}$$

where $\Delta = m_2^2 - m_1^2$. The terms related to the identity matrix represents the common phase factor. It affects both the mass eigenstates equally therefore does not contribute to the phase difference between the mass eigenstates, which is basically the driving force of neutrino flavor oscillations [34]. Hence this term is dropped. Following equation (2.1)

$$\begin{aligned} i\frac{d}{dt}\begin{bmatrix} \cos\theta & -\sin\theta \\ \sin\theta & \cos\theta \end{bmatrix}\begin{bmatrix} \nu_e \\ \nu_\mu \end{bmatrix} &= \frac{1}{4E}\begin{bmatrix} -\Delta & 0 \\ 0 & \Delta \end{bmatrix}\begin{bmatrix} \cos\theta & -\sin\theta \\ \sin\theta & \cos\theta \end{bmatrix}\begin{bmatrix} \nu_e \\ \nu_\mu \end{bmatrix} \\ i\frac{d}{dt}\begin{bmatrix} \nu_e \\ \nu_\mu \end{bmatrix} &= \frac{1}{4E}\begin{bmatrix} -\Delta\cos 2\theta & \Delta\sin 2\theta \\ \Delta\sin 2\theta & \Delta\cos 2\theta \end{bmatrix}\begin{bmatrix} \nu_e \\ \nu_\mu \end{bmatrix}. \end{aligned} \tag{2.12}$$

Adding the potential term to equation (2.8) results in

$$i\frac{d}{dt}\begin{bmatrix} \nu_e \\ \nu_\mu \end{bmatrix} = \frac{1}{4E}\begin{bmatrix} -\Delta cos2\theta + A & \Delta sin2\theta \\ \Delta sin2\theta & \Delta cos2\theta - A \end{bmatrix}\begin{bmatrix} \nu_e \\ \nu_\mu \end{bmatrix} \tag{2.13}$$

where $A = 2EV_{CC}$ is the Wolfenstein matter term. For an electroweak model [35]

$$A = 2\sqrt{2}G_F N_e E = 0.76 \times 10^4 \rho E(\mathrm{GeVg/cm^3}) \tag{2.14}$$

where G_F is Fermi constant for weak interaction and N_e is the electron density in matter. The vacuum mass (Δ) is replaced by the mass eigenstates of the effective mass matrix in a medium ($\Delta^m = \sqrt{(\Delta cos2\theta - A)^2 + (\Delta sin2\theta)}$) and the vacuum mixing angle (θ) is replaced by the effective mixing angle in matter ($\theta^m = \frac{1}{2}\tan^{-1}\frac{\Delta sin2\theta}{\Delta cos2\theta - A}$) [36]. Therefore, the oscillation probability of neutrinos in a medium is given by

$$P_{e\mu}^m = sin^2 2\theta^m sin^2\left(\frac{\Delta^m L}{2E}\right) \tag{2.15}$$

.

This can be extended to a three flavour oscillation scenario. The Hamiltonian in mass eingenbasis in vacuum ignoring the momentum term is

$$H_{vacuum}^{mass} = \frac{1}{2E}\begin{bmatrix} m_1^2 & 0 & 0 \\ 0 & m_2^2 & 0 \\ 0 & 0 & m_3^2 \end{bmatrix} \tag{2.16}$$

and the corresponding in flavour basis is

$$H_{vacuum}^{flavour} = U H_{vacuum}^{mass} U^{\dagger} = U M^2 U^{\dagger} \tag{2.17}$$

The Hamiltonian in the presence of a matter is

$$H_{matter}^{flavour} = H_{vacuum}^{flavour} + V_{matter}^{flavour} = \frac{1}{2E}(U M^2 U^{\dagger} + A) \tag{2.18}$$

$$A = \begin{bmatrix} 2\sqrt{2}G_F N_e E & 0 & 0 \\ 0 & 0 & 0 \\ 0 & 0 & 0 \end{bmatrix}. \tag{2.19}$$

For antineutrinos the potential term is negative. The modified PMNS matrix is as follows

$$U = \begin{bmatrix} \cos\theta_{13}^m & 0 & \sin\theta_{13}^m \\ -\sin\theta_{23}\sin\theta_{13}^m e^{i\delta_{CP}} & \cos\theta_{23} & \sin\theta_{23}\cos\theta_{13}^m e^{i\delta_{CP}} \\ -\cos\theta_{23}\sin\theta_{13}^m e^{i\delta_{CP}} & -\sin\theta_{23} & \cos\theta_{23}\cos\theta_{13}^m e^{i\delta_{CP}} \end{bmatrix} \tag{2.20}$$

where

$$tan2\theta_{13}^m = \frac{\Delta_{31} sin2\theta_{13}}{\Delta_{31} cos2\theta_{13} - A} \tag{2.21}$$

Therefore the oscillation probability is

$$P_{\mu e}^m = sin^2 2\theta_{23} sin^2 2\theta_{13}^m sin^2\left(\frac{1.27\Delta_{31}^m L}{E}\right) \tag{2.22}$$

where

$$\Delta_{31}^m = \sqrt{(\Delta_{31} cos2\theta_{13} - A)^2 + (\Delta_{31} sin2\theta_{13})^2} \tag{2.23}$$

Where $m_3 \gg m_1$, it is termed as Normal Hierarchy (NH). Conversely, if $m_1 \gg m_3$, it is Inverted Hierarchy (IH). Therefore matter effects can help in determining neutrino mass ordering. Depending on the matter density and the neutrino energy, the MSW potential can enhance the conversion between neutrino flavors, leading to a much larger oscillation probability in matter than in vacuum.

The neutrino mixing parameters, mixing angles and mass squared differences affect the oscillation probabilities. Hence, it is crucial to measure these parameters in order to understand neutrinos. Numerous neutrino experiments have been conducted, playing a significant role in enhancing our comprehension of mixing parameters. The following section has detailed explanations on this.

2.3 Mixing Parameters

The PMNS matrix as shown in equation (2.8) is the central component that describes the neutrino mixing and oscillations. The PMNS parameters are measured in different neutrino experiments targeting the solar, reactor, atmospheric, and accelerator neutrino sectors [37]. Solar neutrino experiments are sensitive to θ_{12} and Δm^2_{21}. Atmospheric neutrino experiments are sensitive to θ_{23} and Δm^2_{32} or Δm^2_{31}. Reactor neutrino experiments are sensitive to θ_{13} and Δm^2_{32} or Δm^2_{31}. Accelerator (beam) neutrino experiments can also measure θ_{23}, θ_{13}, and the CP-violating phase δ_{CP}. The sections that follow go over each sector's contribution to the current global best-fit values shown in table 1 as described in [38]. Global fits have been able to constrain neutrino mixing angles θ_{12}, θ_{23}, θ_{13}, and the mass squared difference Δm^2_{21} for both Normal Ordering (NO) and Inverted Ordering (IO), with very similar values. However, a positive Δm^2_{3l} points towards Normal Ordering, while a negative Δm^2_{3l} indicates Inverted Ordering. The uncertainties on these values hinder in a definite determination about the mass hierarchy. Also, there is a large uncertainty in the CP-violating phase, δ_{CP}, spanning almost 100°–360° range. These uncertainties outline the precision required from future measurements to determine both mass hierarchy and δ_{CP}.

2.4 Neutrino Sources

2.4.1 Solar

An important field of neutrino physics that has been thoroughly investigated through several experiments is the solar neutrino sector. Solar neutrinos travel from the sun's core to the earth, covering a distance of approximately 1 AU (150 million km). The energy spectrum of solar neutrinos spans from a few hundred keV to roughly 15 MeV [40].

Solar neutrinos originate from the nuclear fusion reactions that fuel the sun. The fusion of hydrogen to helium occurs through two distinct sets of nuclear reactions: the prevalent proton-proton (pp) chain and the CNO cycle. Since hydrogen has only protons while helium has both protons and neutrons, pp chain involves conversion of protons into neutrons and hence emitting neutrinos. As illustrated in figure 2 the majority of solar neutrinos originate from the initial production of deuterium through the reaction, $p + p \rightarrow 2H + e^+ + \nu$ (pp neutrinos), which have very low energy, less than 0.42 MeV [41]. Since many neutrino detection methods cannot detect such low-energy neutrinos, most experiments focus on the higher energy Be-7 and B-8 neutrinos produced in the pp-II and pp-III side chains. Although the pep and hep neutrinos also have high energies, they are very rare.

	Normal Ordering (best fit)		Inverted Odering ($\Delta\chi^2 = 9.1$)	
	$\pm$ 1σ	3σ range	bfp $\pm$ 1σ	3σ range
$sin^2\theta_{12}$	$0.308^{+0.012}_{-0.011}$	$0.275 \rightarrow 0.345$	$0.308^{+0.012}_{-0.011}$	$0.275 \rightarrow 0.345$
$\theta_{12}/^\circ$	$33.68^{+0.73}_{-0.70}$	$31.63 \rightarrow 35.95$	$33.68^{+0.73}_{-0.70}$	$31.63 \rightarrow 35.95$
$sin^2\theta_{23}$	$0.470^{+0.017}_{-0.013}$	$0.435 \rightarrow 0.585$	$0.550^{+0.012}_{-0.015}$	$0.440 \rightarrow 0.584$
$\theta_{23}/^\circ$	$43.3^{+1.0}_{-0.8}$	$41.3 \rightarrow 49.9$	$47.9^{+0.7}_{-0.9}$	$41.5 \rightarrow 49.8$
$sin^2\theta_{13}$	$0.02215^{+0.00056}_{-0.00058}$	$0.02030 \rightarrow 0.0238$	$0.02231^{+0.00056}_{-0.00056}$	$0.02060 \rightarrow 0.0240$
$\theta_{13}/^\circ$	$8.56^{+0.11}_{-0.11}$	$8.19 \rightarrow 8.89$	$8.59^{+0.11}_{-0.11}$	$8.25 \rightarrow 8.93$
$\delta_{CP}/^\circ$	212^{+26}_{-41}	$124 \rightarrow 364$	274^{+22}_{-25}	$201 \rightarrow 335$
$\frac{\Delta m^2_{21}}{10^{-5}eV^2}$	$7.49^{+0.19}_{-0.19}$	$6.92 \rightarrow 8.05$	$7.49^{+0.19}_{-0.19}$	$6.92 \rightarrow 8.05$
$\frac{\Delta m^2_{3l}}{10^{-3}eV^2}$	$+2.513^{+0.021}_{-0.019}$	$+2.451 \rightarrow +2.578$	$+2.484^{+0.020}_{-0.020}$	$-2.547 \rightarrow -2.421$

Table 1: Oscillation parameters obtained via nu-fit in September 2024 using Super Kamiokande atmospheric data for three flavor neutrino mixing. The best fit point (bfp) is the parameter value of those providing the best fit of models to data and the $s\sigma$ range is the range about this where we expect true parameter values will lie with around 99.7% confidence. It should be noted that for NO, $\Delta m^2_{3l} \equiv \Delta m^2_{31} > 0$, while for IO, $\Delta m^2_{3l} \equiv \Delta m^2_{32} < 0$ [39].

One of the first experiments in solar neutrinos was the Homestake experiment, which was performed by Ray Davis [42] through the chlorine capture reaction $^{37}\mathrm{Cl} + \nu_e \rightarrow ^{37}\mathrm{Ar} + e^-$. The reaction sensitive to electron-neutrinos with energies higher than 0.814 MeV, detected primarily Be-7 and B-8 neutrinos. However, the experiment famously observed only about one-third of the expected number of neutrinos, giving rise to the Solar Neutrino Problem in the 1970s. Later the Kamiokande Experiment [43], headed by Masatoshi Koshiba, utilized a water Cherenkov detector in Japan to achieve the successful observation of solar neutrinos in 1989. However, the observed flux was approximately half of the predicted value, thereby confirming the existence of the solar neutrino problem. Experiments using gallium in a radiochemical setup such as SAGE [44] in the Caucasus mountains and GALLEX[45] in the Gran Sasso tunnel were active in the 1990s. They published their first results, revealing a deficit in the detection of lower energy pp neutrinos compared to predictions from the standard solar model. During the 1990s and 2000s, the Super-Kamiokande [24], a sizable wa-

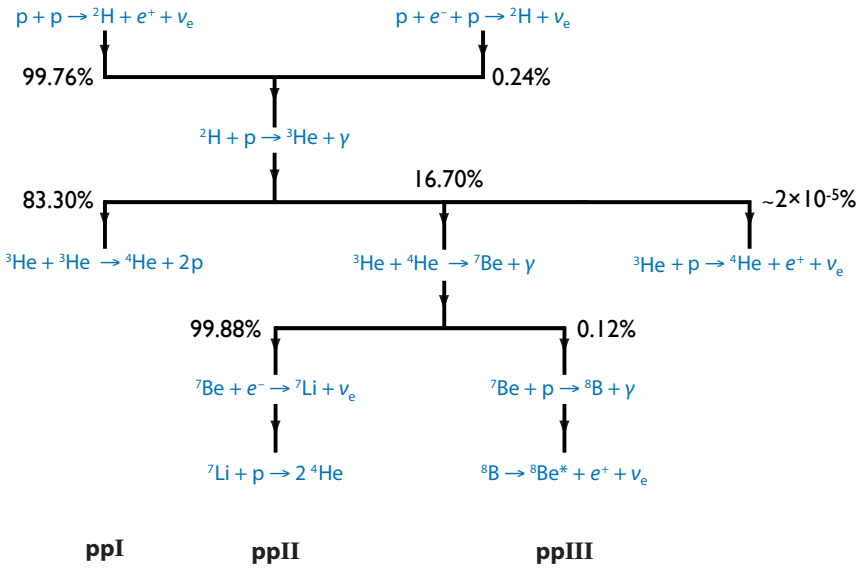

Figure 2: The pp chain is illustrated, outlining the primary branches and their respective distribution ratios. Neutrinos released in this sequence of reactions are identified as pp (stemming from the reaction at the upper left), Be-7 (in the pp II branch), B-8 (pp III), pep (upper right), and hep (center right). [41]

ter Cherenkov detector, conducted the initial model-independent assessment of solar neutrino fluxes, thereby affirming the solar neutrino discrepancy. In 2001, researchers uncovered that the solar neutrino anomaly stemmed from neutrino oscillations, resolving the longstanding puzzle. From the 2000s to 2020s, the Sudbury Neutrino Observatory (SNO) [46] directly detected the full solar neutrino flux, comprising non-electron neutrinos, thus verifying neutrino oscillations. Moreover, Borexino [47] was able to detect neutrinos generated in both the pp-chain reaction, as well as, the CNO cycle, providing a comprehensive view of solar neutrino production.

Neutrino experiments like Super-Kamiokande, SNO, and Borexino measured the survival probability of electron neutrinos produced in the core of the Sun all the way to Earth. The survival probability depends on mixing parameters - mixing angle,θ_{12}, and neutrino mass squared difference Δm^2_{21}. Figure 3 shows the survival probability (light blue band) of solar ν_e as a function of neutrino energy as explained in [37]. The plot shows the data points (in black), from left to right, represent the Borexino measurements for pp, 7Be, pep, and 8B neutrinos (shown in red), along with the SNO+Super-Kamiokande (SNO+SK) measurement for 8B neutrinos (shown in black). Within the Borexino 8B data, the three points correspond to the low-energy (LE) range, the combination of low-energy and high-energy (LE+HE) range, and the high-energy (HE) range.

Numerical methods were to calculate the survival probability of solar neutrinos as they interact with matter via the MSW mechanism [49]. This computation considers the full three-flavor neutrino mixing. It helps extract the neutrino mixing parameters

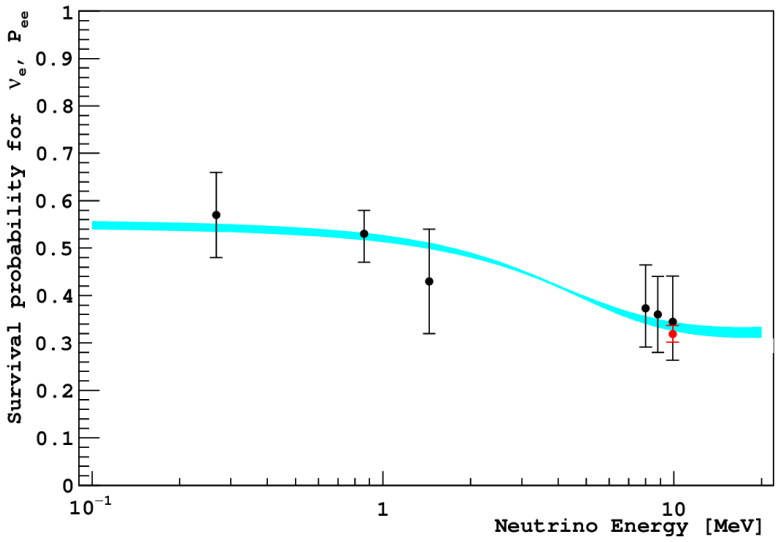

Figure 3: The light blue band represents the electron neutrino survival probability, as predicted by MSW-LMA effect [48]. The flux is based on Standard solar model with black point indicating the Borexino neutrino data and the red point ins the combined SNO+Super-Kamiokande data.

from the observed survival probabilities of solar neutrinos. Additionally, the KamLAND [50] experiment, which detects electron antineutrinos from nuclear reactors at medium baseline, has played a role in accurately measuring the solar neutrino oscillation parameters θ_{12} and Δm^2_{21}. KamLAND's results suggest a slightly larger preferred value of Δm^2_{21} compared to analyses based solely on solar neutrino data. Also it has been observed that the solar mixing angle θ_{12} tends to rise slightly with an increase in the value of the reactor mixing angle θ_{13}. This suggests a subtle link between the measurement of solar θ_{12} and the specific value of θ_{13}, which is mainly determined by reactor neutrino experiments. The upcoming DUNE [51] and JUNO [6] experiments are expected to significantly enhance the precision of measurements for solar neutrino mixing parameters, surpassing current global fit results.

2.4.2 Atmospheric

Atmospheric neutrinos have been essential in finding neutrino oscillations and remain vital for studying neutrino properties and exploring new physics in the neutrino field. Atmospheric neutrinos have baselines ranging from tens of kilometers to the diameter of the Earth (around 12,700 km) and have energies ranging from hundreds of MeV to tens of GeV.

Atmospheric neutrinos arise due to the interactions of cosmic rays-mostly protons-with atoms in the Earth's atmosphere. In such an interaction, a shower of particles is produced which contains the short-lived mesons like pions, decaying to muons and muon neutrinos/antineutrinos ($\pi^- \rightarrow \mu^- + \bar{\nu}_\mu$). Muons further decay into electron neutrinos / antineutrinos along with muon neutrinos($\mu^- \rightarrow e^- + \nu_\mu + \bar{\nu}_e$) as shown

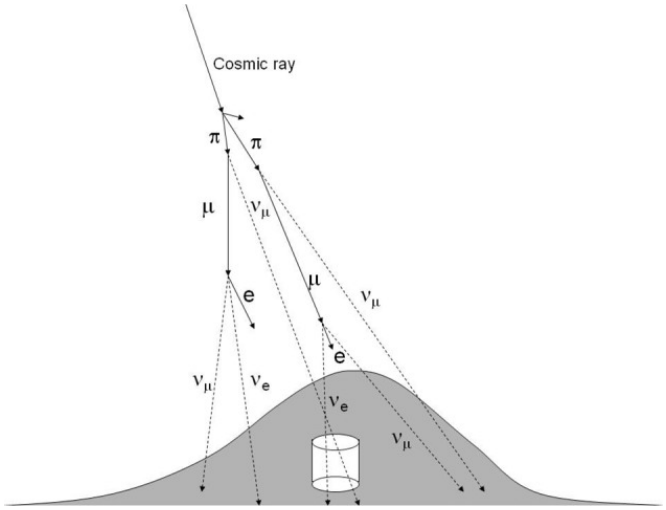

Figure 4: Illustration of cosmic rays producing atmospheric neutrinos after colliding with an air nucleus in the atmosphere [52].

in figure 4. Thus, about two-thirds of the atmospheric neutrinos are muon neutrinos and antineutrinos, while one-third are electron neutrinos and antineutrinos.

In 1965, the initial detection of atmospheric neutrinos was accomplished by two separate teams. They installed detectors deep underground, one in the Kolar Gold Mines of South India and the other in a South African gold mine, to observe upward-going muon events. During the 1980s and 1990s, the Kamiokande [53] and IMB [54] experi- recorded a deviation in the ratio between muon and electron neutrinos-the "atmospheric neutrino anomaly". These observations provided a strong indication that muon neutrinos might oscillate into other flavors of neutrinos like tau neutrinos while passing through the atmosphere. In 1998, the Super-Kamiokande experiment provided the first solid evidence of neutrino oscillations using atmospheric neutrino data. They observed a shortage in the count of upward-going muon-like events than predicted while the electron-like events aligned with the predictions. This was taken as proof that muon neutrinos change into tau neutrinos as they travel through the Earth. Experiments like Super-Kamiokande [53], IceCube [55], and ANTARES [56] have made more accurate measurements of the three-flavor neutrino oscillation parameters, including mass ordering and CP violation, using atmospheric neutrinos.

The NOvA [57] and T2K [58] experiments, conducted from the 2010s onward, have accurately measured neutrino oscillation parameters such as θ_{23}, and Δm^2_{32}. Pooling data from these long-baseline neutrino oscillation experiments, employing neutrino beams, has effectively resolved ambiguities in the neutrino oscillation parameter space and improved the precision of constraints. The upcoming DUNE [59] experiment aims to gather tens of thousands of atmospheric neutrino interactions, enabling the investigation of neutrino oscillations and the potential measurement of the Earth's matter profile. By merging DUNE's atmospheric neutrino data with its long-baseline neutrino beam data, it can determine if observed neutrino oscillations align with

the standard three-flavor model or if they point to the need for new physics. The upcoming JUNO experiment also aims to precisely measure the atmospheric neutrinos to study neutrino oscillations and to measure NMO.

2.4.3 Reactor

Nuclear reactors are intense, isotropic sources of electron antineutrinos ($\overline{\nu_e}$). They can be observed at short baselines of 1-2 km from the source and have energy ranging from 1-10 MeV. The main detection response for reactor neutrinos in scintillator experiments is the IBD reaction: $\overline{\nu_e} + p \rightarrow e^+ + n$. The resulting positron deposits energy and annihilates into two 511 keV gamma rays. The neutron generated in the IBD process is usually trapped $\sim 200\,\mu s$ later by a hydrogen atom, resulting in a signal that coincides with the positron in time. The IBD reaction and the interaction cross-section is illustrated in figure 5. The IBD detection process as outlined in the top of the figure shows neutrino interacting with a proton, produces a positron and electron. The positron promptly emits energy and the neutron continues to scatter before being captured by a proton emitting a gamma ray. The blue curve represents the IBD reaction cross-section and the interaction spectrum is indicated by the red curve. Reconstructing the energy spectrum of the incident reactor antineutrinos involves examining the temporal coincidence and energy spectrum of the detected positron and neutron signals.

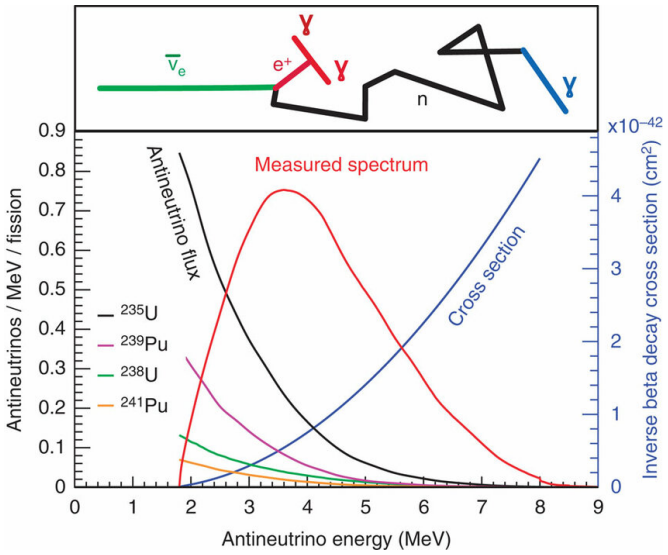

Figure 5: Detection of the coincidence signal of prompt positron and delayed neutron signal confirms a neutrino candidate. The bottom part shows the reactor neutrino flux for different isotopes. The inverse beta decay reaction's cross-section is the blue curve and the outcome (interaction spectrum) detected by the detectors is indicated by the red curve [60].

The Cowan-Reines experiment was the first direct detection of reactor antineutrinos in the 1950s. These first studies not only confirmed the basic features of reactor

neutrinos but also laid the foundation for further investigation into neutrino oscillations. In the 1990s and 2000s, experiments such as Chooz and Double Chooz [61] studied neutrino oscillations at short distances of about 1-2 km away from the reactor cores. By observing neutrino disappearance, Double Chooz gave the first indication for a non-zero value of the neutrino mixing angle θ_{13} in 2011, subsequently confirmed by Daya Bay [62] and RENO [63]. RENO's investigations was important in probing the "reactor antineutrino anomaly," an observed difference between measured reactor antineutrino fluxes and the corresponding predicted fluxes [30]. The observed deviation is investigated to find potential new physics phenomena, among them could also be the possibility of sterile neutrinos.

2.4.4 Accelerator

Accelerator neutrinos result from collisions of high-energy protons directed to a fixed target, creating in a shower many pions and kaons. They decay into muon neutrinos (ν_μ) and antineutrinos $(\overline{\nu_\mu})$ along with smaller proportions of electron neutrinos (ν_e) and antineutrinos $(\overline{\nu_e})$ [64]. Accelerator neutrino experiments have a configuration for short baseline (kilometer-scale), long baseline of (over 100 kilometers), with neutrino energies ranging from hundreds of MeV to a few GeV-all tailored to their respective experiment goals. The detectors in short-baseline experiments are set up close to the neutrino source, within a few kilometers, while for long-baseline experiments, they are tens to hundreds of kilometers away. The short-baseline experiments, including ND280 [65], MicroBooNE [66], MINERvA [67] and the Short-Baseline Near Detector at Fermilab [68], study neutrino interactions before the significant oscillation processes take place. The longbaseline experiments like T2K [69], NOvA [70], and the upcoming DUNE [71] will explore oscillations over large distances through the Earth.

In accelerator neutrino experiments, that oscillation probabilities, including $P_{\nu_\mu\nu_e}$ and $P_{\nu_\mu\nu_\tau}$, are linked to these neutrino mixing parameters. The key parameters include the three neutrino mixing angles (θ_{12}, θ_{23}, θ_{13}), and two independent mass squared differences (Δm^2_{21}, Δm^2_{32}), that govern the probabilities of neutrino flavor oscillations observed in long-baseline accelerator experiments. Experiments, like T2K [69], DUNE [72], and ESSnuSB+ [73] also target measuring the CP-violating phase (δ_{CP}) to probe for leptonic CP violation. A small portion of this study focuses on designing the horn parameters or the ESSnuSB+ and is explained in chapter 6. The current and future accelerator neutrino experiments prioritize precisely measuring these parameters, potentially incorporating energy dependence considerations.

To sum up, the various neutrino sectors offer complementary data regarding the neutrino mixing parameters. As of now, measurements have been made for three mixing angles and two squared mass differences. However, more data is required regarding whether CP violation occurs in the lepton sector. Additionally, the pattern of mass hierarchy remains undisclosed. The upcoming section will elaborate on the unresolved areas in neutrino physics.

2.5 Open Questions

Neutrino physics is a rapidly evolving field of research with many open questions that continue to puzzle scientists. Scientists are continuing to conduct experiments to gather more information about these particles. There are still some fundamental questions that need answers. Are neutrinos Dirac or Majorana particles? Is the neutrino mass hierarchy normal $(m_3 > m_1 > m_2)$ or inverted $(m_2 > m_1 > m_3)$? Is there a violation of CP symmetry in the lepton sector? Do sterile neutrinos exist? The present understanding of the answers to these questions are briefly described in the following sections.

2.5.1 Nature of Neutrinos

Neutrinos may be Majorana particles, meaning that they are their own antiparticles, but it is uncertain. If a neutrino is Dirac particle, it differs from its own antiparticle. A massive Majorana neutrino violates lepton number conservation, due to being its own antiparticle. The tiny masses of the neutrinos makes it challenging to determine if they are Dirac or Majorana particles. One of the most practical methods to investigate the Majorana nature of massive neutrinos is through observing neutrinoless double beta decays ($0\nu\beta\beta$) as this process can only occur with Majorana neutrinos. This is expressed as $N(A, Z) \rightarrow N(A, Z + 2) + 2e^-$. The experimental observable of neutrinoless double beta decay is its half-life, denoted as ($T^{0\nu}_{1/2}$). The current best limit on the half-life of $0\nu\beta\beta$ decay comes from the KamLAND-Zen liquid scintillator experiment [74], utilizing the ^{136}Xe isotope, which has set a bound of ($T^{0\nu}_{1/2} > 3.8 \times 10^{26}$) years (at 90% confidence level). Several current and future experiments are exploring this topic using various isotopes and experimental approaches. Further insights are available in the review article [75].

2.5.2 Mass Ordering

Neutrinos have three flavors and can change between them, but their mass hierarchy remains unclear. Two possible scenarios are normal hierarchy ($m_1 < m_2 < m_3$), or inverse hierarchy ($m_3 < m_1 < m_2$). The two cases are illustrated in figure 6 the left (NO) and right (IO). Here, violet, red and yellow mark the admixtures of ν_e, ν_μ, and ν_τ to the mass states, respectively. Also the sign of Δm^2_{31} is crucial as it affects vital processes, including $0\nu\beta\beta$-decay. In atmospheric, long baseline accelerator and supernova neutrino experiments, flavor oscillations depend on the sign of Δm^2_{31} [76], [77]. Also, the interference effects of the two atmospheric mass-squared differences in the reactor neutrino vacuum oscillations depend on the sign ofΔm^2_{31} [78].

Various future efforts are underway to determine the mass ordering of neutrinos, employing primarily three approaches. The first approach involves medium baseline reactor neutrino experiments, exemplified by JUNO [7] which is expected to start data taking in 2025. The second approach focuses on long baseline neutrino beam

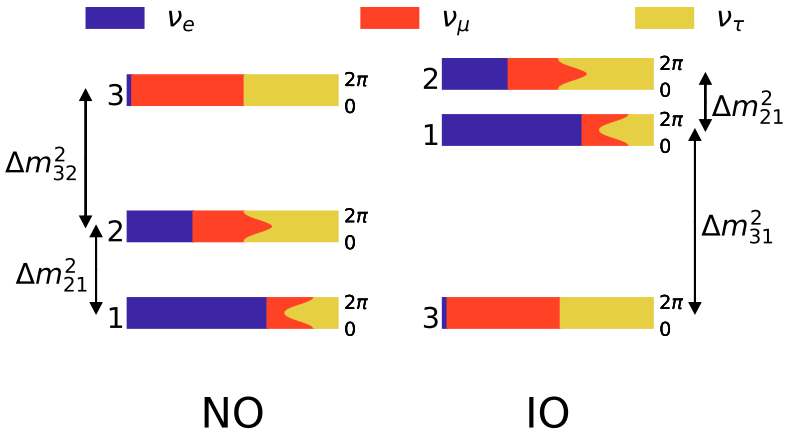

Figure 6: This illustration shows the neutrino mass ordering and the unknown absolute mass scale. On the left, it displays the squared neutrino masses for the Normal Mass Ordering , while on the right, it shows them for the Inverted Mass Ordering. Violet, red, and yellow mark the admixtures of ν_e, ν_μ, and ν_τ to the mass states, respectively [79].

experiments, which include NOvA with increased statistics and DUNE [71]. While JUNO focuses on quasi-vacuum oscillations, the long baseline experiments use the MSW effect. Finally, the third approach revolves around atmospheric neutrino-based experiments, such as JUNO, ORCA [80], PINGU [81], and Hyper-Kamiokande [82]. By precision measurement of neutrino energies and directions, JUNO can identify these atomspheric oscillation patterns and would distinguish between the two mass orderings on the basis of how oscillations would evolve under Earth's matter effects.

2.5.3 CP Violating Phase

Neutrino CPV is defined as the combined violation of charge conjugation (C) and parity (P). The CP symmetry, relates particles and antiparticles of mirrored spatial coordinates and defines whether they behave identically. Though CP violation has been observed in the baryon sector [83], its status in lepton sector remains undetermined. Under the assumption of CPT conservation, which is fundamental for theory construction, CP violation can also be explored through the complementary channel of T symmetry violation, although this approach currently lacks precision. Long baseline neutrino beam experiments, such as T2K [69] and NOvA [84] , are well-suited to investigate lepton CP violation by measuring the δ_{CP} phase through muon neutrino to electron neutrino appearance. Additionally, future long-baseline experiments like DUNE [72], Hyper-K [82]and ESSnuSB+ [73] with improved δ_{CP} resolution, are poised to potentially resolve leptonic CP violation.

2.5.4 Sterile Neutrinos

In addition to the three flavor of neutrino, a fourth flavor might exist. These are called sterile neutrinos as they do not interact via weak force. Sterile neutrino have been suggested as a possible explanation for experimental anomalies like those observed in the LSND [85] and MiniBooNE [86] experiments, indicating the presence of more neutrino states whose masses are below 1 eV [87], [88]. These anomalies have led to an increase in experimental activity in searching for a more categorical indication of sterile neutrinos. Utilizing the globally best-fit parameters from the initial anomalies, researchers are looking to investigate the shape of short-baseline oscillations. The sterile neutrinos are predicted to exhibit a distinctive pattern at a particular L/E ratio corresponding to $\Delta m^2_{41} \geq 1\,\mathrm{eV}^2$. The above experiments such have reported anomalies that might be attributable to light sterile neutrinos. On the other hand, contrary results from other experiments such as MicroBooNE failed to confirm their existence of light sterile neutrinos. In contrast, heavy sterile neutrinos in the range of 105 to 1012 GeV are predicted by numerous extensions to the Standard Model such as Grand Unified Theory (GUT) and left-right symmetric models. These predictions arise as part of the seesaw mechanism [89], which is proposed to account for the small observed neutrino masses. Regardless of their mass they are only detectable when they mix with active neutrinos. This mixing can affect the unitary of the PMNS matrix, adding more generations of neutrinos. Current and future long-baseline neutrino experiments aim to search for anomalies in oscillation that may prove the existence of sterile neutrinos and their subsequent role in neutrino sector [90].

3 Liquid Scintillator Experiments: JUNO & TAO

This chapter first introduces to the working mechanism of Liquid Scintillator (Liquid Scintillator (LS)) detector, including its major components and the basic physics from light generation to detection. With this established theoretical foundation, the chapter then introduces JUNO and its subdetector TAO both of which are LS experiments. With a brief overview on the JUNO experiment, the chapter explains in detail the TAO experiment and its vital role in aiding JUNO to achieve its prime goal. The chapter then describes the detector design and the physics goals of the TAO experiment.

3.1 Physics of Liquid Scintillator Detectors

Liquid Scintillators LS are target materials that emits light flashes when particles interact with them. The light flashes produced are detected by specialized sensors that convert them to electrical signals for analysis. It therefore enables the detection of various particles. LS is typically a mixture of an organic solvent, fluor (primary scintillator), wavelength shifter (secondary scintillator), and other optional additives. It is enclosed in a tank which is either cylindrical or spherical. LS utilizes large volume of dense materials often tens of meters and hundreds to multi-kiloton scale to increase the probability of neutrino interaction. These are popularly known for their low energy threshold (keV range) making them effective for detecting low energy neutrinos. LS also has the ability to determine the event energy with great precision (in comparison to Cherenkov detectors) due to its nearly perfect linear response in the low energy range. This section goes into the details of the physics that happens in the LS highlighting the above features.

3.1.1 Primary Interaction

Neutrinos interact via weak forces and cannot be measured directly hence the charged particles that are produced during their interactions are detected instead. For particles with mass lighter than the mass of electron m_e, the mean loss of energy E, per unit length x, is described by the Bethe-Bloch formula [14]

$$\left\langle -\frac{dE}{mdx} \right\rangle = Kz^2 \frac{Z}{A} \frac{1}{\beta^2} \left[\frac{1}{2} \ln \left(\frac{2m_e c^2 \beta^2 \gamma^2 W_{\max}}{I^2} \right) - \beta^2 - \frac{\delta(\beta\gamma)}{2} \right]. \tag{3.1}$$

The constant K is defined as $K = 4\pi N_A r_e^2 m_e c^2$ (where N_A refers to Avogadro's number, the classical electron radius is given by $r_e = \frac{e^2}{4\pi\varepsilon_0 m_e c^2}$, ε_0 is the vacuum permittivity), z is the charge number of the incident particle, the atomic mass and

atomic number of the absorber is denoted by mA, and Z, the parameter β is defined as the ratio of the particle's velocity v to the speed of light c, the density correction is denoted by $\beta\gamma$, W indicates the energy transfer to an electron in a single collision and mI is the mean excitation energy. The factors in the equation like particle velocity, charge and material properties of the scintillator influence the energy loss and therefore the subsequent light production, which is crucial for analyzing neutrino events. The gammas resulting from the IBD in LS are neutral but can be measured indirectly. They interact with the LS through several process: photoelectric effect, Compton scattering and pair production which releases charged particles that can be measured. According to the gamma interactions in Carbon [14], the photoelectric effect dominates for gamma rays with energies between 10-50 keV, the Compton effect dominated between 100 keV to 10 MeV and pair production occurs for gamma rays that have energies exceeding 1.022 MeV.

3.1.2 Emission, Propagation & Detection of Light

Emission: Light serves as a vital source of information required for event reconstruction. Two primary mechanism of light emission in LS are scintillation and Cherenkov radiation.
Scintillation: When charged particles pass through the organic solvent, they deposit energy, exciting the delocalized π-electrons in the carbon to higher energy state creating excited solvent molecules. The unstable solvent molecules transfer their energy to flour (fluorescent solutes) and excite them as well. The excited electrons return to their ground state, resulting in the emission of photons in a process known as fluorescence (if the radiative lifetime is a few nanoseconds) or phosphorescence (if the radiative lifetime is a few microseconds). The emitted light is in the UV range but if the scintillator is composed of only one type of molecule, light would be self absorbed. To minimize self absorption, wavelength shifters are added to the scintillation mixture. Wavelength shifters absorb the emitted UV light and re-emit in longer wavelengths typically in visible range or range appropriate for the light sensors. This would improve the overall light collection efficiency. The light yield as described by Birks Theory [91]

$$\frac{dL}{dx} = L_0 \frac{dE}{dx} \cdot \frac{1}{1 + k_B \frac{dE}{dx}}, \tag{3.2}$$

where $\frac{dL}{dx}$ is luminesce per unit length, $\frac{dE}{dx}$ is the energy loss per unit length and k_B the Birks parameter which depends on the LS material. The above equation implies the light yield depends on the particle and its energy.
Cherenkov radiation: When charge particles pass through dielectric medium with velocity greater than the local phase velocity of light, they produce Cherenkov radiation. The electromagnetic field due to polarization becomes asymmetric because the medium cannot respond quickly enough to return to its equilibrium state. This results in overlapping wavefront that constructively interfere to produce light (near

UV range) forming a Cherenkov cone having an angle

$$\theta_C = \text{acos}\left(\frac{1}{n\beta}\right), \tag{3.3}$$

where n denotes refractive index and $\beta = v/c$. The directional information provided from the cone can help in studying particle direction. The amount of photons emitted per unit length per unit wavelength [14] is

$$\frac{d^2N}{dxd\lambda} = \frac{2\pi\alpha z^2}{\lambda^2}\left(1 - \frac{1}{\beta^2 n^2(\lambda)}\right) \tag{3.4}$$

where, α is the fine structure constant, z is the charge number of the particle. Cherenkov radiation is emitted instantaneously on the picoseconds scale.

Propagation: Light propagation in the liquid scintillator is dictated by a few key processes, namely: absorption, Rayleigh scattering, and Mie scattering. Absorption of light is one of the key processes involved in light propagation in liquid scintillators, which occurs for photons with energy that matches an excitation level of scintillator molecules. This process is described in context of the Beer-Lambert law

$$I(x) = I_0 e^{-x/L} \tag{3.5}$$

where, $I(x)$ is the intensity of light at distance x, I_0 is the intensity at distance 0, and L is the propagation length. The Stokes shift accounts for the difference between absorption and emission spectra, emission is generally red-shifted from absorption due to relaxation into a lower vibrational state by a photon. The absorbed energy will be re-emitted as fluorescence or converted to heat through non-radiative process. Fluorescence re-emission is isotropic and delayed due to the molecule decay time, changing the trajectory of the original photon. This cycle of absorption and emission can repeat, greatly influencing the overall light propagation and detection efficiency in LS detectors. Energy transfer facilitated by overlap of the emission and absorption spectra of the different scintillator components is a key part of the scintillation mechanism in large-volume detectors. Another way for the photons to propagate is through Rayleigh scattering. The elastic scattering mechanism takes place when the corresponding photons interact with the molecules or the density fluctuations of the scintillator which correspond to an intrinsic limit of the transparency of the material. It is highly wavelength dependent, following a cross-section of typically λ^{-4}. The differential cross-section for Rayleigh scattering obeys

$$\left(\frac{d\sigma}{d\Omega}\right)_{\text{ray}} \propto \frac{1 + \cos^2\theta}{2} \tag{3.6}$$

where θ is the scattering angle. As indicated by $\cos^2\theta$, the scattering will be more intense in the forward and backward direction when $\theta = 0$ and $\theta = 180$. Mie scattering is relatively less wavelength dependent as compared to Rayleigh scattering. Mie scattering in the liquid scintillator takes place through scattering of light by particles or impurities whose size is in similar scale to the scattered light's wavelength.

Mie scattering can result from suspended particles or other inhomogeneities in the scintillator medium. None of these processes can be reliably detected, the information that could be received gets diminished by the number of photons that have been scattered or absorbed and can be explained using equation (3.5). The propagation length in equation (3.5) is a combination of the above effects and can be updated as

$$\frac{1}{L} = \frac{1}{L_{\text{abs}}} + \frac{1}{L_{\text{ar}}} + \frac{1}{L_{\text{ray}}} + \frac{1}{L_{\text{mie}}} \tag{3.7}$$

where, L_{abs} for absorption, L_{ar} for absorption and remission, L_{ray} for Rayleigh scattering and L_{mie} for Mie scatting.

Detection: The effective detection of photons requires an array of photon detectors covering the target area, balancing excellent energy resolution and spatial coverage with a possible budget restriction. The principle of detection by these devices is based on the photoelectric effect, the conversion of optical photons into electrons. Different types of detectors are chosen based on the specific detection requirement and the target area requirement. Few of the common choices include Silicon Photomultipliers (SiPM), Photomultipler Tubes (PMTs), Single Photon Avalanche Diodes (SPAD) and Large Area Picosecond Photodetectors (LAPPD). The key characteristics of theses detectors include Photon Detection Efficiency (PDE), Transit Time Spread (TTS) and dark count rate. PDE is the detector's ability to convert the incoming photons to signal and hence it is defined as the ratio the detected photons over the incident photons. TTS is the variation of the signal information time within the detector and can be roughly translated into the time resolution of the photodetector. Dark count rate is the false count that were registered in the absence of the incident light. These characteristics are important to know the overall performance and the precision of the detectors.

JUNO utilizes PMTs while TAO utilizes SiPMs in their respective LS. The working principle of a PMT is based on the photoelectric effect and the emission of secondary electron. Photons incident from outside the PMT enter the PMT through the input window, and hit the photocathode that is coated with the photosensitive material. This causes photoelectrons to be emitted from the photocathode into the vacuum of the tube. The emitted electrons are then focused by electrodes onto a series of dynodes, where secondary emission occurs – each electron impacting a dynode contacts a few more, causing an avalanche of emission – and so considerably amplify the signal. When this electron avalanche is amplified and driven to the anode, this creates a signal or electrical pulse which can be measured and corresponds to the original detection of the photon.

SiPMs are detectors that function according to the principles of SPADs to detect low levels of light from an event with high sensitivity. SAPDs are high-sensitivity photon detectors with capabilities of detecting very weak optical signals, even as weak as single photons. Once reverse-biased above breakdown voltage, it operates in the so-called Geiger mode, whereby a single incident photon initiates an avalanche of

charge carriers that creates an electrical signal. A SiPM is an array of SAPDs working in independent microcells. A microcell can absorb a photon, causing an avalanche breakdown and a large current pulse resulting from charge carrier multiplication. A series resistor helps to extinguish this avalanche in such way that the voltage drop across the diode falls below its breakdown potential, which allows it to reset to detect the next photon. Each time the SiPM detects a photon, it responds with a pulse, and a series of these pulses provide a measurement of the amount of detected light.

Finally, after photon detection, signal processing, and data acquisition are performed in such a way that amplified signals from photon detectors are routed through electronics with discriminators to filter out noise. Depending on the storage, the the signal maybe fully digitized or only the key information are stored. Due to storage limitations, it is often not possible to save every digitized sample, leading to strategic implementations such as data compression, real time spectrum analysis, selective sampling, etc. However, in critical events, selective information may need to be recorded at a higher rate, with full waveform storing the most information useful for complete signal reconstruction and even digitized pulse shape yielding useful, recoverable data.

3.2 JUNO

The Jiangmen Underground Neutrino Observatory (JUNO) [6] is a large LS experiment that is located in Jiangmen, with a baseline of about 53 km from the Yangjiang and Taishan nuclear power plants. This medium-baseline reactor neutrino experiment is located 600 meters underground with a rock overburden of about 1800 m.w.e. to shield against cosmic rays. As shown in figure 7, the detector components include a Central Detector (CD), a water Cherenkov detector, the Top Tracker (TT) and the calibration house. The CD is a 35.4 m diameter acrylic sphere containing 20 kton of liquid scintillator. Roughly 17,612 20-inch PMTs and 25,600 3-inch PMTs surround this sphere enabling it to electron antineutrinos via IBD interactions. The acrylic vessel is supported by 40.1 m diameter stainless steel structure. The central component is surrounded by 35 kilotons of ultrapure water in an enormous 43.5 m diameter tank, which acts as both a buffer and a Cherenkov detector. About 2,400 20-inch veto PMTs are installed in the water tank for identification and tagging of the atmospheric cosmic muons. The Top Tracker is an additional muon tracking system. An energy calibration of the detector is performed with a calibration house that is integrated into the system. With its large LS, JUNO aims to have an energy resolution of about $3\%/\sqrt{\mathrm{E(MeV)}}$ [6].

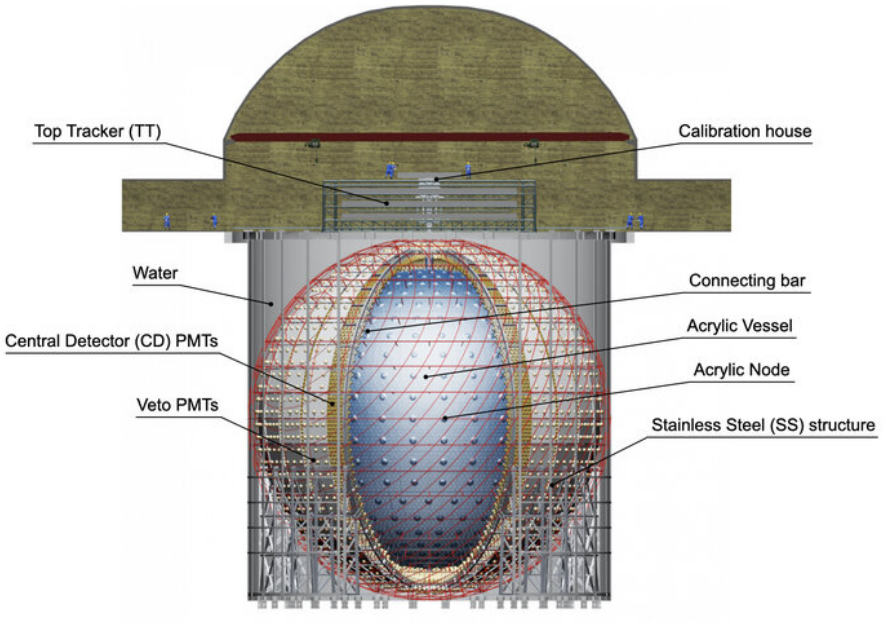

Figure 7: Schematic representation of the JUNO detector. The central acrylic sphere contains 20 kt of liquid scintillator, surrounded by PMTs. This is supported by a stainless steel structure, immersed in water tank with veto PMTs. A Top Tracker and calibration house complete the setup that is designed for precise neutrino measurements [92].

While the NMO can also be determined with long-baseline accelerator or atmospheric neutrino experiments, JUNO stands out due to its primary sensitivity to vacuum oscillations, whereas accelerator and atmospheric experiments primarily rely on the NMO dependence of matter effects. JUNO aims to determine the NMO using precise spectral measurements of the reactor antineutrino oscillations. The expected reactor antineutrino spectra for the different mass orderings are shown in figure 8. The plot shows different shapes for unoscillated spectra (black line), normal ordering (blue), inverted ordering (red) and with only solar term (grey). The small oscillation peaks in the oscillated antineutrino spectrum contain the NMO information. With high resolution measurement of the oscillation spectra, a detailed information of the oscillation parameters (Δm^2_{31}, Δm^2_{21}, $\sin^2 2\theta_{12}$, and $\sin^2 2\theta_{13}$) that govern the spectra can be obtained. The oscillation curves are obtained by applying the survival probability of electron neutrinos on their original energy spectra as shown below

$$P(\bar{\nu}_e \to \bar{\nu}_e) = 1 - \sin^2 2\theta_{13}(\cos^2\theta_{12}\sin^2\Delta_{31} + \sin^2\theta_{12}\sin^2\Delta_{32}) - \cos^4\theta_{13}\sin^2 2\theta_{12}\sin^2\Delta_{21} \tag{3.8}$$

where $\Delta_{ij} \equiv \frac{\Delta m^2_{ij} L}{4E}$ and E is energy. To able to extract the information on the mass ordering a resolution as or better than the size of $\frac{\Delta m^2_{21}}{|\Delta m^2_{31}|}$ is required ($2.6\%/\sqrt{\mathrm{E(MeV)}}$) [7]. Therefore, the existing energy resolution may not be sufficient to accurately measure the oscillation probabilities of reactor antineutrinos. These probabilities are

sensitive to the reactor antineutrino flux and spectrum, which can be subject to significant uncertainties. Some of these uncertainties stem from differences in the nuclear processes that lead to the production of antineutrinos, and others are due to the current model limitations that predict the antineutrino spectrum from reactors as explained in section 3.4. To address these

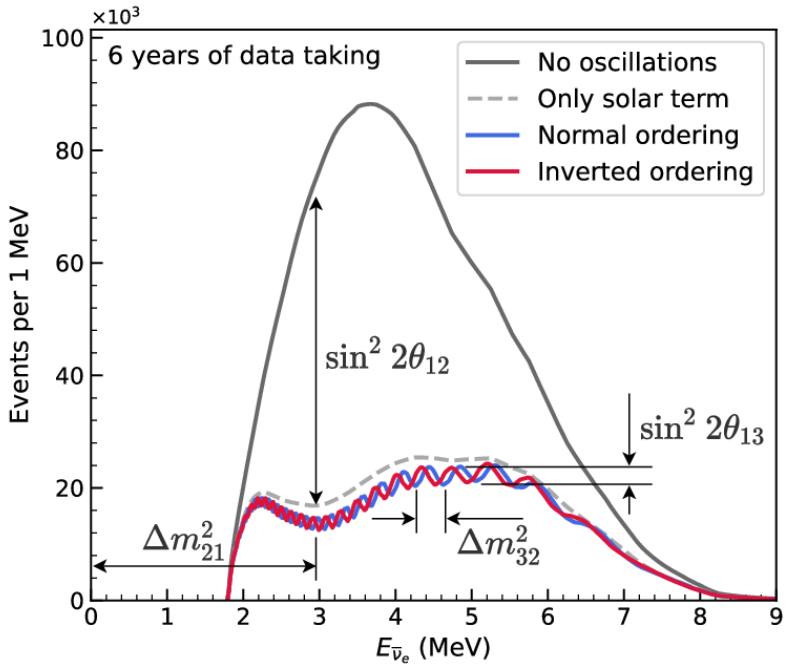

Figure 8: The expected antineutrino energy spectrum for NO, IO, and no oscillation for 6 years of data taking. The curves that correspond to oscillation are obtained by applying survival probability of electron antineutrinos on their original energy spectrum.[93]

challenges, the Taishan Antineutrino Observatory TAO is designed to perform high-precision measurements of the reactor antineutrino spectrum, from the direct measurements from the Taishan Nuclear Power Plant. TAO will provide a model-independent reference spectrum with an energy resolution better than 2% at 1 MeV. The accurate understanding of the antineutrino spectrum allows for better characterization of oscillation effects thereby improving the sensitivity of JUNO in determining NMO. The other goals of TAO are explained in detail in section 3.4.

3.3 Experimental Framework of TAO

3.3.1 Detector Layout

The TAO experiment independently assess the antineutrino energy spectrum emitted from the nearby Taishan nuclear reactor with unmatched precision. This critical

capability aids in probing the reactor antineutrino anomaly and the bump in the 5-6 MeV neutrino flux detected by other experiments. This is explained in section 3.4.1. The three main components of the TAO detector are the CD that is surrounded by a cryostat to maintain low temperatures, a water Cherenkov detector that detects

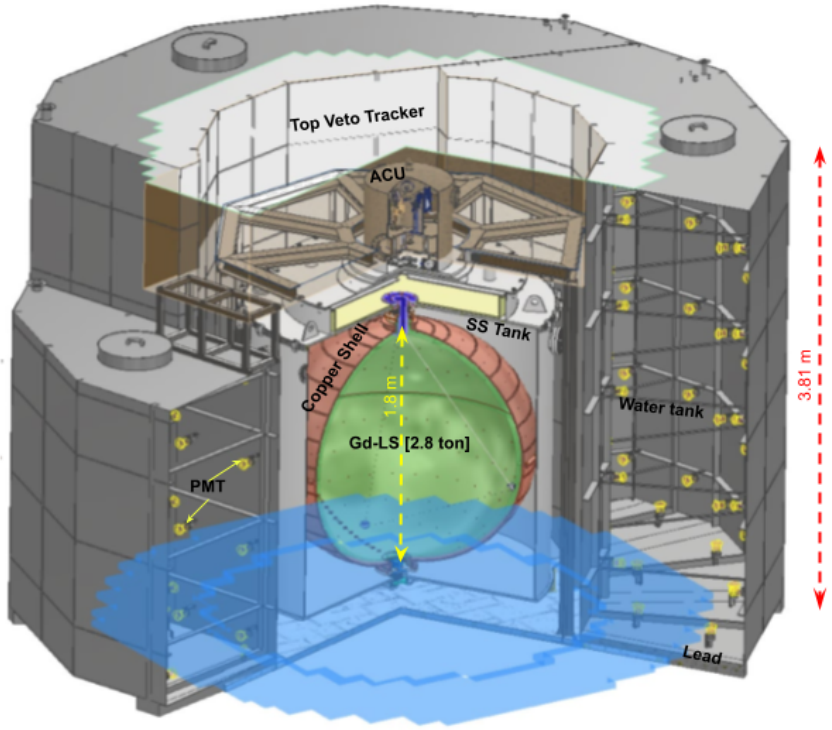

Figure 9: Schematic view of the TAO detector, indicating the liquid scintillator target located in the middle of the spherical copper shell and the stainless steel tank, with the external water tank surrounding it. It consists of a top veto tracker for cosmic ray muon detection an ACU for precise calibration.

Cherenkov light by cosmic muons, and a passive shield layer that shields against neutrons generated by cosmic muons and external radioactivity [10]. Figure 9 shows a sketch of the TAO detector, the central detector houses the LS (doped with Gadolinium) with SiPMs for detecting antineutrinos. The surrounding copper shell provides mechanical support and also thermal stability for the SiPMs. The copper shell is installed within the stainless steel tank that is filled with buffer liquid and maintained at -50°C to reduce dark noise. The water tank surrounding it acts as a Cherenkov detector and the Automated Calibration Unit (ACU) at the top is used for calibration. The following text provides a comprehensive explanation of the assembly details.

Central detector: The CD comprises of two layers. The inner layer is the LS housed within a spherical acrylic vessel. The 2.8 tons Gadolinium-doped liquid scintillator (GdLS) will serve as the neutrino target facilitating the detection of a distinct delayed signal of IBD resulting from neutron capture on Gd hence reducing accidental background. The LS will be curated to have a good transparency and light yield even

at low temperatures. TAO's baseline LS option considers 2 g/L 2,5-Diphenyloxazole, PPO (primary fluor), 1 mg/L 1,4-Bis(2-methylstyryl)benzene (secondary wavelength shifter), 0.43 g/L ethanol (co-solvent to improve solubility at low temperatures), 0.1% Gadolinium by weight (for neutron capture). This composition is engineered to have exceptional optical properties and high radiopurity to achieve a target energy resolution of less than 2% at 1 MeV. Surrounding it is the acrylic vessel that has an inner diameter of 1800 mm and a thickness of 20 mm. A copper sphere surrounds the acrylic vessel, offering mechanical support to ensure the SiPM tiles are directed towards the center of the detector. The external surface of the copper sphere is utilized for the readout electronics and accommodating the cooling pipes.

The outer layer contains the buffer liquid, Liquid Alkyl Benzene (LAB) held in a Stainless Steel Tank (SST). LAB will serve as the liquid scintillator solvent. LAB's high flash point (>130°C) and low volatility make it ideal for proximity to a nuclear reactor. However, LAB's water content can precipitate at low temperatures, reducing LS transparency, necessitating extensive drying. Adding Dipropylenglykol-n-butylethe (DPnB) as a freezing inhibitor and antioxidant addresses this. The stainless steel tank supports all components within the SST, including the ACU and overflow tank on the lid. It ensures an air-tight environment for the liquid scintillator, maintaining a temperature of -50°C inside the SST while requiring insulation to regulate room temperature outside.

TAO uses large-area SiPM tiles produced by Hamamatsu with each tile integrated with thirty two chips of dimension 12 mm x 6 mm [94]. These SiPM tiles has a photon detection efficiency (PDE) exceeding 50%. To keep the dark noise rate within acceptable bounds, the SiPMs must function at cryogenic temperatures of approximately -50°C. SiPM photosensors will be mounted on a spherical copper shell surrounding the acrylic vessel, with a distance of 18 mm between the SiPM surface and the acrylic vessel. Each SiPM tile connects to a Front-End Board (FEB) for readout. A total of 4024 FEBs will cover the $10\,\mathrm{m}^2$ detector area. These FEBs are linked to Front-End Controllers using Vertex Ultrascale Field Programmable Gate Arrays (FPGAs) for data collection. A specialized trigger and (DAQ) system will filter and capture events as they happen, rejecting dark count occurrences.

Water Chrenkov detectors: Surrounding the CD, are three irregular water tanks that form dodecagon shape with 1.2 m thickness serving as both passive shielding (from environmental radioactivity from rock and air) and active Cherenkov muon detectors (effectively serving as a veto detector). They're equipped with 3 inch PMTs to detect Cherenkov light from muons. Approximately 300 PMTs will be evenly spread, averaging 1 PMT per 0.5 m^2, providing about 0.8 % surface coverage. These 3-inch PMTs, along with their bases, potting, and electronic readout, will use the same technology as the JUNO small PMT system [6]. The PMTs require a time resolution of approximately 2 nanoseconds to accurately establish the veto window timing. The dodecagon shape, chosen for TAO, accommodates space constraints and

contains approximately 70 tons of water in total. The tanks are lined with reflective Tyvek film and hold PMTs in place with stainless steel frames. A purification system maintains water clarity and reduces radioactivity. Circulation ensures water turnover in a day.

Calibration: TAO is designed to precisely install radioactive sources for detector calibration using Automated Calibration Unit (ACU) based on a similar system used in the Daya Bay experiment [95]. The ACU, which is featured in TAO, is a complex apparatus that uses radioactive sources for the purpose of detector calibration. The ACU is a system that can mount a variety of radioactive sources, including the ^{68}Ge source, combined gamma-emitting isotopes (^{137}Cs, ^{54}Mn, ^{40}K, ^{60}Co), and a neutron source (^{241}Am–^{13}C). The sources are wound around pen sheathed RT with the PTFE truss, preventing contamination of the gadolinium-loaded liquid scintillator. Using two stepper motors, the ACU is able to move these sources inside the detector with sub-millimeter precision based on glued anchors on the inner wall of the acrylic vessel. The ACU is an integral element in TAO's overall calibration strategy — which also includes an ultraviolet LED calibration system and Cable Loop System (CLS). The ultraviolet LED is used to monitor SiPMS and for precise timing calibration. The CLS facilitates the use of radioactive sources at varying detector positions and enables the accurate mapping of energy-response distributions across various geometries of the detector.

Shielding layer: Simulations show that most fast neutrons come from the top, so a 10 cm layer of lead bricks will be placed below the CD, while about 1 m of High Density Polyethylene (HDPE) will be added above to slow down fast neutrons. Additional HDPE layers may be installed above the steel beam frame for improved top shielding. An HDPE "hat" will be made for the ACU to aid in top shielding, which is expected to slightly increase the fast neutron background by less than 10%. Above the CD, a few layers of plastic scintillator strips will serve as a muon detector, using multilayer coincidence to reduce false detections from natural radioactivity. These strips, coated with TiO2-doped PVC, will be read out by 1-inch PMTs on each end, using electronics from the JUNO 3-inch PMT system. Detailed investigation into the plastic scintillator muon detector's design and assembly is ongoing.

Facility & Installation: A neutrino lab is established at the Taishan Nuclear power plant at a distance of 44 metres from the reactor core. The vertical standing is estimated at approximately 5 meters-water-equivalent. The layout includes space for the TAO detector and it's related facilities constrained by height of 3.85 m. The CD assembly includes liquid filling (loading the solvent follows Daya Bay's procedure using Gd-complex with ligand 3,5,5-trimethylhexanoic acid (TMHA)), integrating SiPM tiles and Frontend Electronics (FEE) with the copper shell, bonding acrylic pieces and building the stainless steel tank. A final mass concentration of 0.1 % Gd in the LS. Once the assembled copper shell is clamped to the acrylic vessel, it is rotated from vertical to horizontal position and then installed to the stainless steel tank and then

rotated to vertical position. Following the CD installation, the ACU will be mounted on the SST. The ACU is vital for TAO as it will contribute to the control of energy resolution degradation and energy bias within 0.05 % and 0.3 %, respectively [96]. It will be operating at $-50°C$ and therefore is protected by a thermal insultion hat made up of HDPE. The veto and shielding setup comprise of a lead bottom shield for the CD, three water tanks encircling the CD, HDPE shielding material positioned above the CD, and plastic scintillator detectors situated atop the HDPE shielding.

3.3.2 Signal & Background

Reactor antineutrinos ($\overline{\nu_e}$) result from the fission products of key isotopes like $^{235}\mathrm{U}$, $^{238}\mathrm{U}$, $^{239}\mathrm{Pu}$, and $^{241}\mathrm{Pu}$. The ($\overline{\nu_e}$) undergo IBD reaction, $\overline{\nu_e} + \mathrm{p} \rightarrow \mathrm{e}^+ + \mathrm{n}$, in the gadolinium-doped liquid scintillator. The positron promptly deposits it's energy in the scintillator and annihilates with an electron creating two 0.511 MeV gamma rays. Neutrons from IBD are primarily captured by hydrogen or gadolinium, producing gammas with energies of 2.2 MeV and about 8 MeV, respectively. The coincidence of the prompt scintillation from the positron with delayed neutron capture on Gd, marks the distinctive ($\overline{\nu_e}$) signature. TAO will be able to detect 2000 IBD events everyday. The energy of the antineutrino $E_{\overline{\nu_e}}$ is linked to the measured prompt energy (kinetic energy of positron + two 511 keV gamma rays) E_{e^+} by

$$E_{\overline{\nu_e}} \approx E_{e^+} + (m_n - m_p - m_e). \tag{3.9}$$

The kinetic energy of the outgoing neutron is negligible, so it can be ignored in a basic calculation. The positron's energy in the scintillator converts into light, and the energy resolution is primarily determined by photon counting statistics. The combination of the excellent optical coverage of 95 %, the high photon detection efficiency of 50 % for the SiPMs and the high light yield of the LS, 12,000 photons per MeV deposited energy yields a total of 4,500 photoelectrons per MeV of deposited energy. This enables TAO to aim for an energy resolution better than $2\%/\sqrt{\mathrm{E(MeV)}}$.

The primary sources of background for IBD events include prompt (from positron annihilation) and delayed (from neutron capture) events, which can either be correlated or uncorrelated in time. The uncorrelated events that pass the energy cuts are accidental backgrounds that typically arise due to natural radioactivity. The proposed solution to this will be doping gadolinium in the buffer liquid and optimizing veto methods. These methods aim to reduce the neutron background-to-signal ratio from an initial estimate of about 10 % to approximately 2 %. Additionally, pulse shape discrimination may offer further suppression of the neutron background. The most significant component of the background of fast neutrons arises from the spallation of cosmic muons within the materials that encase the detector due to the comparatively shallow overburden present in the TAO experiment. A muon veto system will be established to diminish the fast neutron background to fewer than 200 events daily. Furthermore, cosmic muons that engage with carbon present in the liquid scintillator may generate isotopes such as $^{9}\mathrm{Li}$ and $^{8}\mathrm{He}$, thereby adding to correlated background

signals. Table 2 summarizes some important results of the singles and background simulation.

IBD signal	2000 events/day
Muon rate	70 $\mathrm{Hz/m^2}$
Fast neutron background after veto	$<$ 40 events/day
Singles from radioactivity	$<$ 100 Hz
Accidental background rate	$<$ 190 events/day
$^{9}\mathrm{Li}$ /$^{8}\mathrm{He}$ background rate	$\sim$ 54 events/day

Table 2: Summary of the IBD signal and background simulation results [97] [10].

TAO's extensive photosensor coverage, substantial light yield, and operation at cryogenic temperatures will enable precise measurement of the reactor antineutrino energy spectrum, achieving resolution of 1.5 % at 1 MeV. This accurate spectrum will serve as a valuable reference for JUNO and upcoming reactor neutrino experiments and nuclear database evaluations.

3.4 Physics Goals

As discussed in the previous chapter, the unknown CP-violating phase and neutrino mass ordering remain major objectives for next-generation experiments. JUNO aims to resolve the neutrino mass ordering and improve oscillation parameter uncertainties below 1 % via precise energy spectrum measurement. As explained in section 2.4.3 antineutrino yield per fission exhibits a deficit compared to model predictions, known as the reactor antineutrino anomaly as illustrated in figure 10. The plot shows a comparison of measured and predicted prompt energy spectra of fission indicating the observed deficits. The obtained spectrum and its prediction by the Huber-Mueller model together with uncertainties are displayed in the left panel. The ratio of the measured to predicted spectra and the deviation from the local mean are pointed out, respectively, in the middle and the bottom regions of the left panel. The right panel of the figure shows the obtained $^{235}\mathrm{U}$ and $^{239}\mathrm{Pu}$ spectra compared to Huber-Mueller model predictions, with the best normalization factors, to match shapes. The lower and middle panels of the right panel show the extracted-to-predicted ratio of spectra and local deviations for each isotope respectively. The figure shows deficit of the observed fluxes, particularly around 5 MeV where an excess of antineutrinos is observed and this has been confirmed by the recent experiments. To address this issue the reactor antineutrino experiments use near detectors that can provide a reference spectrum. However, the current resolutions obtained from them are insufficient to address the fine structure. This is one of the prime goal of TAO, to provide a precise antineutrino energy spectrum with sub-percent energy resolution that can aid in understanding reactor anomalies and neutrino physics. The following sections explains various physics goals of TAO.

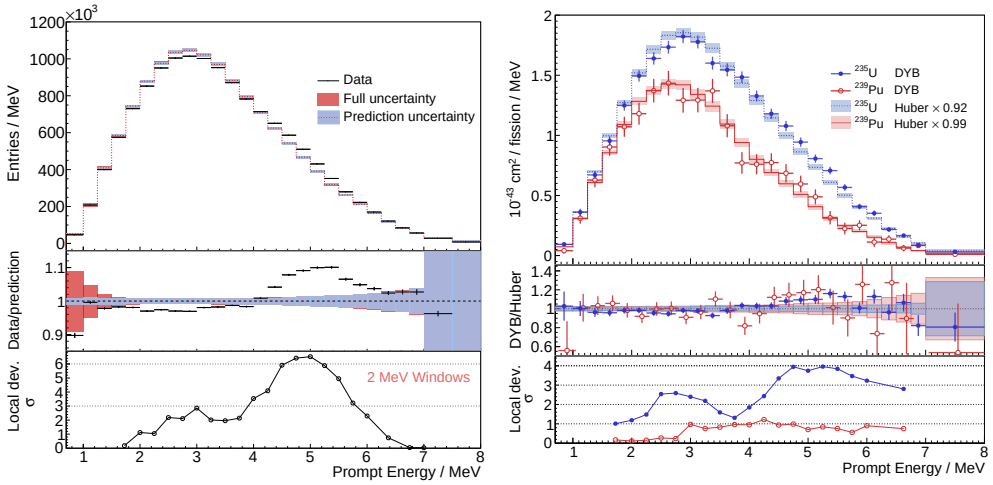

Figure 10: The figure compares the observed reactor antineutrino spectrum to Huber Mueller model predictions. The Left panel shows the predicted and measured prompt energy spectra. On the right panel the extracted spectra of $^{235}\mathrm{U}$ and $^{239}\mathrm{Pu}$ is compared to model predictions (using best-fit normalization factors (0.92 and 0.99)) [98].

3.4.1 Fine Structure Measurement

In a reactor, the energy spectrum of antineutrinos arise from multiple beta decay branches, each exhibiting a sharp edge due to Coulomb correction. These corrections create sharp edges in the spectra as they distort the beta decay branches due to electromagnetic interaction between the emitted beta particle and their daughter nucleus's charge, modifying the particle's energy distribution. This creates fine structure in the spectrum. Figure 11 illustrates this with clear cutoffs at decay branch edges of the listed fission products calculated using summation method. However, the exact shape and amplitude of this fine structure remains challenging due to limited data owing to the low event rates and the fluctuations introduced from the reactor operations. TAO and JUNO are capable of reproducing the summation spectrum, including fine structure, with an accuracy of better than 1 %, as demonstrated in the calculations presented in [99]. TAO's precise measurement aims to validate summation spectrum calculation, with anticipated statistical uncertainty <1 % in the 2.5–6 MeV range, constraining fine structure to <1 % and offering a reference spectrum for JUNO.

The fine structure of the spectrum hold significant insights into nuclear databases and models utilized for forecasting reactor antineutrino fluxes. Variances observed between TAO's fine structure measurements and model forecasts might offer clues to understanding the $\sim$3% shortfall in recorded reactor antineutrino fluxes compared to predictions.

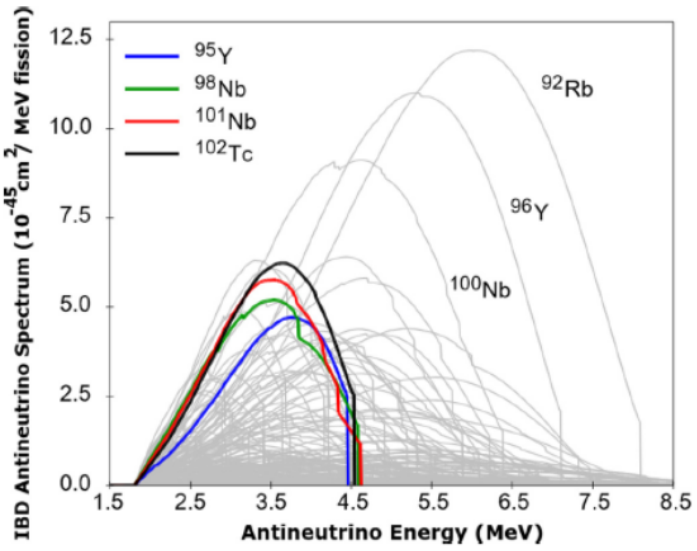

Figure 11: Calculated antineutrino energy spectra from many fission products in a commercial reactor [100].

3.4.2 Reference Spectrum for JUNO

TAO will offer a precise reference spectrum for JUNO as its event rate will surpass JUNO's by 33 times because of the short baseline of about 44 m. TAO has the capability to accurately map its measured spectrum onto the expected unoscillated spectrum in JUNO, considering detector effects such as energy resolution and recoil. This mapping enables the direct application of TAO's reference spectrum to JUNO without requiring prior knowledge of the underlying neutrino spectrum [101]. Utilizing TAO's spectrum as input, JUNO's predicted antineutrino energy spectrum can be expressed as the sum of TAO's reference spectrum and adjustments for potential differences in fission fractions for major isotopes:

$$S_{JUNO}(E_\nu) = S_{TAO}(E_\nu) + \Sigma_i \Delta f_i S_i(E_\nu) \tag{3.10}$$

where $S_{TAO}(E_\nu)$ is the reference antineutrino energy spectrum from TAO, Δf_i is the difference of fission fractions for four major isotopes, and $S_i(E_\nu)$ is the antineutrino spectrum for each isotope. TAO detects antineutrinos only from one of the Taishan reactors but JUNO detects antineutrinos from two Taishan reactors (4.6 GW) and six Yangjiang reactors (2.9 GW) therefore there would be variations in the antineutrino flux due to different reactor types and operational periods.

TAO's statistical uncertainty will influence JUNO's bin-to-bin spectral shape uncertainty (which refers to the differences in the measured values from one energy bin to another due to statistical fluctuations). Figure 12 illustrates the statistical uncertainty of TAO, obtained from three years of data, in contrast to JUNO's uncertainty derived from six years of data. TAO maintains a statistical uncertainty below 1 % across most

energy regions of interest. Assuming a 10 % difference in fission fractions between

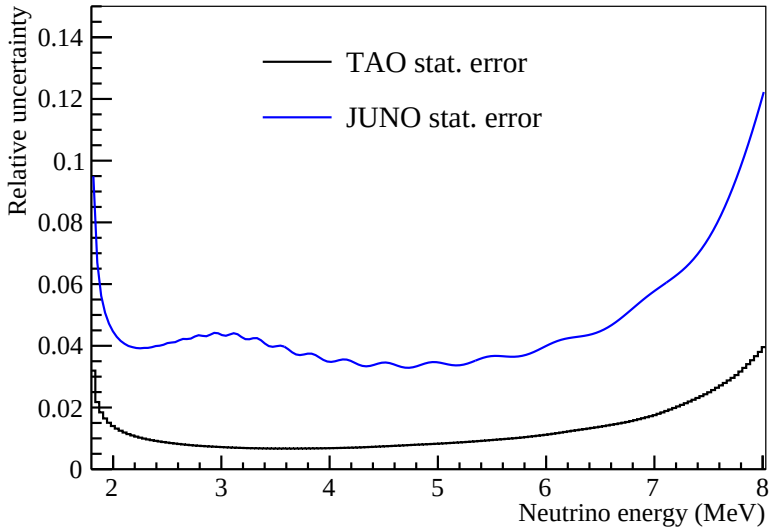

Figure 12: The statistical uncertainty of TAO & JUNO with three & six year's of data taking respectively [10].

TAO and JUNO, the bin-to-bin uncertainty from the reference spectrum is around 1 %. Also a study on the sensitivity of the mass ordering of JUNO vs inputs bin-bin shape [7] as illustrated in figure 13, clearly shows by incorporating TAO's data (black marker), the mass ordering sensitivity (χ^2) improves by approximately 1.5 compared to using the Daya Bay reference spectrum (blue marker).

By offering a high-precision and model-independent reference spectrum, TAO will significantly contribute to JUNO's objective of precisely determining neutrino oscillation parameters, including the neutrino mass ordering and the mixing angles θ_{12} and Δm^2_{21}. TAO's reference spectrum plays a crucial role in minimizing systematic uncertainties in JUNO's oscillation analysis.

3.4.3 Other Goals

Search for sterile neutrinos: As mentioned in section 2.5.4, anomalous neutrino behavior in MiniBooNE and LSND experiments, and a deficit of neutrino yields in gallium experiments hint at the possibility of a fourth neutrino generation, called a sterile neutrino, whose mass splitting is roughly around $1\,\mathrm{eV}^2$. TAO's sensitivity to sterile neutrinos within a 3+1 model, considering its short oscillation baseline was examined. The $\overline{\nu_e}$ survival probability can be approximated as

$$P_{\overline{\nu_e}\to\overline{\nu_e}}(L,E) = 1 - 4\sum_{i=1}^{3}|U_{ei}|^2|U_{e4}|^2\sin^2(\frac{\Delta m^2_{4i}L}{4E}). \tag{3.11}$$

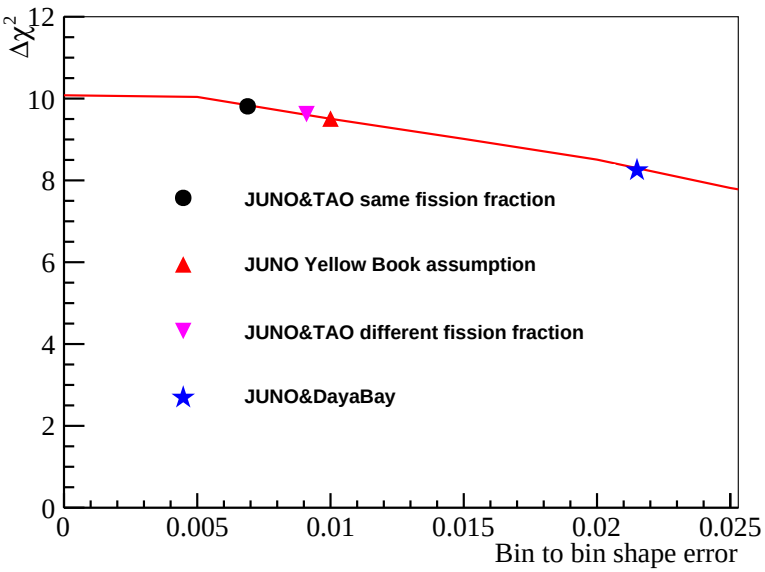

Figure 13: The plot shows mass ordering sensitivity for different reference spectra (represented by different markers) for JUNO. The χ^2 value quantifies the sensitivity where higher values indicate better discrimination between normal and inverted orderings [7].

Here, Δ_{ij} represents the mass splittings, defined as $m_i^2 - m_j^2$ where m_i is the mass of the i-th neutrino state, and $|U_{ei}|$ are elements of the extended 4 $\times$ 4 unitary mixing matrix. TAO's setup involves a cylindrical reactor emitting antineutrinos, detected by its nearby spherical detector. By accounting for background noise and systematic uncertainties, the discrepancy between observed and expected spectra are evaluated statistically. Using the Confidence Level with a signal hypothesis (CLs) statistical method [102]–[104], TAO's sensitivity to sterile neutrinos is gauged by comparing standard and sterile neutrino scenarios. The sensitivity improves with increased statistics and reduced uncertainties. Leveraging its unique features, like its short baseline and segmented detector, TAO complements existing experiments and holds promise for setting new limits on sterile neutrinos.

Reactor Monitoring: Antineutrino detectors provide real-time monitoring of nuclear reactor power and fuel mixture, complementing standard methods and providing a safeguard against unauthorized nuclear activities. The reactor activity is monitored by TAO using the overall antineutrino energy spectrum which varies for different isotopes based on their fission fraction. Changes in fuel composition affect flux and spectrum evolution. Precise measurement of these parameters is critical, especially given recent antineutrino experiments that have highlighted discrepancies from theoretical predictions [105]. The safeguard measures aim to detect and potentially remove plutonium quantity in reactors through fuel reprocessing. TAO aims to bring precision in the spectral measurements that can serve as input for reactor monitoring and safeguard studies.

4 Deep Learning and Genetic Algorithm

Deep learning is a subdomain of machine learning concerned with the use of artificial neural networks [106] comprising multiple layers, also known as deep neural networks. They can extract features automatically from the raw data and learn them without the requirement of explicit feature engineering. Every layer builds on the features extracted from the previous layers, and a complex representation is formed. This hierarchical approach goes a long way in understanding complex patterns within massive datasets, hence proving very useful in particle physics. It could be used in distinguishing types of particles from each other or identifying rare events, or it could be applied in speeding up simulations and optimizing detectors by analyzing large datasets. Of the several deep learning techniques, Graph Convolutional Networks GCNs are used in this study. GCNs model the relations between particles excellently; thus, they are appropriate for problems in particle physics, particularly in complex particle interactions such as predicting the decay of composite particles. On the other hand, Genetic Algorithms GA are optimization techniques that use the process of natural selection to get to the optimal solution within a defined parameter space. In this line, GAs may be applied to design new detector configurations for specific physics searches. A detailed introduction and the principle working of these techniques are discussed in this chapter.

4.1 Deep Learning

4.1.1 Structure of Neural Networks

The fundamental unit of a neural network is the node/neuron, which is grouped into successive layers to process information. A neural network basically includes an input layer, one or more hidden layers, and an output layer [107]. The input layer contains information regarding the initial data. Between the input and the output layers, there are hidden layers in which the information is extracted. Finally, the output layers are those that predict the final result. As illustrated in figure 14, a neuron receives input X_i from the previous layer and processes them with weights W_i, bias b and an activation function f to produce an output Z. A neuron can be mathematically represented as

$$Z = f(\sum_{i=1}^{n} \mathrm{W}_i \cdot \mathrm{X}_i + \mathrm{b}) \tag{4.1}$$

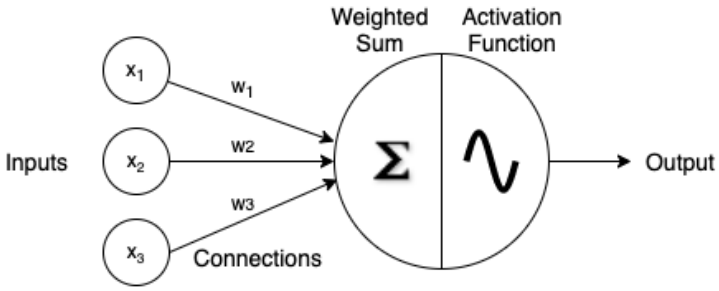

Figure 14: A representation of a neuron that sums up weighted inputs x_i, applies an activation function to modulate the weighted sum to yield the output of the neuron. [108].

In equation (4.1) n represents the total number of input features and the summation starts from i = 1 to iterate over each input, calculating the weighted sum of all inputs. The activation function determines the neuron's output by simulating the (non)firing state of a biological neuron [109]. Weights determine how strong are the connections between the neurons and the biases tune the output by applying an offset to the weighted sum of inputs. By introducing non-linear relationships between the input and the output, the activation function allows the network to learn complex connections [109]. The nonlinearity is incorporated using several functions like Rectified Linear Unit (ReLU), Scaled Exponential Linear Unit (SELU), sigmoid, and tanh [110]. The activation functions used in this study are ReLU [111] and SELU [112] which can be mathematically represented as:

$$\text{ReLU}: \quad f(x) = \max(0, x) \tag{4.2a}$$

$$\text{SELU}: \quad f(x) = \begin{cases} \lambda x & \text{if } x > 0 \\ \lambda\alpha(e^x - 1) & \text{if } x \leq 0 \end{cases} \tag{4.2b}$$

The ReLU function is a popular activation function that introduces nonlinearity by returning zero for inputs less than zero while leaving positive inputs unchanged. One problem with this method is that the neurons might get stuck in returning zeros for continuous negative inputs (also called "dying ReLU"). Despite the drawback, ReLU remains a popular choice because it is quick to compute as it requires only a simple max operation (as shown in equation (4.2a)). Also, it doesn't have any upper limit for the positive inputs thereby allowing free gradient flow preventing vanishing gradient problems. The SELU function although not so popular is utilized for its self-normalizing properties. The predefined constants in equation (4.2b) $\lambda \approx 1.0507 \quad \text{and} \quad \alpha \approx 1.6733$ help in maintaining the mean and variance of the activation across the layers close to zero and one respectively. Unlike ReLU the positive inputs are multiplied with λ, this scaling amplifies the variance of the activations

for larger positive inputs. On the other hand, the negative inputs and inputs that have a value zero are subjected to exponential transformation scaled by $\lambda\alpha$ producing negative output, addressing the issue of dying ReLU. The counterbalancing effect of amplifying positive values and dampening negative values is what makes SELU a self-normalized activation function. This helps in creating a balanced distribution of activations leading to improved training of the network.

4.1.2 Key steps in Building Neural Networks

The building of the neural network involves several key processes: preparing the data, designing the model architecture, initializing training parameters, training the model, evaluating the model and tuning the hyperparameters for better performance. The data preparation begins by defining features (the inputs used by the model) that are extracted from the raw data. Additionally, the dataset is split into training, validation and test sets. The next step is designing the model by the number of layers and the activation functions that it uses. Once the model is designed it undergoes training. Neural networks train in an iterative process by changing weights and biases so that the prediction is quite close to the true output. This is usually done by running the data in batches through several epochs (iterations). The learning/training takes place in three steps: forward propagation, error calculation using loss function and backpropagation. In forward propagation, as the name suggests, the data travels forward through the network, where weighted sums and biases are applied at each layer to produce an output. The second step is the calculation of the error using the loss function. The final step is backpropagation where the error gradients are propagated backwards through the network to update the model parameters: weights and biases at every layer to enhance the model performance. Following training, the model is evaluated using the validation set where tuning the hyperparameters such as learning rate, batch size and other regularization techniques will aid in optimizing the model performance. Finally it is assessed by the test set. This subsection provides a detailed explanation of these processes.

1. Data Preparation: The suitability of the data to be processed by the network has to be ensured before the actual training begins. If the ranges of the input data differ by several orders of magnitudes, then adjusting the parameters could be a difficult task. Certain preprocessing is done on the data to eliminate such complications. One of the methods to do this is to normalize the data, so all features are at a common range, say (0,1) or (-1,1). Feature selection is another important step in preprocessing. Only relevant features are selected for training a model as it impacts the model's prediction. The dataset is also split into training, validation and test data. For this study, a dataset split ratio of 70% for training and 30% for validation is used. A separate test dataset (typically comprising 10-20%) of the total available data is generated independently to provide an unbiased final evaluation of the model's performance. The details of which can be seen in section 5.2.

2. Defining the model: The model is defined by the number of layers and the activation functions it uses. The number and type of layers are designed based on

the problem statement (classification, regression or clustering). As this study focuses on the reconstruction of events in a detector, the task is regression. To cater to this requirement the model is designed with a combination of specialized layers: graph convolutions (for processing spatial relationships of SiPMs), partition pooling (for hierarchical feature extraction), ResNet blocks (for improved gradient flow and feature earning) and fully connected layers (for final output generation). The details of these layers are explained in section 4.1.3 and the implementation of the architecture is explained in detail in section 5.3.1.

3. Parameter Initialization: When initializing the network parameters, the diversity in the weights and biases are to be maintained. This breaks the symmetry and prevents the network from learning identical mappings. This is achieved by randomly initializing the weights and biases. Bias is generally initialized with small constant values or zeros. The weights are usually initialized randomly within a selected range. Proper initialization should prevent a model from suffering from vanishing/exploding gradients and allow convergence during training to occur quickly. Transfer learning can also be applied, in which the weights of a pre-trained model are used in order to initialize the network to provide a head start.

4. Training the model: After initialization, the data is propagated with the help of equation (4.1) to the next layers to generate an output. In the forward, every neuron receives input from the previous layer, applies weights and biases, and processes the result through activation functions. This process produces initial predictions which are compared to the true values using the loss functions. The loss functions are used to gauge the quality of network prediction using a scalar measure at the end of every epoch, depending on the input data and on the parameters of the neural network. The the loss function is chose based on the problem statement, like regression or classification. In case of regression, the commonly used function is Mean Squared Error (MSE):

$$L_{\text{MSE}} = \frac{1}{N_{\text{sample}}} \sum_{i}^{N_{sample}} \left| \hat{Y}_i - Y_i \right|^2 \tag{4.3}$$

where N_{sample} is the dataset size and $\hat{Y}$ and Y are the predicted and true output respectively. The loss value becomes the bias for the final step backpropagation where the biases and weights are updated to minimize the error in the subsequent iterations. The model uses iterative gradient descent, in which the partial derivatives — computed by the chain rule across nested NN — update the initially random parameters towards optimal values. Backpropagation involves calculating errors and partial derivatives of weights and biases. The error term of the output layer δ is derived as the derivative of the loss function L with respect to Z as in equation (4.1):

$$\delta = \frac{\partial \mathrm{L}}{\partial \hat{\mathrm{Y}}} \cdot \mathrm{f}'(\mathrm{Z}) \tag{4.4}$$

where $f'(Z)$ is the derivative of the activation function f to it's input Z, δ represents the sensitivity of the loss with respect to the pre-activation output Z. This helps in distributing the error across the network during the backward pass. The partial derivatives of loss function with respect to weights W, biases b and activation $A(= f(Z))$A are as follows:

$$\frac{\partial L}{\partial W} = \delta \cdot A_{\text{prev}}^{T} \tag{4.5}$$

$$\frac{\partial L}{\partial b} = \delta \tag{4.6}$$

$$\frac{\partial L}{\partial A_{\text{prev}}} = W^{T} \cdot \delta \tag{4.7}$$

These derivatives are crucial in updating the weights and biases, to minimize the loss, the primary goal of optimization.

5. Model Evaluation: After training the model it is first evaluated with the validation dataset. While more parameters often increase performance, at some point additional network depth and width can lead to overfitting and underfitting. This can be explained using figure 15 which shows how training and validation losses vary for a data that is run over 80 epochs. As seen in the plot, below 10 epochs, the validation loss is constantly less than the training loss, which means early underfitting. In the range between epochs 10 through 60, validation loss has tends to fluctuate around the training loss. This indicates how the model adjusts to the training data. After epoch 60, validation loss starts to increase while the training loss is still decreasing. This is a sign for the start of overfitting. To address overfitting two regularization methods dropout layers [113] and early stopping [109] were used in this work. Dropout is a technique that shuts off a portion of neurons and all of their connections randomly. Early stopping tracks the validation loss after each epoch and stops training id no further improvement is noticed. Once the model is updated and finalized its performance is assessed on a separate test set which it has never seen before. Here, only the inputs are fed to the model and it is expected to predict based on the training and evaluation it previously underwent.

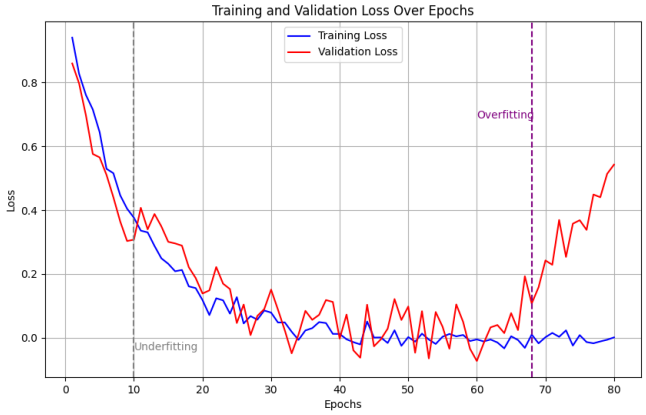

Figure 15: The plot shows the the learning progression of the model across 80 epochs. The first ten epochs indicates a clear case of underfitting. From epochs 10 to 60 the training and validation loss tend to converge, indicating learning. After 60 epochs the increasing validations loss signals the onset of overfitting.

The algorithm 1 explains in detail a neural network's training and evaluation processes. The algorithm begins by initializing weights W, and biases b, along with hyperparameters like learning rate η, epochs E, and batch size B. A neural network NN is designed with a total of L layers, where each layer l has d^l neurons and uses the activation function f^l. The dataset is split into three subsets. The training D_{train}, and validation datasets D_{val} include the inputs X_{train}, X_{val} and true outputs Y_{train}, Y_{val} respectively. However, the test dataset D_{test} includes only inputs X_{test} as it is used to predict outputs $\hat{Y}_{\text{test}}$ from unseen data using the trained and updated model NN. In the training phase, the data is batched and processed over several epochs. For every batch, the forward propagation is conducted whereby linear combination Z^l and activation A^l are computed. Then the batch-wise loss L_{batch} is computed by comparing the target value A^l with output Y_{train}, and this is updated in total training loss, L_{train}. Following it is the backpropagation that begins from the output layer and moves backwards, layer by layer in the network. It computes the error in the output layer δ^{output}, as the element-wise product of the batch loss gradient ∇L_{batch}, and the derivative of the activation function $f'(\cdot)$, evaluated at Z^{output}. Weights and biases get updated in this process to minimize the prediction errors. The next step is validation where the forward propagation is performed in a similar fashion to the training phase however the weights and biases are not updated and the model uses their current values to compute the validation loss L_{val}. The obtained training loss, L_{train}, and validation loss, L_{val}, can be useful to give information on how well the data has been trained and can trigger the saving of the model if the performance improves. The saved model contains information about the best configuration (weights W^l, biases b^l, learning rate η, activation functions f^l, and layer dimensions d^l for each layer l) that achieved the lowest validation loss. Finally, for testing the saved model NN is loaded and the test input X_{test} is fed into the model to generate the predictions $\hat{Y}_{\text{test}}$ without access to the true outputs of the test dataset.

Algorithm 1 Training, Validation, and Testing of a Neural Network

Require:
- Initialized weights W, biases b, learning rate η, number of epochs E, batch size B
- Neural Network NN: Number of layers L, Activation functions f^l for each layer l,Dimensions of each layer d^l
- Model save location M_{save}: file to store the neural network.
- Training data $D_{\text{train}} = \{(X_{\text{train}}, Y_{\text{train}})\}$: inputs X_{train} and true outputs Y_{train}
- Validation data $D_{\text{val}} = \{(X_{\text{val}}, Y_{\text{val}})\}$: inputs X_{val} and true outputs Y_{val}
- Test data $D_{\text{test}} = \{X_{\text{test}}\}$: inputs X_{test}

Ensure: $epoch = 1$ to E ▷ Training begins here

Training:

$L_{\text{train}} = 0$ ▷ Initialize training loss for this epoch

for each batch (X_{train}, Y_{train}) in D_{train} **do**

Forward Propagation:

for each layer l in NN **do**

$Z^l = W^l A^{l-1} + b^l$ ▷ Linear combination

$A^l = f^l(Z^l)$ ▷ Apply activation function

end for

Loss Calculation:

$L_{\text{batch}} = \text{loss}(A^{\text{output}}, Y_{train})$ ▷ Compute batch loss

$L_{\text{train}} = L_{\text{train}} + L_{\text{batch}}$ ▷ Accumulate batch loss

Backpropagation:

$\delta^{\text{output}} = \nabla L_{\text{batch}} \cdot f'(Z^{\text{output}})$ ▷ Compute error at output layer

for each layer l from output to input **do**

$\delta^{l-1} = (W^l)^T \delta^l \cdot f'(Z^{l-1})$ ▷ Backpropagate error

$W^l = W^l - \eta \cdot \delta^l (A^{l-1})^T$ ▷ Update weights

$b^l = b^l - \eta \cdot \delta^l$ ▷ Update biases

end for

end for

$L_{\text{train}} = L_{\text{train}}/(\text{number of batches})$ ▷ Average training loss for the epoch

Validation:

$L_{\text{val}} = 0$ ▷ Initialize validation loss

Forward Propagation on Validation Data:

for each layer l in NN **do**

$Z^l_{\text{val}} = W^l A^{l-1}_{\text{val}} + b^l$ ▷ Linear combination

$A^l_{\text{val}} = f^l(Z^l_{\text{val}})$ ▷ Apply activation function

end for

$L_{\text{val}} = \text{loss}(A^{\text{output}}_{\text{val}}, Y_{\text{val}})$ ▷ Compute validation loss

Log L_{train} and L_{val} for monitoring ▷ Track progress

Save the model NN: store W^l, b^l, η, f^l, d^l to M_{save} if L_{val} improves.

Testing:

Load Model: $NN \leftarrow M_{\text{save}}$ ▷ Load the best saved model

$\hat{Y}_{\text{test}} = 0$ ▷ Initialize predictions

$\hat{Y}_{\text{test}} = NN(\mathbf{X}_{test})$ for all $\mathbf{X}_{test} \in \mathcal{D}_{test}$ ▷ compute predictions from the model

Output: Predicted outputs $\hat{Y}_{\text{test}}$

4.1.3 Layers in the Architecture

This subsection provides a theoretical overview of the selected layers in the architecture specifically designed for the reconstruction task. The layers include GCNs, partition pooling layers, residual blocks and finally a fully connected layer. The detailed implementation is presented in chapter 5.
Graph Convolutional Networks (GCNs)

GCNs perform convolution directly on a graph, a structure that contains a set of nodes (or vertices) and edges that connect the nodes. It can be represented as G = (V, E, W), in which V denotes nodes, E signifies edges, and their corresponding weighted adjacency matrix W. A node $\mathrm{v_j} \in \mathrm{V}$ is said to be in the neighbourhood of $\mathrm{v_i}$ if there exists an edge in E between them, and these connections are weighted and encoded in W. In graph theory [114], an undirected graph has no directed edges; hence, the connection is bidirectional, from node $\mathrm{v_i}$ to node $\mathrm{v_j}$ or vice versa. Their adjacency matrix is symmetric. Whereas in the case of a directed graph with directed edges, traversal is one way. Their adjacency matrix is not symmetric. A basic structure of graph is illustrated in figure 16. The directionality of the graph matter a lot in facilitating information transfer or message passing [115].

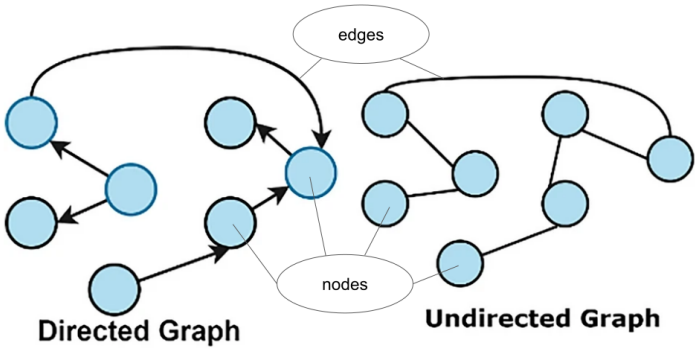

Figure 16: A representation of graph with it's nodes and edges. Each node represents a variable or operations and the edges represent the connection between the nodes [116].

Message passing is one of the fundamental principles underlying graph neural networks, especially Graph Convolutional Networks. It performs an iterative propagation by aggregating information from neighboring nodes and updating the features of every node. It can be mathematically expressed as

$$h[i]^{k+1} = \mathrm{UPDATE}(h[i]^k, \mathrm{AGGREGATE}(\{h[j]^k : j \in N(i)\})) \tag{4.8}$$

where $h[i]^k$ is the feature vector of node i at iteration k, and $N(i)$ denotes its neighbors. The aggregate functions typically include sum (adding neighboring features),

mean (averaging neighboring features), max (selecting the highest feature value) or a combination of these [117]. The update function usually consists of a linear transformation followed by a non linear activation [118]. This combination of aggregation and update allows GCNs to learn the local topology of the graph. Message passing is mathematically implemented in GCNs using graph convolutional filters. It aids GCNs to capture complex patterns and higher-order dependencies across graphs.

Convolutional filters can be categorized into two main categories: spatial and spectral. The spatial domain methods act directly on the graph structure, so information is aggregated from the neighboring nodes. These are usually implemented by message-passing schemes, where nodes exchange information and perform some aggregate operation with their immediate neighbors. Each node performs a kind of filtering operation over its neighbors and extracts the relevant information. A general equation for the convolution on a graph is of the form:

$$h_v^{l+1} = f(\Sigma_{u \epsilon N(v)} W^l \cdot h_u^l + b^l) \tag{4.9}$$

where h_v^{l+1} is the output feature vector of a node v in the $(l+1)$-th layer, h_u^l is the feature vector of a neighboring node u in the l-th layer, $N(v)$ is a set where W^l is learnable weight matrix (filter) for layer l, b^l is the learnable bias term for layer l and f is an activation function. This expression collects input from the neighbors of the node, applies a learnable transformation, and then pushes the computed value through an activation function. Spatial methods have localized operations much like in traditional CNNs but with the advantage of dealing with graphs of various sizes and structures. Few approaches include: Graph Convolutional Networks by Kipf & Welling [118] , GraphSAGE [119], and Edge Convolutions [120].

The other approach is using spectral filters. Spectral convolutions conduct convolution operations on graph-structured data through spectral graph theory [121] based on the eigendecomposition of the graph Laplacian matrix. The normalized graph Laplacian is defined as

$$L = I - D^{-1/2} A D^{-1/2} \tag{4.10}$$

where A is the adjacency matrix, D is the degree matrix, and I is the identity matrix, then decomposed as $L = U \Lambda U^T$ where U contains the eigenvectors and Λ the eigenvalues, for the graph Fourier transform. The spectral convolution operation may be mathematically summarized as mapping a signal x into the spectral domain— that is, $\hat{x} = U^T x$— and then applying a filter in the spectral domain $g_\theta(\Lambda)$, followed by returning it back to the node domain: $y = U g_\theta(\Lambda) U^T x$. A few spectral methods include: ChebNet [122], CayleyNet [123] and ARMA Graph Neural Networks [124]. All of these methods have trade-offs between computational cost, involving a small neighborhood, and their ability to localize the graph signal and capture complicated graph patterns, respectively. While patial filters are highly localized, spectral filters exhibit global support. Having said that, the preference between spatial and spectral

filters is mainly a matter of current application, available computational resources, and desired properties toward graph convolution.

Partition pooling

This technique adapts image recognition architectures-CNN to graph neural networks by defining pooling kernels for graphs [125]. A graph G has nodes and edges. The corresponding node matrix is denoted by h wherein every row h_i represents the feature vector of the node i. The graphs can be segmented into clusters using the K-means algorithm [126] where nodes are grouped based on their proximity to the centroids of each cluster. The resulting clusters/partitions P_i max-pooled using max-aggregation function Q [127] as shown below:

$$y_i = Q(h_j | j \epsilon P_i) \tag{4.11}$$

where y_i indicates the pooled representation of Partition P_i. The aggregation is applied across all feature space resulting in a new graph G' with a new node matrix h'. This pooling can be repeatedly used as shown in section 4.1.3 to reduce the graph size while capturing essential feature information.

$$G \xrightarrow{\text{Q-pool}} G' \xrightarrow{\text{Q'-pool}} G" \xrightarrow{\text{Q"-pool}} .... \tag{4.12}$$

Figure 17 is a schematic representation of partition pooling in graphs. This technique allows for extensive hyperparameter tuning concurrently with less computational demands. In practical applications, for example, simulating the interaction vertices in neutrino detectors, partition pooling enhances the performance of a network while reducing over-fitting with respect to models without pooling mechanisms.

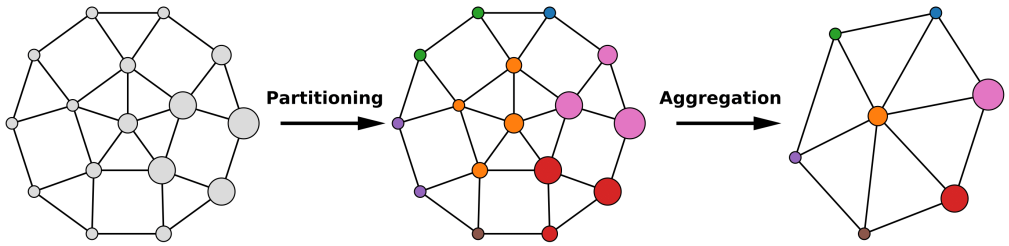

Figure 17: The graph is partitioned using K-Means algorithm and is subjected to max-aggregation. Nodes that belong to the same partition have similar color and their size is proportional to the signal strength [125].

Residual Blocks

These are building blocks of ResNET which is a normalizing method designed to combat the problem of vanishing gradients [128]. As illustrated in figure 18, a unit comprises of several stacked convolutional layers, which form a residual function $F(x)$, where x is the input that is passed on to the unit. The extra connection between the input of a particular layer to it's corresponding output through an identity operator is the key feature of the residual block. The input is added to the interim result before the activation function is applied. The identity operator allows the gradients to be propagated directly, thereby mitigating vanishing gradients problem especially in deep networks. In case of a difference in dimension between $F(x)$ and x, zero padding can be applied or 1×1 convolution can be applied on x as mentioned in [128].

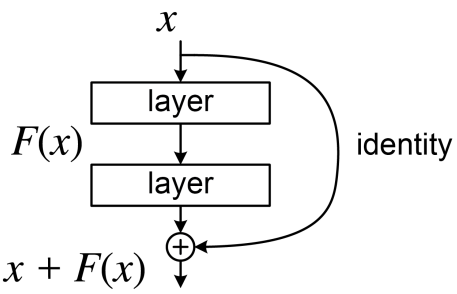

Figure 18: The residual unit is composed of the residual function $F(x)$ and the identity operator. The output at every layer adds up the input x passed through the identity operator [128].

Fully Connected Layer

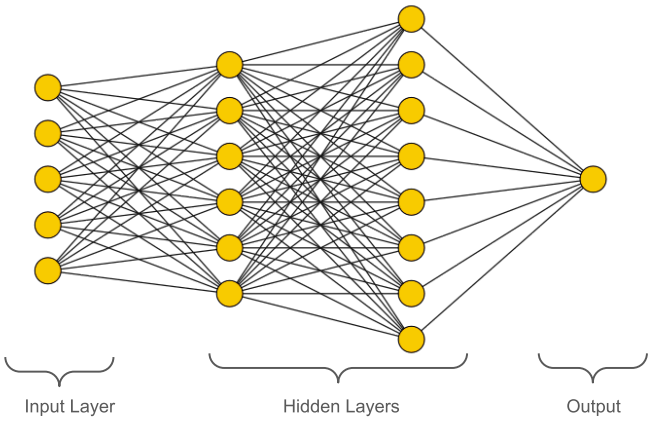

Figure 19: Fully connected dense network where each each neuron in a particular layer is connected to every other neurons in the next layer. This architecture was generated using [129]

This type of network has every neuron in a layer connected to every other neuron in the subsequent layers as illustrated in figure 19. This inter connectivity of the network enables it to process and accumulate information from all previous neurons. These layers are usually are used at the end layers of model to predict the output. After convolutional and pooling layers process features, fully connected layers uses the dense connectivity to transform feature maps to output predictions. Every layer multiplies the inputs by weights and adds biasses followed by an activation function. But in the final layer the activation function is mostly omitted to produce continuous output values.

4.1.4 Role of GCN in Neutrino Event Reconstruction

The typical geometry of a neutrino detector and the data produced from it can be complex. In contrast to traditional neural networks that require a regular grid-like structure for the data, GCNs work by defining convolution operations based on graph topologies and leveraging data structure according to graphs. By representing neutrino detector as graph with the SiPMs (that record the hits) as nodes and their relationships as edges, GCNs can capture the spatial and temporal dynamics of the particles. The addition of partition pooling layers aids in improving the computational efficiency of the model without compromising on the vital data. This makes them a better choice over traditional methods that may not handle large-scale graph data as efficiently, especially in terms of memory usage and processing speed.

4.2 Genetic Algorithm (GA)

GAs are optimization algorithms [130] that use natural evolutionary mechanisms to search for optimal or near-optimal solutions of complex problems [131]. They are based on the concept of biological evolution, which involves the processes of inheritance, mutation, selection, and crossover [132]. GAs are versatile and efficient, requiring no extraneous information like derivatives or continuity, and thus turn out to be applicable to very complicated problems which have discontinuities or non-linearities [133]. By definition, GAs operate on a parallel population and consider many candidate solutions at the same time, which inherently makes them more efficient than the traditional optimization methods like gradient descent that operate sequentially on single candidate solution at a time [134]. They have turned out to be effective in very diverse domains like, medical specialties[135], pattern recognition [136], financial analysis [137], industrial optimization [138] etc. This section will introduce in detail about GA, dwelling on the concepts and basic ideas. The details of the implementation will be given in chapter 6. The following subsections are based on [139] and [140].

4.2.1 Basic Structure of GA

GA operates with a population of individuals, each represented with chromosomes, usually in the form of a string of particular genes (bit, number, or character se-

quence). Chromosomes describe candidate solutions to the solution space for a given problem.

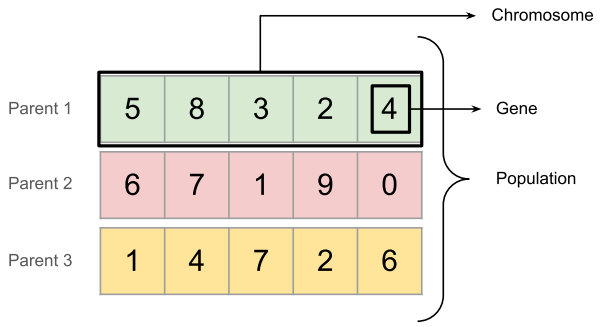

Figure 20: Components of a genetic population. Each individual is identified by their chromosome which is a unique combination of their genes.

The two common representations: binary strings (10101,10001,10010) and continuous variables (45,57,96) with both form encoding the same solution. For this work, continuous variable representations have been chosen due to their appropriateness for the problem.Figure 20 depicts a population and each of its distinct chromosomes, which are made out of genes. The population resides within the search space, which is limited by the domain of the objective function to guarantee that every individual is a valid solution (fitness). The value of each potential solution is established by the particular problem specification. Algorithm 2 describes the working of GA which can be explained in five steps: initialization, evaluation, selection, propagation and termination. The first step is initialization where individuals form an initial population P^0 followed by evaluation where the fitness of the individuals are calculated by the objective function. The third step is selection where the most fit individuals N_{fit} are selected P' for propagating the population. The fourth step is propagation where the selected individuals are propagated using crossover P'', and mutation P''' operators. This process is continued for several generations (iterations) and the population has always the same number of individuals within each generation (iteration). The final step is the termination of the iteration when a stopping criterion is satisfied (which in this case is k=10).

Initialization: The initial population is generated in respect with the requirement of the problem (heuristic initialization). The size of population is one of the most important parameters of the GA, which influences the overall performance. Diversity of the initial population should be ensured to prevent the premature convergence to local optima.

Algorithm 2 GA Workflow

Require: Generate a random population of individuals, P^0, with dimension N_{pop}
Ensure: k = 0
  while k < 10 **do** ▷ For 10 generations
  P' = Apply selection procedure on N_{pop} individuals.
  P'' = Apply crossover procedure on N_{fit} individuals.
  P''' = Apply mutation procedure on N_{fit} individuals.
  $P^{k+1} = N_{pop}$ best individuals of $P^k \cup P'' \cup P'''$
  Set $k = k + 1$
  end while

Evaluation of the individuals: The objective function is the mediator between the GA and the optimization problem. By evaluating the fitness of the chromosomes, at every generation, it ranks these individuals for their relativity towards the optimization problem. The complexity of computing the value of the objective function varies from one problem to another. Suppose, for example, that the fitness function is taken to be Σx_i^2, where x_i is a gene in an individual. Then, the fitness will be calculated by summing up squares of the values of genes as illustrated in figure 21. In some cases, when the mathematical equation is not viable, one can then make use of a rule-based procedure as a fitness function, or a combination of both may be implemented.

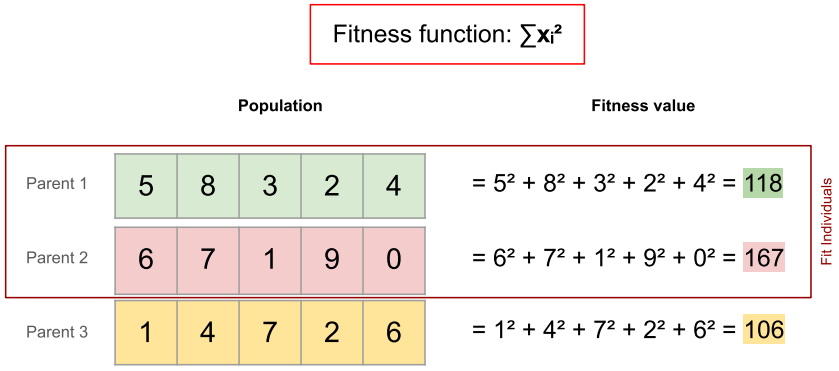

Figure 21: Fitness Evaluation and Selection of Individuals.

Selection: Selection procedure is designed to select individuals from the existing population to propagate and produce offspring. The selection depends on the survival probability, decided by the objective function value of an individual. Again, many selection methods are there, such as ranking-based selection, tournament selection, and elitist selection; the most common one is roulette wheel selection. In the roulette wheel game each chromosome receives a wheel sector proportioned by its value of

fitness; the higher the evaluated chromosome, the larger the sectors. The problem taken for this study is a maximization problem; therefore, individuals with higher fitness are more likely to survive and reproduce, while those with lower fitness are eliminated. From a population of N_{pop} individuals, the number of individuals retained, forming the subset N_{fit}, is based on their fitness value. Based on the example depicted in figure 21, three individuals make up the initial population. Their fitness is evaluated using the fitness function: Σx_i^2 and those with higher fitness values (Parent 1, Parent 2) are selected to continue the propagation.

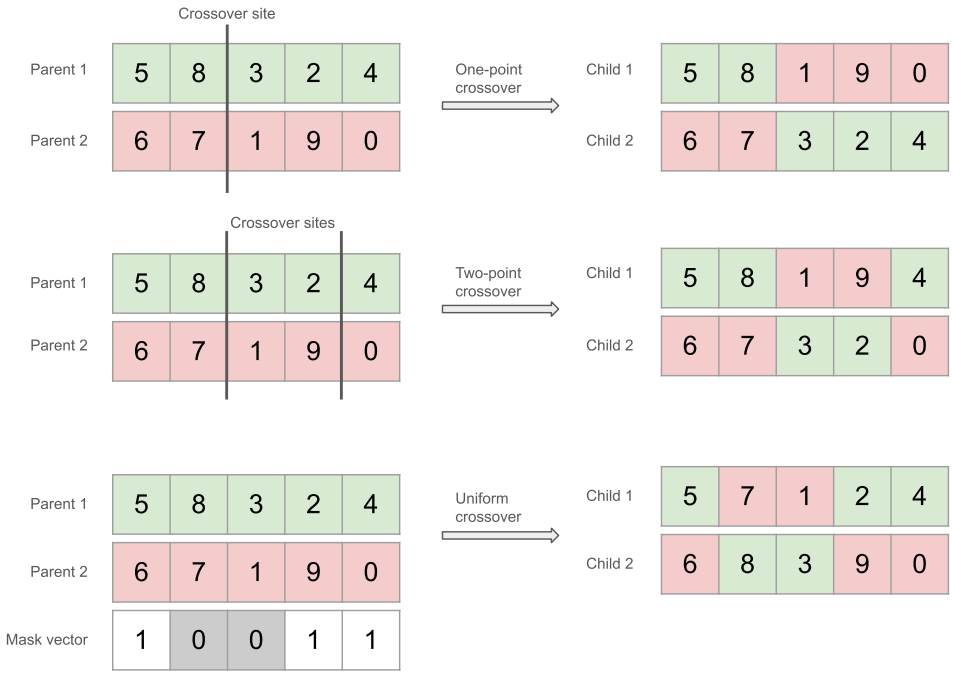

Figure 22: Illustration of one-point, two-point and uniform crossover operators.

Propagation through Crossover: This main operator P'' recombines the parental traits from the parents chosen from the subset N_{fit} and transmits them to the new generation (offspring). The most common modes of crossovers are represented in figure 22, and details are given below:

1. One-point Crossover: A particular point in the chromosome of both the parents are chosen. They are sliced at this point and the corresponding segments are swapped to generate the new offspring.
2. Two-point Crossover: Two points are selected randomly and sliced. This would divide the parents into three sections. The segment between the points are interchanged to form two new offsprings.
3. Uniform Crossover: In this type a binary mask will decide the segments that are to be interchanged. If the mask contains 1, then the gene from the first parent is copied and when it is zero the gene from the second parent is copied to the offspring. This

is how the first offspring is bred. The mask is swapped to produce the second offspring.

Propagation through Mutation: The mutation procedure, P''', is a rare phenomenon in natural processes but can help diversify the existing population. Not all individuals undergo mutation. A fixed number of individuals from the N_{fit} subset that will undergo mutation based on the mutation probability rate. These individuals are chosen randomly, and their values are then replaced with new random values. For example if a second gene in an individual is chosen to undergo mutation, as shown in figure 23 then it's replaced with a random new value. This approach assists the algorithm to alter the search and introduce new genetic structures. In this way it prevents premature convergence to a local minima. However, the probability of mutation should be maintained relatively lower than the crossover probability else it would turn the algorithm into a random search.

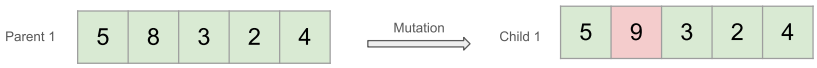

Figure 23: Illustration of mutation of an individual. A random gene position is selected and altered to produce the offspring.

Termination: The termination can happen when a specified number of generations have been completed with no improvements in the fitness value after a certain generation or if all individuals in the population narrow down to the same solution. When the stopping criterion is met and the new generation is evolved, the old generation can be discarded.

4.2.2 Role of GA in Optimizing Horn Geometry

GAs operate with a population of solutions simultaneously, therefore it effectively finds the global optimum contrary to methods that find single solutions. By fine-tuning parameters such as population size, crossover and mutation rates and by selecting the more fittest individuals for propagation, GA ensures a balance where there is sufficient diversity to thoroughly explore the search space, yet also to converge towards optimal solutions. Furthermore, as the population progresses, the algorithm automatically assess and propagates new individuals. However, their convergence rates are slow as compared to traditional optimization methods like gradient based

methods [141]. Despite this, they have an advantage of scaling up or down the population size and the generations to fit to the problem statement. They are hence good at dealing with high dimensional problems that are hard to optimize by hand. All of the above mentioned reasons justify the fitness of GAs in analyzing complex profiles with multiple parameters like those of horn geometry. Details of implementation is in chapter 6.

5 Event Reconstruction

An event is a single interaction or group of related interactions detected within the detector. These events have properties like particle types, energies, momenta, and vertices (interaction points). But detectors are not measuring these properties directly; they capture signals from various components as particles interact with the detector material. The raw detector signal is reconstructed to recreate, as accurately as possible, the original event properties that were collected in the detector data. This process uses complex algorithms to determine the vertex and energy of the events or even identify the particles. This chapter explains in detail from the particle interactions to the reconstructed parameters, focusing on the key aspects: simulation, data generation, vertex and energy reconstruction. It starts with a simulation phase where the Monte Carlo (MC) techniques are used to simulate the particle reactions inside the detector. This is then followed by the generation of data, that is, the conversion of these simulated particle interactions into realistic detector signals reflecting the interaction of particles with detector elements. The final step is the event reconstruction: the algorithms and methodology required to determine the vertex and evaluate the energy of the primary particle interactions. The ultimate goal is to reconstruct the spatial coordinates and deposited energy of neutrino interaction events from SiPM hit times and counts. This study, however, mainly concerns the reconstruction of positron events. The positron reconstruction lays the groundwork for understanding the response of the detector and developing subsequent algorithms which will be applied to the full neutrino event reconstruction in the future. The vertex reconstruction aims to find the vertex resolution that is crucial in applying fiducial volume cuts in the detector. The Energy reconstruction aims for a resolution of less than 2 % at 1 MeV helping to accurately measure the antineutrino spectra of the reactor.

5.1 Simulation

The TAO offline software is conceptually designed to use the Software for Non-collider Physics Experiments (SNiPER) framework [142] and is built upon on the existing JUNO software [143]. It handles software units (Geant4, ROOT, I/O), job profiles, and events and offers extensible data schemes and concurrent processing capabilities. The core utilities such as Geant4 [144] and ROOT [145] facilitate the simulation and analysis of data, respectively. It handles software units, job profiles, and events and offers extensible data schemes and concurrent processing capabilities. The existing framework of the JUNO software provides a significant advantage in constructing TAO offline software, as both are LS detectors, the existing modules can

be adapted and tailored to meet TAO's dimensions and other needs. The complete layout of the TAO offline software with the above details is shown in figure 24 and it contains some modules from the JUNO offline software, newly added modules from the TAO offline software, the SNiPER framework and a few External Libraries. The modules in the JUNO software include:

1. Generators like GENIE [146], which handles the neutrino interaction with the target matter and simulates the corresponding secondary particles.
2. Simulation uses Geant4 for modeling detector geometry, physics processes like electromagnetic, decay physics, hadronic, optical, and special processes tailored for accurate neutrino interaction and background event modeling and photon propagation. In short, Geant4 handles the propagation and interaction of the neutrino"s secondaries and the subsequent emission, propagation and detection of optical photons.
3. Calibration handles the energy scale calibration and detector response corrections by processing data from multiple radiactive sources using the ACU and CLS.
4. Reconstruction processes the data to reconstruct energy, vertex, waveform, charge distribution, particle tracks, and directional information.
5. Analysis handles the event selection and statistical analysis of the data to identify IBD candidate and assess the reactor antineutrino spectrum.

The JUNO Offline Software is a framework developed for a wide variety of non-collider physics analysis problems, supporting complex analyses in solar and atmospheric neutrinos, while utilizing general reconstruction algorithms and flexible data processing workflows. TAO is focused explicitly on reactor antineutrino detection and as such employs specialized reconstruction algorithms, dedicated calibration methods specific to liquid scintillator response, and statistical analysis tools aimed at precision measurements of the flux. The TAO software uses the same modules with the following key adaptations: simulation of a smaller liquid scintillator detector (diameter = 1.8 m) with higher resolution ($< 2\%$ @ 1 MeV), reconstruction algorithms altered to SiPM readouts and calibration procedures at an operating temperature of $-50°$C.

The simulation module in the TAO offline software consists of three essential components: the physics generator, the detector simulation (Detsim), and the electronics simulation (Elecsim). The physics generator produces wide variety of event types including signal and background processes. It produces antineutrinos from the reactor core and gives initial conditions and particles required for interactions with the detector by providing random first particles with respective properties and generates first events according to physics models. Simultaneously, it also produces background events like atmospheric neutrinos, natural radioactivities, cosmic muons and their induced backgrounds as shown in table 2. DetSim utilizes Geant4 to model the overall detector response to the generated particles. It includes the overall structural particulars of the TAO detector such as the geometric specifications of the detector (inner diameter of 1.8 m, volume of about 2.8 tons, 10 m^2 coverage of SiPMs) and the

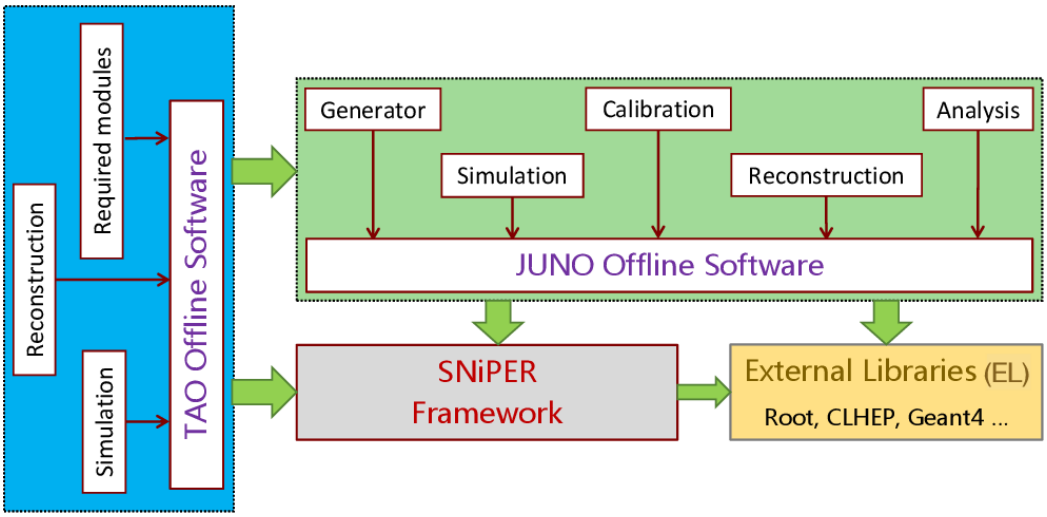

Figure 24: Components of the TAO offline software [10]. The JUNO Offline Software is a data processing environment with components of physics generators, detector simulation, and event reconstruction. The TAO Offline Software that has been tailored specifically for reactor antineutrino detection utilizing similar structures to JUNO Offline Software but focusing on the unique requirements of the TAO experiment. The SNiPER Framework serves as the backbone for the software of both JUNO and TAO providing an extensible architecture for efficient event data management and the External Libraries that consist of mainly Geant4 for simulating interactions of particles and ROOT for data handling and visualization.

main material properties (GdLS) as well as the optical parameters (absorption and re-emission probabilities of GdLS, 50% PDE) that are essential for accurate simulation. It also incorporates the basic physics process that controls particle interactions, follows the motion of particles throughout the detector volume, and energy deposition as well as scintillation light generation. Moreover, DetSim simulates the optical photons, their propagation and detection with SiPMs. ElecSim is mainly concerned with mimicking the response of the TAO readout electronics. It contains several important components, such as SiPM photon counting, signal amplification and shaping as well as the analog to digital conversion. However, for this study Elecsim was not utilized since it was still in the development stage. This choice will lead to better results than expected due to absence of the electromagnetic response of the detector.

The events are initiated by an injection of positrons with energies from 0 to 10 MeV. After creating the primary particles, the simulation next tracks their energy loss in matter, taking into account of various process including ionization and excitation that leads to the production of scintillation photons. Alongside scintillation, Cherenkov photons are produced when the charged particle travel faster than the speed of light. In the process, when a positron deposits its kinetic energy E_{kin}, it annihilates with an electron to produce two 511 keV gamma-rays. These gammas in principle interact with matter over photo effect, compton effect and pair production and hence produce

additional scintillation light. The photons are then propagated through the detector, incorporating the key optical processes like Rayleigh and Mie scattering. The scattering along with the absorption and re-emission has an impact in the overall light yield in the LS. When the photon reaches an SiPM tile it can generate a photoelectron. Every photoelectron that is detected is accounted as a hit. Around 4500 photoelectrons are detected for 1 MeV of deposited energy at the center of the detector. Although, this number can vary with statistical and systematical effects, like non-linearity of liquid scintillator, variation of detector response, etc. Hits on SiPMs are used to integrate the total charge and save it together with the time of the first hit as a SiPM signal. The time of the first hit on each SiPM is registered, with the time starting from when the event was generated in the simulation. The charge from all subsequent hits are aggregated to provide a detailed measure of the light detected during an event. The information regarding the events are stored as Event Data Model (EDM) [10] which provides a solid structure for processing and analyzing the data.

The TAO EDM is used to store all the information on the event data in the form of ROOT-based persistent data objects. These data objects are processed and passed through various stages and applications of the TAO offline software. The key types of event data includes: SimEvent (from detector simulation), ElecEvent (from electronics), CalibEvent (from calibration), and RecEvent (from reconstruction). For this study, only SimEvent is utilized. It contains initial particle information, interaction vertex, deposited energy, hit information, time stamps, and track information of the fired SiPMs and the MC truth information of each particle. In addition to organizing complex data, the model also has the ability to display the event in 3D mode shown in figure 25, as well as 2D projection mode. As shown in the figure, the event's graphical output consists of the interaction of gamma rays in the detector itself, with fired SiPMs and hit patterns shown on the left. The right part of the panel contains functional buttons for users to control parts of the visualization, like whether or not to display detector geometry, how to adjust the views of the events and which parameters to analyses. This interaction interface promotes the exploration of a wider range of physics, as users can adjust events as they are being visualized in the event display in real-time, leading to an increased understanding of both physics and detector performance.

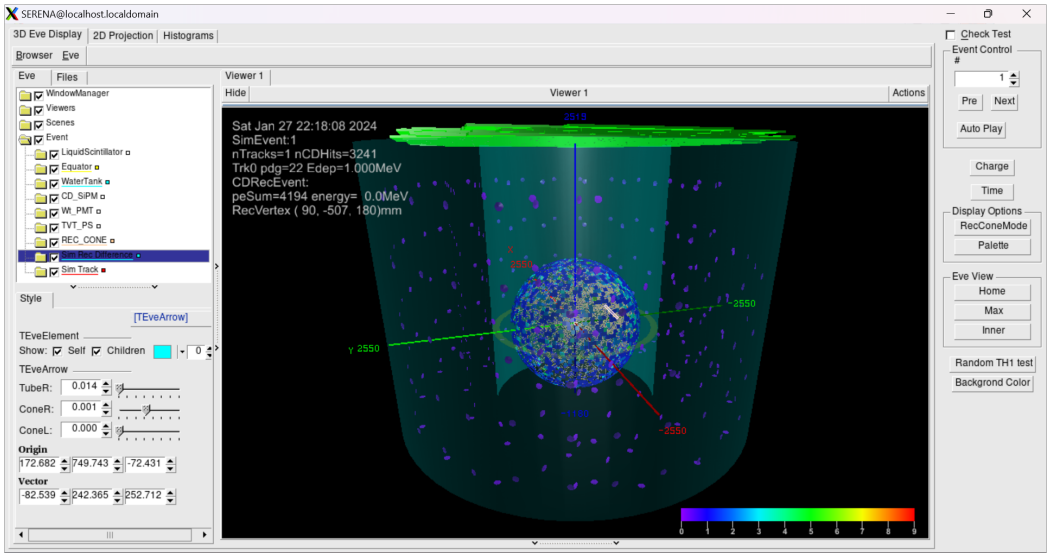

Figure 25: The TAO event display software displaying a gamma event. The visualization effects of the event and detector components can be controlled on the right panel through the functional buttons available [147].

5.2 Data Generation

In an IBD event, an electron antineutrino interacts with a proton, producing a positron and a neutron. The positron produces an immediate signal, while the neutron undergoes delayed capture. In this study the focus is on positron events which makes the analysis simpler by demonstrating on the immediate visible signals that are relevant to the IBD interaction. Neutrons will be incorporated in a future analysis. This two step approach enables a comprehensive understanding of reactor antineutrino interactions by first establishing a framework on the prompt positron events followed by deeper understanding of the neutron's role in improving event characterization. The event data for training, validation and testing of the neural network were generated from Monte Carlo samples, produced with the official TAO offline software. The data is structured as:

1. Training and Validation Dataset: A dataset containing 5 million positron events with kinetic energies ranging from 0 to 10 MeV was generated with the events uniformly distributed across the central detector volume. For this study, 70% of the data is used for training while the other 30% is used for validation. The model learns the correlations between the event variables and the prediction during training. The performance of the model is evaluated during validation and with the obtained information the hyperparameters are fine-tuned.

2. Testing Dataset: Subsets of discrete kinetic energies with each subset, containing 10,000 events were generated. The energies include 0 MeV, 0.1 MeV, 0.3 MeV, 0.6 MeV, 1 MeV, 2 MeV, up to 10 MeV. This independent dataset is used for the final evaluation of the model performance after completion of training and validation. The discrete energy subsets enable precise benchmarking of the performance of the model

at specific energy points. This allows to detect possible biases or limitations of the model predictions.

The aim of the reconstruction task is to determine the total energy deposited by each positron and associated gamma rays, $\mathrm{E_{dep}}$ and the interaction point of this energy deposition $\mathrm{x_{dep}}$, $\mathrm{y_{dep}}$ and $\mathrm{z_{dep}}$ using the information about first hit timings and the number of hits. An event display of a positron event with deposited energy of 1.512 MeV is shown in figure 26. The grey sphere represents the primary vertex or the initial interaction point of the event. The left plot with is a depiction of the fired SiPMs giving the details of the number of hits. The right plot depicts the first hit time with lighter blue shades indicating first hit arrivals. The timing information is important to build the time profile of the event and for tracing interaction sequences within the detector. These visualizations provides an understanding of the event properties.

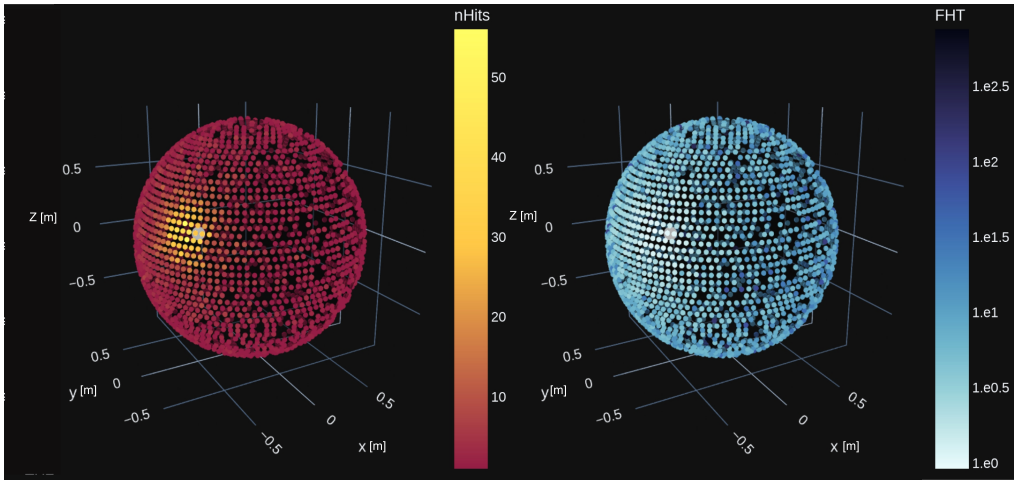

Figure 26: A positron event with deposited energy of 1.512 MeV. Only fired SiPMs are shown. (Left) Distribution of the number of hits with yellow points representing more hits and red points representing fewer hits. (Right) The first hit time (FHT) is represented where the lighter blue represents earlier first hit arrivals. The grey sphere represents the primary vertex.

5.3 Reconstruction

This sections explains in detail the vertex and energy reconstruction process, including the architecture, the optimizations done to train the data and the obtained results. The vertex and energy reconstruction were carried out independently, however both utilized the same underlying architecture and a nearly identical set of hyperparameters. This approach produced better results over their combined reconstruction.

5.3.1 Vertex Reconstruction

Motivation: The goal of vertex reconstruction is to determine the spatial coordinates of the interaction point of an event using its first hit time information and hit counts from SiPMs. These coordinates provide only one single point where the interaction occurred and not a track. The reliability of these reconstructed vertices is quantized using the vertex resolution – an attribute that shows the proximity of the reconstructed positions to the true interaction points. Precise localization of the interaction points within the detector volume is important for applying fiducial volume cuts that can help to reject background events occurring at the edges while maximizing the usable detector volume. Given that TAO will serve as a reference detector for JUNO, accurate vertex reconstruction is an important aspect in the delivery of a high-quality model-independent reactor antineutrino spectrum.

Architecture: The architecture uses GCNs and is implemented using the Pytorch [148] environment and contains several specialized layers like graph convolutional layers, pooling layers, and residual blocks as shown in figure 27. The spherical graph in the figure is designed with dimensions as that of the detector, with 4024 nodes that represent the SiMPs. Each of these nodes has two features: the first hit time and the number of hits, which are the input to the network, hence the shape of the input (2D tensor) is 4024x2. The graph is passed through graph a convolutional layer. Here, the dimension of the features is increased say for example, from 2 to 8 in the first step and the modified shape is 4024x8. This allows each nodes to learn eight features based on the aggregated information from the neighbouring nodes instead of two initial parameter. Following the convolution are the residual blocks that contain skip connections and maintains the shape as it is. They also have dropouts implemented that help in regularizing the network from overfitting. Next is the partition pooling layer that clusters the graph by grouping the nodes. In this way, the number of nodes are reduced but the feature dimension remains the same. Hence the shape results to 804x8 after first pooling as per figure 27. This layer helps in reducing the dimensionality while enabling deeper networks and fewer uses of computational resources. The graph passes through four stages of convolutions and three poolings with residual blocks in between. After fourth convolution the graph is flattened to a fully connected layer, it's converted from a 2D tensor to 1D (this reduction in dimensionality reduces the computational complexity). This linear layer yields the output: x, y and z coordinates.

Optimization: To improve the performance of the architecture several hyperparameters are tuned during training. These parameters together decide the training process: they specify how long to train, learning speed, how much to regularize and what kind of optimization would work. One has to find the best tuned configurations that optimizes the model and provides most accurate predictions. For the vertex reconstruction, the model was trained over 39 epochs. Early stopping was introduced

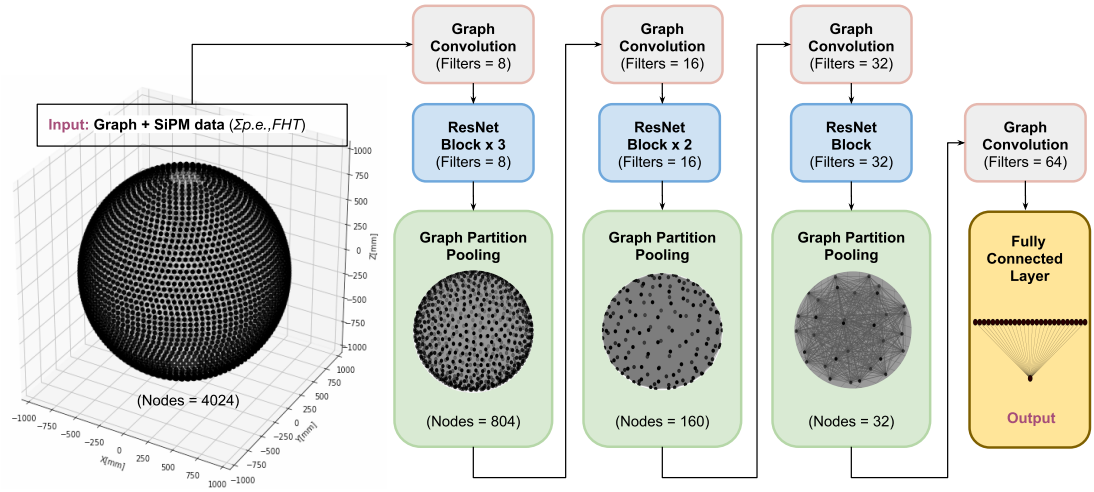

Figure 27: Architecture used for reconstruction. The graph with its features (SiPM data) is fed as input into the NN. The first layer is a single graph convolution layer where the feature dimension is indicated using filters. Following all convolutional layers are residual blocks that vary across the network. After every residual unit is a partition pooling layer that reduces the number of nodes. After the fourth convolution the graph is flattened to a fully connected layer with linear activation that outputs the three vertex coordinates x,y,z.

during the training with a patience of six. This halts the training if the model's performance doesn't improve for six consecutive epochs. The entire training data was processed in batches of hundred events so that model can update the parameters frequently in these mini batches instead of the entire data. The model uses Adam optimizer and the initial learning rate is set to 0.005, with a dropout of 25%. This means in every training iteration 25% of neurons are randomly deactivated aiding the model to learn more robust features. The parameters are summarized in table 3.

The model uses MSE as the loss function. It calculates the mean squared error of 3D vertex reconstruction based on both true $(V = (x, y, z))$ and reconstructed $(V' = (x', y', z'))$ vertices.

$$\text{MSE} = \frac{1}{3}\left[(x - x')^2 + (y - y')^2 + (z - z')^2\right] \tag{5.1}$$

The above formula calculates the average squared differences between true and reconstructed coordinates across three dimensions. This scalar measure gives detailed information on reconstruction accuracy and lower values indicate better performance.

Training parameter	Selection
Batch Size	100
Epochs	39 (33)*
Early stopping (patience)	6
Learning Rate	0.005
Dropout	0.25
Optimizer	Adam lr 1.e-4.

Table 3: Tuned hyperparameters used in the training. *Is the changed parameter in the energy reconstruction.

MSE is useful in vertex reconstruction because of the squaring; the larger errors are penalized more, and it treats all spatial dimensions equally. In training, MSE guides the optimization such that the cumulative difference between true and reconstructed vertex positions is minimized while achieving highly accurate 3D reconstruction for the vertices.

Training and evaluation: As mentioned in section 5.2, 3.5 million events were trained and 1.5 million events were validated. The training and validation losses were monitored to ensure better learning. As shown in figure 28 the initial 34 epochs show decreasing loses, however the losses become nearly identical from epoch 35 onward. The convergence of losses suggest that the model has reached an optimal point and performs equally well on training and validation data. After 39 epochs a slight overfitting was observed and hence the training was stopped here. The trained model now is evaluated on test dataset, with a focus on the 1 MeV subset. The evaluation involves comparing the the model predicted vertex positions with the true positions and evaluating the biases and resolutions. The 1 MeV subset is a good checkpoint to access the model's ability to handle low energy signals against the background noise and to provide an insight into model's real-world applicability.

Results: The optimized architecture is trained and evaluated to provide the reconstructed vertices. Initially, the predicted values are compared to the true values to assess the model's accuracy. As shown in figure 29 the true values of the vertices (x,y,z) show a strong linear correlation with their corresponding predicted values. Furthermore, the narrow width of the distribution indicates a high resolution, reflecting the model's effectiveness in capturing the underlying physics. Since the model appears to effectively predict vertices, the next step is to analyze the distribution of these predicted vertices. The distribution, of the vertices can help in identify if there are any biases or deviations in the predicted values that can imply areas for improvement in the model. The detector response and inherent measurement uncertainties associated with particle interactions may also be inferred from the shape and spread of the distributions. A histogram, representing the distribution of the differences between the predicted and true coordinates are fitted with a Gaussian function that

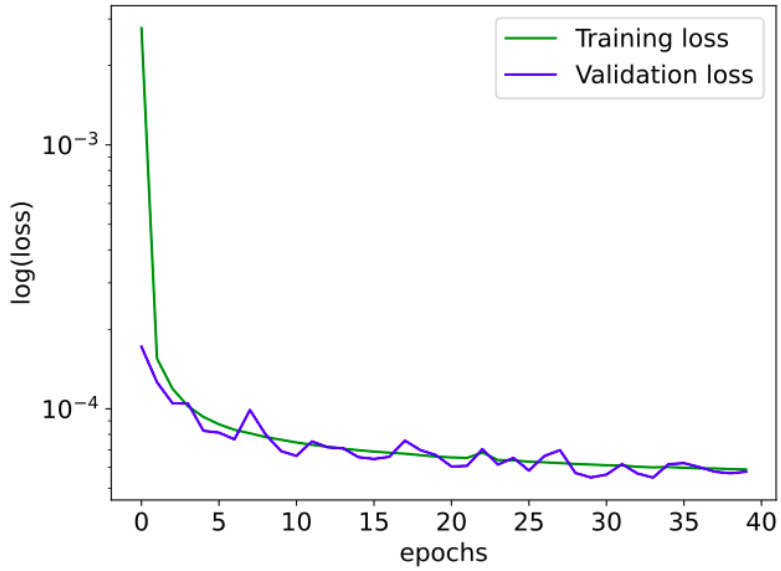

Figure 28: Training (green line) and validation loss (blue line) over number of epochs. An initial drop suggests that the learning has began and with increasing epochs the validation loss converges around the training loss.

provides two key parameters, the mean (μ) and the standard deviation (σ). The mean represents bias in the reconstruction and the standard deviation quantifies the resolution of the vertex. A mean close to zero represents an unbiased reconstruction and a smaller standard deviation indicates that the model reconstructs the vertex close to its true values. The Gaussian fit not only provides the above information but also helps in understanding systemic effects. Any deviation from the Gaussian could indicate non-linear effects in the reconstruction process or potential biases in specific detector regions. With the current model, the vertex resolution obtained at a low energy of 1 MeV is shown in figure 30. The closeness of the mean in the obtained results suggest the reconstruction is unbiased across the detector volume. The resolutions of each coordinates are: x = 7.995 mm; y = 8.366 mm; z = 7.868 mm. The achieved resolution of approximately 8 mm at 1 MeV looks promising especially considering the challenges in reconstructing low energy events.

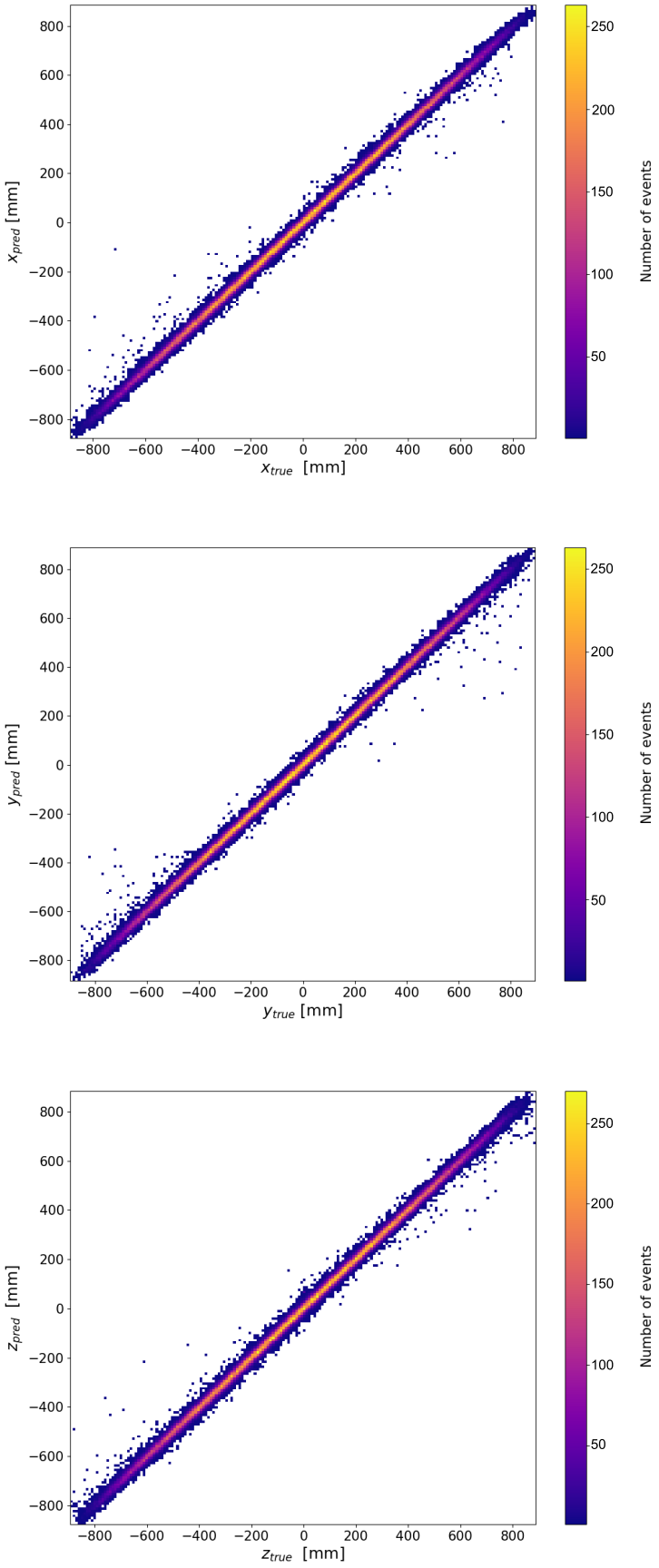

Figure 29: Comparision of the true and predicted values of vertices (x, y, z). The predicted values shows a clear linear trend, suggesting that the model's predictions align closely with actual measurements.

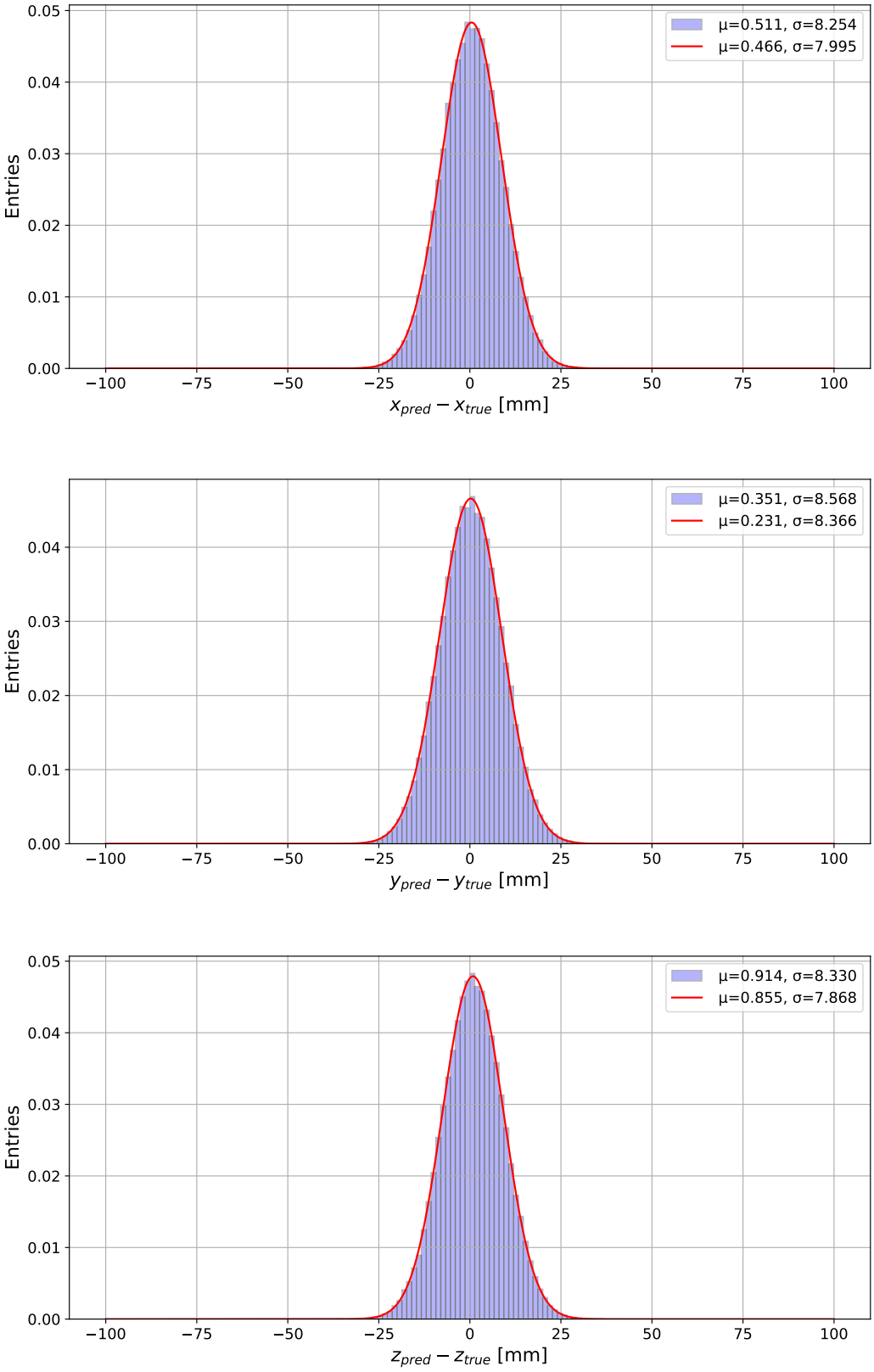

Figure 30: Difference between the predicted and true event vertices for each coordinate x (top), y (middle) and z (bottom) at 1 MeV. The distributions are fitted to a gaussian and the sample mean μ and the standard deviation σ are indicated in the graphics. The fitted σ value is the resolution of the vertex.

Determining the radial distance $\mathrm{R} = \sqrt{\mathrm{x}^2 + \mathrm{y}^2 + \mathrm{z}^2}$ of each vertex from the origin can be helpful in understanding the spatial distribution of vertices throughout the detector volume. The distribution of the differences of the true and predicted R values, fitted to a gaussian is shown in figure 31. The distribution shows a resolution of 9.536 mm is obtained at 1 MeV. This resolution is vital for applying the fiducial volume cut, a selection criteria to eliminate events near the detector boundaries. In this case, the cut excludes events within a range of 10 mm from the detector walls. Applying the cut would aid in reducing the background events and improve data quality for analysis.

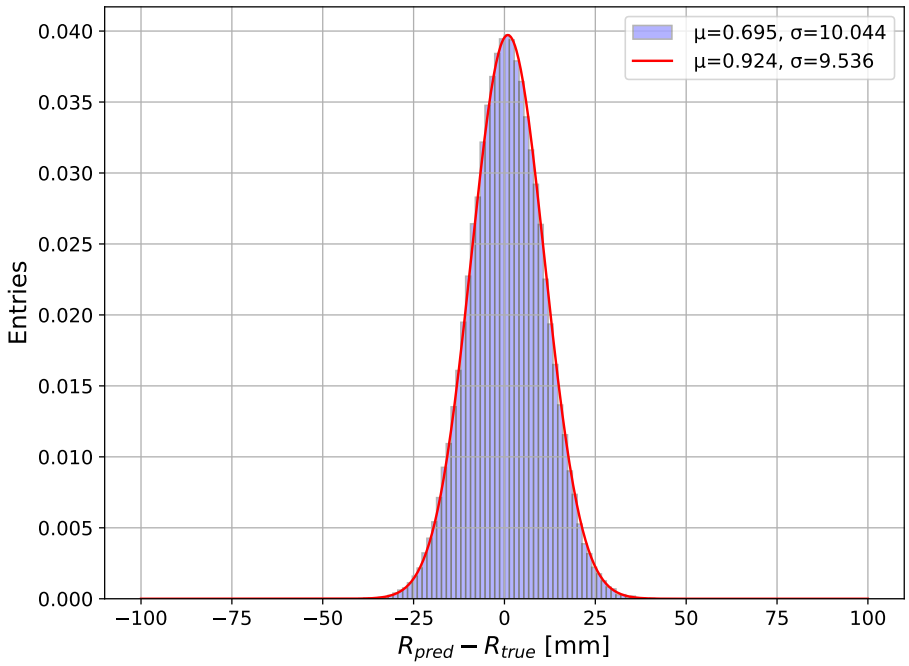

Figure 31: A histogram of the differences between true and reconstructed R at 1 MeV, fitted to a gaussian. The width of the gaussian determines the resolution.

Also, a visualization of how well the model's predicted values match with the true values across the detector volume can be useful to study the spatial performance, highlighting areas of good or poor reconstruction. Figure 32 is a 2D heat map that compares the differences between $\mathrm{R}_{\mathrm{pred}}$ and $\mathrm{R}_{\mathrm{true}}$ in the detector volume $\mathrm{R}^3_{\mathrm{true}}$. The color map to the right represents the number of events. The central yellow band indicates that the events in this band are those whose predicted values are close to the true values. This band is distributed almost in a similar fashion across different detector regions, suggesting that the reconstruction algorithm worked quite well across different detector regions. However, there are also other scattered points above and below the yellow band that indicates a deviation of the predicted values from the true values. In summary, the vertex reconstruction is largely unbiased across the detector geometry.

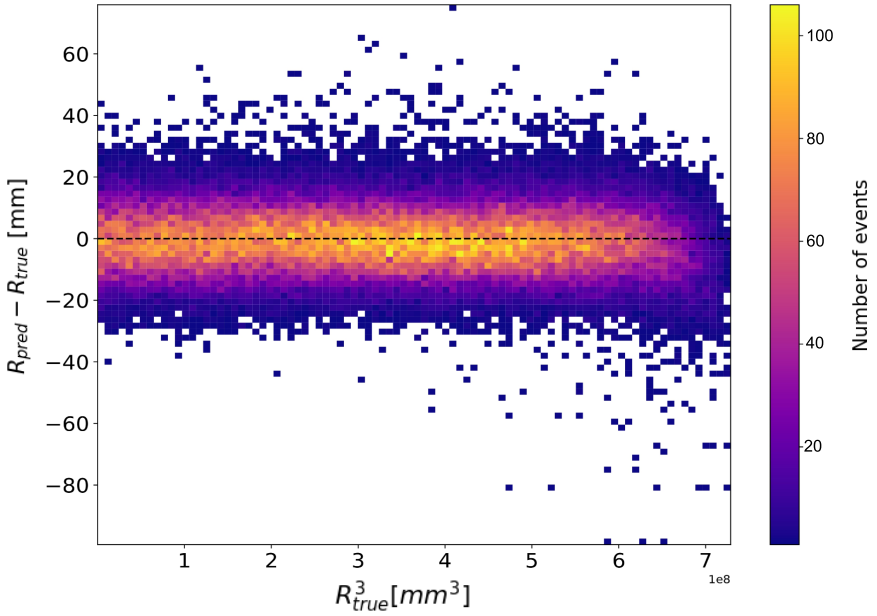

Figure 32: Heatmap of $\mathrm{R}_{\mathrm{pred}} - \mathrm{R}_{\mathrm{true}}$ versus R^3 for events at 1 MeV. The cental yellow band indicates events whose predicted values closely match the true values. The uniform distribution across the detector volume shows unbiased reconstruction.

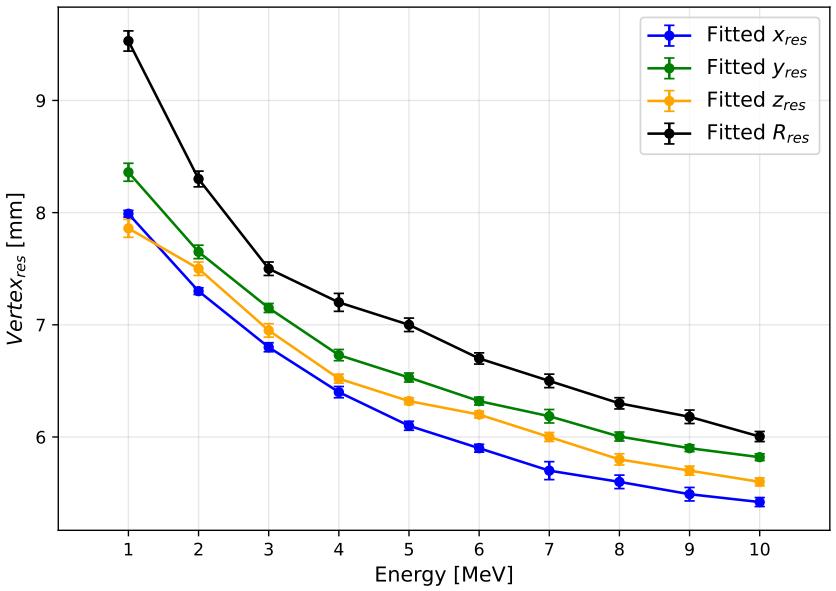

Figure 33: The plot illustrates the relationship between energy (measured in MeV) and vertex resolution (measured in mm) for the reconstructed coordinates x, y, z as well as the overall radial resolution (R).The individual resolutions for x, y, and z coordinates show a consistent improvement with increasing energy. The radial resolution which combines the contributions from all three dimensions, also reflects this trend.

Vertex resolutions were studied for the different positron energies. Figure 33 shows the resolutions of vertices x, y, z and the radial distance R across the positron energies. Here, the fitted resolutions for x, y, z, and R indicate improved precision in locating the interaction vertices as energy rises. At higher energy, the positron ionizes more because it interacts more with the material in the detector. This results in an increased number of hits in the tracking detectors. This improves the signal-to-noise ratio, allowing a more precise reconstruction of positron trajectories and, thus, vertex positioning.

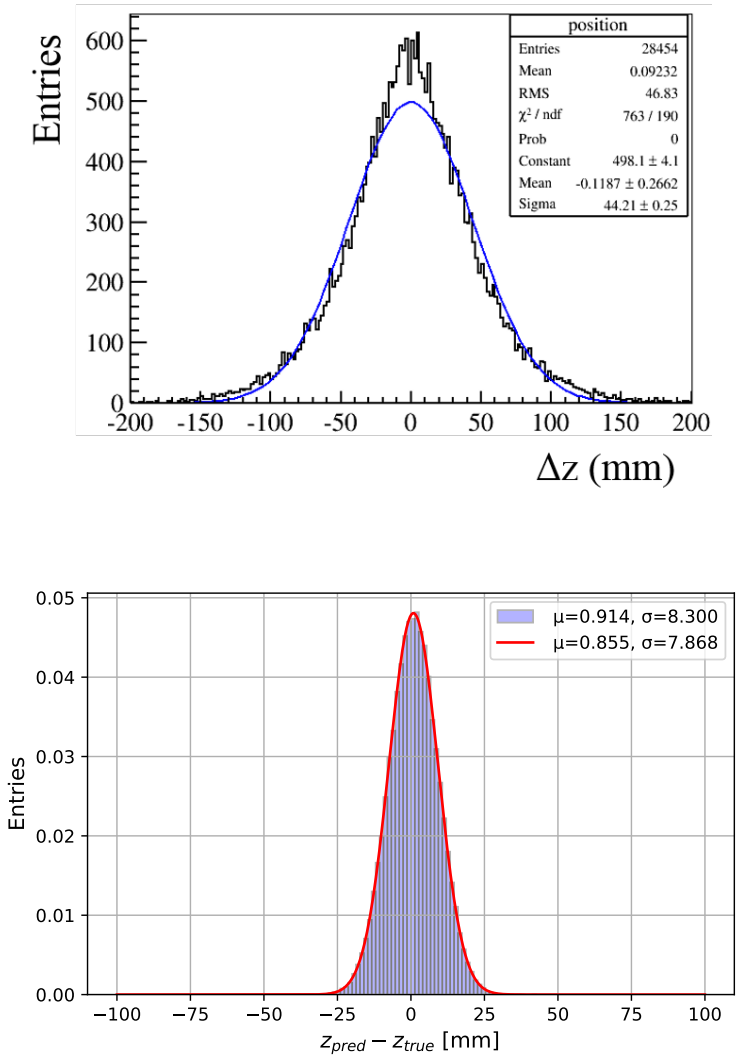

Figure 34: Comparison of the z_{res} obtained from center of charge method (using neutrino events) [10] and GCN (positron events). The GCN achieved a better resolution of 7 mm as compared to center of charge method that obtained 44 mm.

In order to evaluate the obtained vertex resolution, the current method was compared to the center of charge method as discussed in [10]. In the center of charge recon-

struction, the amount of charge collected from ionization events is used to determine the location of an interaction vertex. In this approach, the detected signal then becomes a point that contributes to the position of the vertex (weighted by charge) with the goal of achieving an optimal weighted average of what is supposed to be the true position of the vertex. Nonetheless, the reconstruction results obtained via GCN method gave better results than the charge-center method. As shown in figure 34 the z_{res} obtained from the charge center method is 44 mm while the GCN shows an improved resolution of 7 mm. However the charge center method used neutrino events and the GCN used only positron events. The obtained resolution is expected to decrease when neutrino events are considered.

5.3.2 Energy Reconstruction

Motivation: The prime aim of energy reconstruction is to predict the energy deposited at the interaction point. Precise reconstruction of the deposited energy is vital for accessing the detector's energy resolution. By achieving an excellent resolution below 2% at 1 MeV TAO would aid in measuring the energy spectrum of the rector antineutrinos and provide a model independent reference spectrum for JUNO.

Architecture: The same architecture as represented in figure 27 was used. The only difference is that the model was fed with deposited energy E_{dep}, obtained from the simulation. Hence, the output of the model was the prediction of the deposited energies E_{pred}.

Optimization: The parameters used for optimization were similar to those used in the reconstruction of the vertex, as shown in table 3 except for the number of epochs. However, the loss function used for energy reconstruction was the Cross-entropy loss. This was preferred over MSE loss as the former handles the nonlinear, probabilistic nature of energy measurements in complex detectors. For continuous energy distributions, the loss is calculated as:

$$L = -\int p_{\text{dep}}(E) \log(p_{\text{pred}}(E))\, dE \tag{5.2}$$

where, $p_{\text{dep}}(E)$ is the true deposited energy distribution, $p_{\text{pred}}(E)$ is the predicted energy distribution, E represents the energy and the integral is taken over the entire energy range. The goal is to minimize the loss during training so that the predictions closely match the true distributions.

Training: The training was also carried out in similar fashion and the training and validation losses where monitored for different epochs. The comparison of training and validation losses are shown figure 35. The initial epochs show decreasing training loss with validation loss fluctuating around it. However, the validation loss tend to converge around the training loss from epoch 25 onward. The convergence of losses

suggest that the model has reached an optimal point and performs equally well on training and validation data. The training was terminated at 33 epochs to prevent overfitting.

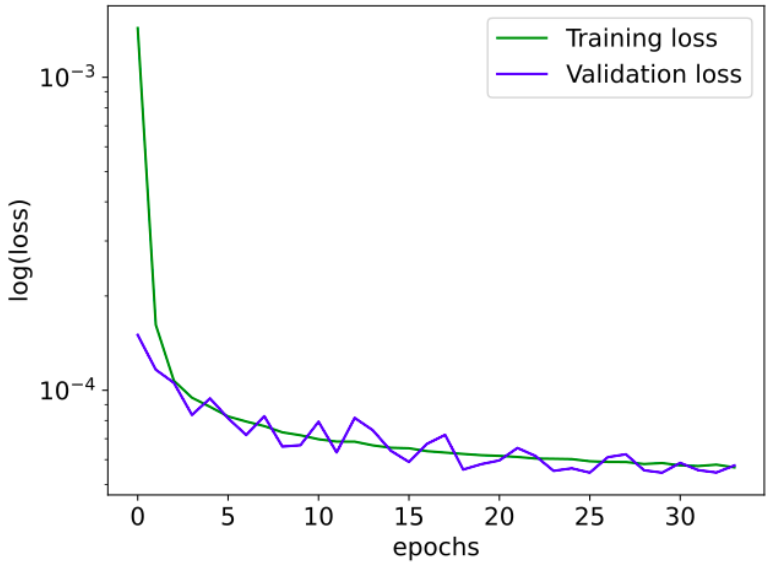

Figure 35: Training and validation loss vs. epochs for energy reconstruction. The initial decrease in training loss is accompanied by fluctuating validation loss. From epoch 25, both losses converge, indicating optimal model performance.

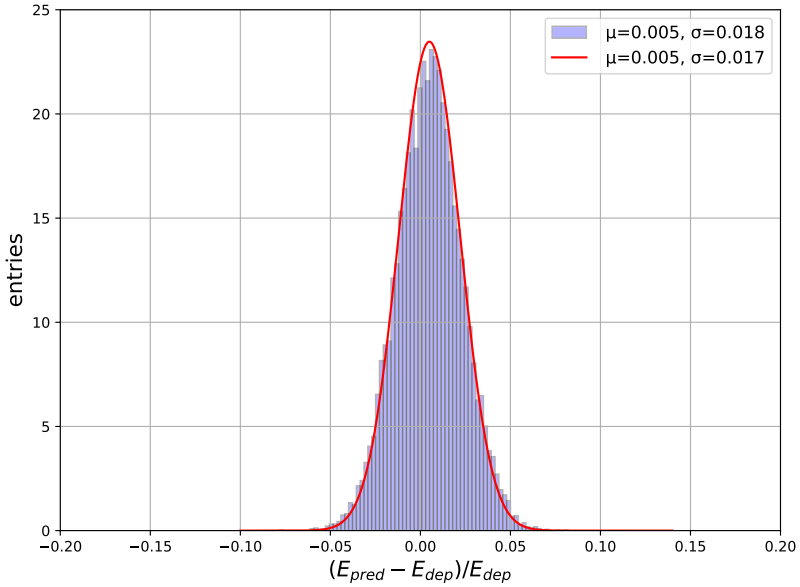

Figure 36: Distribution of energy resolution at 1 MeV, fitted to a Gaussian. A slight positive bias is observed.

Results: With the model prediction, the true and predicted values are compared. The energy resolution is calculated as:

$$E_{\text{res}} = \sigma \left(\frac{E_{\text{pred}} - E_{\text{dep}}}{E_{\text{dep}}} \right) \times 100 \tag{5.3}$$

where the σ is determined from the histogram of $(E_{pred} - E_{dep})/E_{dep}$ as shown in figure 36. Since the energy at 1 MeV is of the interest, the corresponding histogram is plotted and fitted to the Gaussian. The sigma from the Gaussian fit is the resolution, in this case it is 1.8% at 1 MeV.

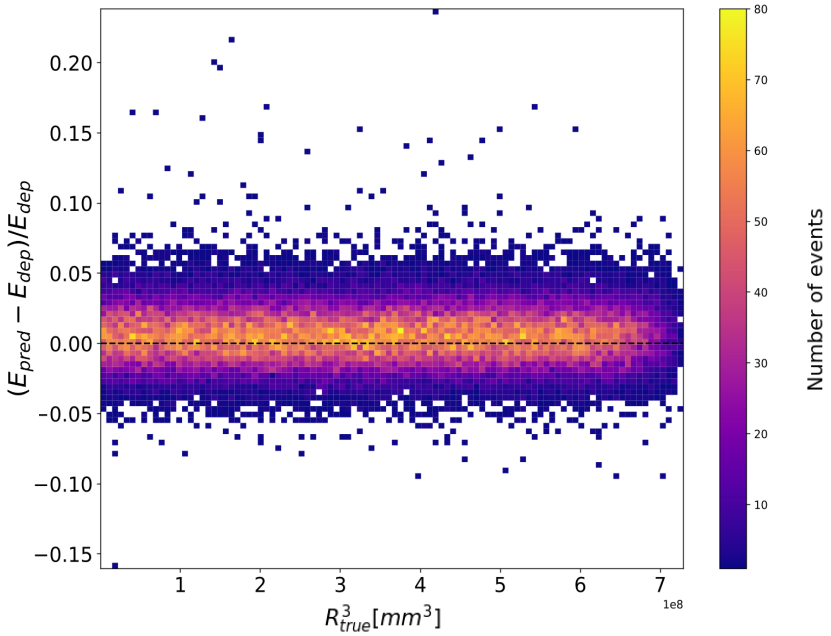

Figure 37: Heatmap of $(\mathrm{E_{pred}} - \mathrm{E_{dep}})/\mathrm{E_{dep}}$ at 1 MeV across detector volume. The cental yellow band indicates events whose predicted values closely match the true values. A slight positive bias is observed

A visualization of how well the model's predicted values match with the true values across the detector volume can be useful to know if there is bias at any regions and the overall variations of energy resolutions. Figure 37 is a 2D heat map that compares $(\mathrm{E_{pred}} - \mathrm{E_{dep}})/\mathrm{E_{dep}}$ in the detector volume $\mathrm{R^3_{true}}$. The color map to the right represents the number of events. The line y=0, serves as a reference point, indicating a slight bias towards the positive values.

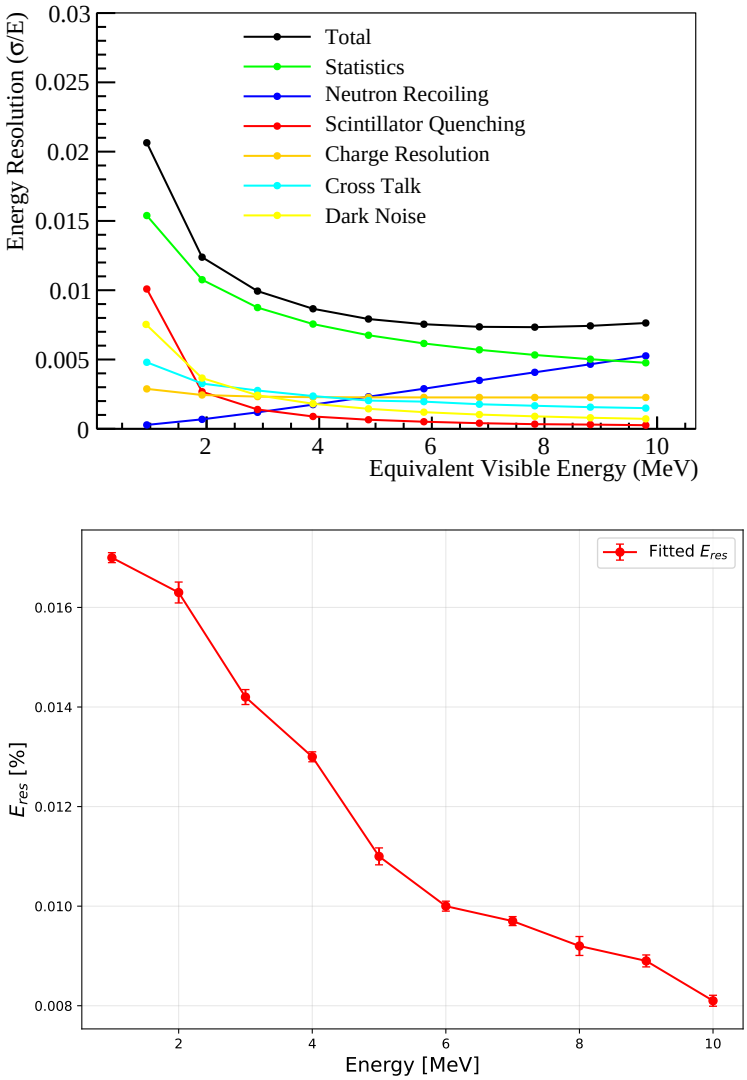

Figure 38: Comparison of the energy resolution of antineutrino events $\mathrm{E_{res}}$ as foreseen in TAO[10] with positron events reonstructed by GCN. While TAO predicts a constant 0.3 % resolution for all energies, GCN shows a gradual improvement from 1.8 % at 1 MeV to 0.8 % at 10 MeV.

The energy resolution across various energies was calculated and compared to the resolution predicted by TAO [10]. Since the reconstruction primarily focused on detector simulations, the charge resolution anticipated in TAO is a suitable benchmark for this comparison. As mentioned before the GCN used only positron events as compared to the neutrino events used by TAO. Figure 38 illustrates a comparison of the energy resolutions foreseen by TAO and the results produced by the GCN. The top plot is the resolution as anticipated in TAO taking into account the LS quenching effect, projected dark noise, cross talk, and charge resolution of the SiPMs across energies 0-10 MeV. Since GCN utilized only the charge , a relevant comparison would be to the charge resolution. It is observed that the charge resolution appears to remain constant at 0.3 % across all energy values, whereas the GCN method shows

a gradual improvement, from 1.8 % at 1 MeV to 0.8 % at 10 MeV. This behavior can arise from the way energy loss fluctuations and signal-to-noise ratio evolve with increasing energy. At higher energies, the relative fluctuations in energy deposition become smaller, as the total energy deposited in the detector increases, leading to a clearer separation between signal and noise. Additionally, the increased number of hits and a stronger signal in the detector allow for more accurate energy measurements, resulting in progressively smaller energy resolution as energy rises.

In conclusion, the optimized models have produced good results for energy and vertex reconstruction. A vertex resolution of about 8 mm could be achieved at 1 MeV. The model could also achieve a good energy resolution. Although a resolution of about 1.8% was achieved at 1 MeV the study utilized involved only positron events. However, to study more realistic scenarios neutrino events should be studied also the electronic simulation must be incorporated. The electronic simulation involves a range of optical processes (Dark Count Rate, waveform distribution and cross talk) which play a critical role in signal detection and can impact the reconstruction.

6 Optimization of Horn Geometry in ESSnuSB+

This chapter introduces ESSnuSB [149] that works towards the primary goals of measuring the leptonic CPV at the second oscillation maximum, precisely determining the CP violating phase δ_{CP} and exploring physics beyond the Standard Model. The ESS [11] is a multidisciplinary research facility under construction in Lund, Sweden, designed to be the world's most powerful neutron source using spallation technology. ESSnuSB is a design study program funded by the European Commission from 2018 to study the feasibility of using ESS as an intense neutrino beam source for ESSnuSB and ESSnuSB+ [150]. While the former aims to study CP violation in the leptonic sector with precision, the latter complements the former's motive by enabling precise measurements of neutrino interaction cross sections below 600 MeV, where no previous data is available [151].

This thesis confines its focus to ESSnuSB+ with a particular emphasis on efficient pion extraction by optimizing the horn (magnetic focusing element) geometry. Pions are produced when the high energy proton beam from the ESS hits the titanium target, resulting in a secondary hadron beam. The focusing of charged pions is done by the magnetic horns which is critical for generating intense neutrino beams, which in turn is essential for measuring the CP violation in the leptonic sector. The horn configuration and its electromagnetic fields play an important role in focusing pions. In this study, the horn is simulated using FLUKA [12] and its configuration is optimized utilizing genetic algorithms (explained in section 4.2). The parameters (dimensions) of the horn are fine tuned over several runs to produce the best parameter set that yields the highest number offocused pions.

6.1 Physics Motivation

In the standard three-flavor oscillation scenario, substantial progress have been made in measuring the key parameters that govern neutrino behavior: the three mixing angles ($\theta_{12}, \theta_{13}, \theta_{23}$), and two mass squared differences ($\Delta \mathrm{m}^2_{21}, \Delta \mathrm{m}^2_{31}$) as shown in table 1. Despite these progresses, there are still some open questions, as explained in section 2.5. One of these questions is the precise value of the CP violating phase δ_{CP}. Measuring this key parameter with precision could help explain the asymmetry between matter and antimatter observed in the universe. The proposed ESSnuSB experiment (baseline of 360 km and a neutrino energy of 2.5 GeV) aims to measure neutrino CP violation at the second oscillation maximum. The sensitivity towards measuring CP-violation at the second oscillation maximum is enhanced by a factor of about 2.5 to 3 compared to the first maximum [152]. Moreover, matter effects

here are substantially smaller [150] thereby enabling improved measurement of δ_{CP}, reduction of systematic errors and high precision. This section explains in detail, the physics goals of ESSnuSB and its expected performance. Additionally, this section introduces to ESSnuSB+, an extension of the original project and it's corresponding goals.

In context of long baseline experiments, the oscillation probability (in vacuum) of ν_μ to ν_{e} contains three terms as presented in equation (6.1): the first term describes atmospheric neutrinos, the second describes solar neutrino contributions and the third term includes CP violation effects through the parameter $\tilde{\mathrm{J}}$, related to the Jarlskog invariant [153] that provides a measure of CP violation.

$$\begin{aligned} P(\nu_\mu \to \nu_e) = & \sin^2\theta_{23}\sin^2 2\theta_{13}\sin^2\left(\frac{\Delta \mathrm{m}_{31}\mathrm{L}}{2}\right) \\ & + \cos^2\theta_{23}\sin^2 2\theta_{12}\sin^2\left(\frac{\Delta \mathrm{m}_{21}\mathrm{L}}{2}\right) \\ & + \tilde{\mathrm{J}}\cos\left(\delta_{\mathrm{CP}} - \frac{\Delta \mathrm{m}_{31}\mathrm{L}}{2}\right)\sin\left(\frac{\Delta \mathrm{m}_{21}\mathrm{L}}{2}\right)\sin\left(\frac{\Delta \mathrm{m}_{31}\mathrm{L}}{2}\right) \end{aligned} \tag{6.1}$$

where, θ_{13}, θ_{23}, and θ_{12} are the mixing angles of the PMNS matrix, and $\Delta_{\mathrm{ij}} \equiv \frac{\Delta \mathrm{m}^2_{\mathrm{ij}}}{2\mathrm{E}_\nu}$,$\mathrm{E}_\nu$ is the the neutrino energy and L is the baseline, $\Delta \mathrm{m}^2_{\mathrm{ij}}$ are the mass squared differences between neutrino mass eigenstates, $\tilde{\mathrm{J}} \equiv \sin\theta_{13}\cos^2\theta_{13}\sin\theta_{12}\theta_{12}\cos\sin\theta_{23}\cos\theta_{23}\sin\delta_{\mathrm{CP}}$ and δ_{CP} is the CP-violating phase. Although all mixing angles contribute to the oscillation probability, θ_{13} plays an important role in evaluating the performance when planning "future" long baseline neutrino experiments. A higher value of θ_{13} amplifies the third term in the above equation that is sensitive to δ_{CP}. When neutrinos propagate in matter, the oscillation probabilities are affected due to forward elastic scattering of neutrinos with matter [36]. Electron neutrinos experience additional potential that affects their propagation in matter from charged current interactions with electrons. These matter effects can mimic the CPV signal (the differences in oscillation probabilities of neutrinos and antineutrinos that indicate a violation in charge-parity symmetry) in long baseline experiments like ESSnuSB as neutrinos travel 360 km through matter. Figure 39 shows the oscillation probabilities for different values of δ_{CP} with solid lines for vacuum and dotted lines for matter as a function of neutrino energy. The first oscillation maximum occurs around 0.65-0.85 MeV while the second oscillation maximum is around 0.25-0.35 MeV. The matter effects has significantly affected the oscillation probability at the first maximum but has a minimal impact at the second maximum. This characteristic of the second maximum could be advantageous for long baseline experiments.

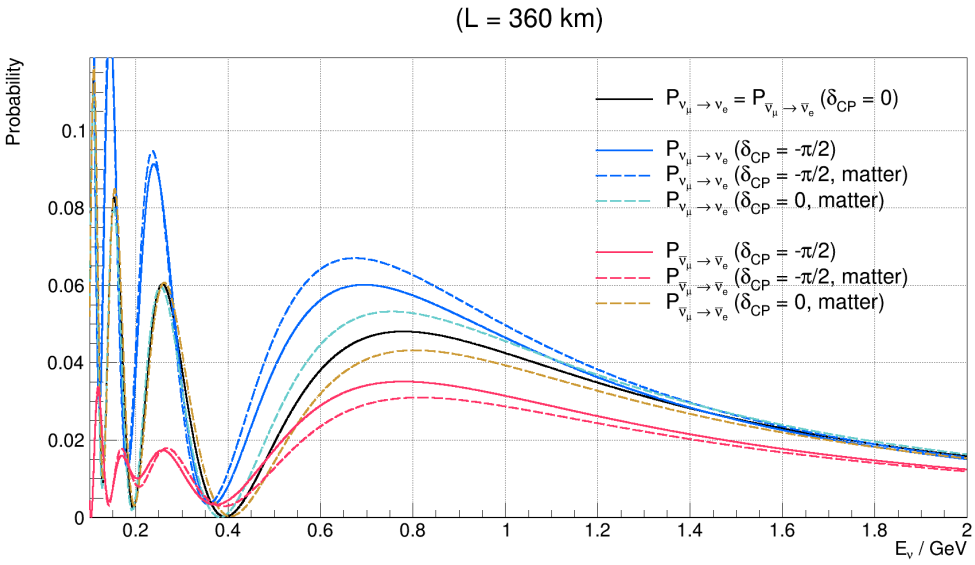

Figure 39: The plot shows the probabilities for $\nu_e \rightarrow \nu_\mu$ and $\nu_e \rightarrow \nu_\tau$ transitions for a fixed distance of 360 km. The solid lines represent the probabilities in vacuum, while the dashed lines show the effect of matter on these probabilities [150].

At the second oscillation maximum, the systematic errors are reduced and this enables increased sensitivity in measuring the δ_{CP}. However, the event statistics at the second oscillation maximum are reduced either due to the long baseline or lower neutrino energies, resulting in lower neutrino interactions. This could be challenging for precise measurements. To overcome these challenges, ESSnuSB is specially designed to leverage the powerful 5 MW ESS linear accelerator that produces proton of 2.5 GeV to generate exceptionally intense neutrino beam to overcome the reduced event rate. This would enable precise measurements that can provide insights into the matter-antimatter asymmetry of the universe.

The expected physics performance of ESSnuSB is based on a total run time of 10 years with 5 years in neutrino mode and 5 years in antineutrino mode, aiming at the second oscillation maxima. In this way the experiment's sensitivity for leptonic CP violation increased and therefore enables the precise measurement of δ_{CP}. The ability to rule out CP symmetry scenarios ($\delta_{CP} = 0, \pi$) is what would allow the potential discovery of CP violation. Different values of different paramters of the systematic error have been studied and it has been noticed that the CPV is most sensitive to uncertainties in the normalization of neutrino flux [150]. This can be seen in figure 40. The plot shows the sensitivity of the experiment to CPV as a function of δ_{CP} for different normalizations. The observed sensitivity, shows symmetrical shape at $\delta_{CP} = 0°, 180°$ with peaks $\delta_{CP} = \pm 90°$, where the CP violation is at maximum. The sensitivity to CPV discovery reaches approximately 13 σ with conservative uncertainties of 5%, up to 17.5 σ for optimistic scenarios of 1% uncertainty and about 7.5σ for worst-case scenario with an uncertainty 25%. This means that even in the worst

case scenario, ESSnuSB can detect CP violation with a significance greater than 5σ for $\delta_{\mathrm{CP}} = \pm 90^{\circ}$. This remarkable sensitivity is due to the experiment's unique design that focuses on measurements at the second oscillation maximum.

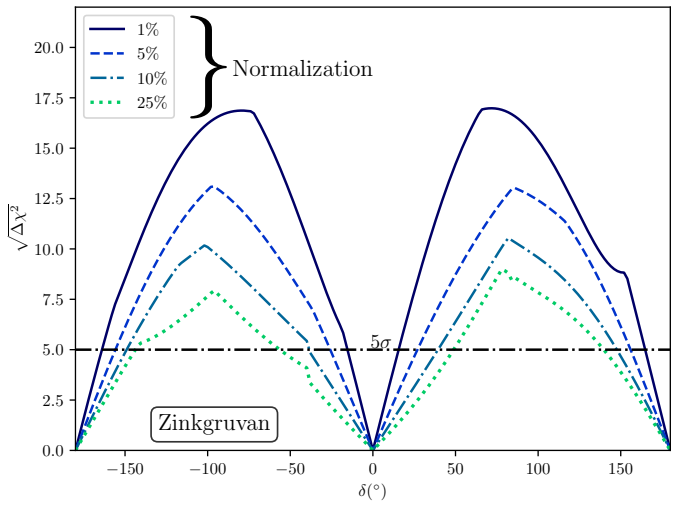

Figure 40: The plot illustrates the potential to discover CPV as a function of the true value of the δ_{CP} . This analysis assumes a baseline length of 360 km (Zinkgruvan mine) and a total run time of 10 years, with 5 years of neutrino mode and 5 years of antineutrino mode. The different lines represent different levels of uncertainty in the normalization of the neutrino flux [149].

The physics goal of ESSnuSB is not only to measure the CPV in the neutrino sector but also to measure it with precision. As shown in the figure 41 the sensitivity of ESSnuSB to the the CP violating phase δ_{CP} value varies with its true values. With 1 % normalization uncertainty the precision would be at its best and at 25% uncertainty the errors would be significantly large. At 5% uncertainty, (which is considered as a conservative scenario) one observe for true values of δ_{CP} around 0° or 180°, a measurement error of approximately 5°, indicating good precision, for $\delta_{\mathrm{CP}} = 90^{\circ}$ the error increases to approximately 7°. The better precision (5°) for δ_{CP} around 0° or 180° is due to the steeper slope of the oscillation probability curve in these regions, enabling more sensitive measurements. The increased error (7°) at $\delta_{\mathrm{CP}} = 90^{\circ}$ occurs because the CP-violating effects are maximal at this point, making the oscillation probability less sensitive to small changes in δ_{CP}. Nevertheless, ESSnuSB can measure δ_{CP} with an error not exceeding 8° making it the most promising long baseline neutrino experiment proposed to date surpassing other experiments like DUNE [154] and Hyper-K [155] which are expected to have a precision of about 20°.

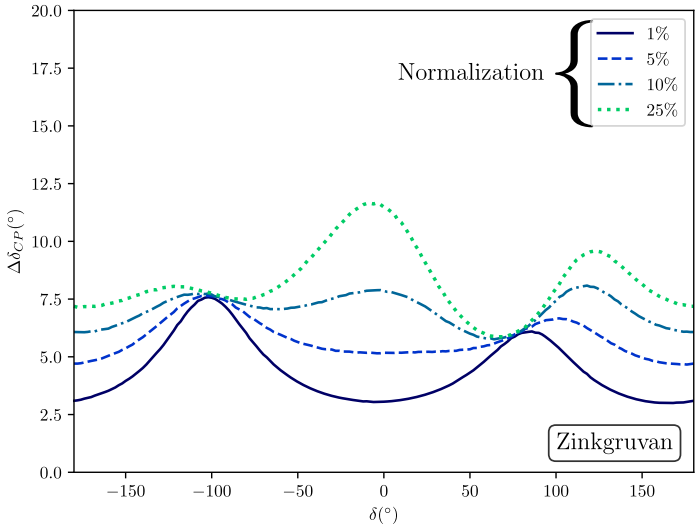

Figure 41: The plot explains the precision of ESSnuSB's measurement on δ_{CP} by comparing its sensitivity to δ_{CP} as a function of its true value. The plot shows $\chi^2 = 1$ contour for different normalization percentages.[149].

Accurate measurements of the neutrino-nucleus interaction cross section are important as it is a major factor contributing to systematic uncertainties in ESSnuSB. These are essential in understanding how neutrinos interact with nuclei at the low energy regime of ESSnuSB, i.e. $<$ 600 MeV. Several experiments like T2K, NOvA, MicroBooNE have measured neutrino cross sections at low energies [156]. However, the available data in this energy regime are limited and often have significant uncertainties. To address these limitations, the ESSnuSB+ project is proposed which would have additional detectors and facilities to measure cross section across wider ranges. ESSnuSB+ comes with two facilities: Low Energy Neutrinos from STORed Muons (LEnuSTORM) and Low Energy Monitored Neutrino Beam (LEMNB) to enhance neutrino interaction cross section measurement in the region 0.2 to 0.6 GeV. The LEnuSTORM facility is aimed at generating beam of muon neutrinos and electron neutrinos using racetrack storage ring to study neutrino nucleus cross sections with high precision. The LEMNB aims to produce a monitored neutrino beam that would aid in improving the cross section measurements of muon and electron neutrinos by precisely tagging the corresponding leptons. The following section will explain in detail on the experimental configurations of these facilities.

6.2 Experimental Layout

The ESS is the world's most powerful linear accelerator facility that is under construction in Lund, Sweden. It will use spallation technology to generate intense neutron beams by accelerating protons to 2.0 GeV and colliding them against a tungsten target with each pulse lasting 2.86 ms with a repetition rate of 14 Hz. The high energy neutrons that are produced are slowed and cooled and are directed to various experimental stations for cutting-edge research. The layout of the ESS facility as shown in

figure 42 houses the accelerator (Linac), the target monolith (where protons collide on the tungsten wheel to produce spallation neutrons), the experimental hall (that hosts sophisticated neutron instruments tailored for various scientific investigations) and the utility building (that provides the services to support the entire operation of the facility). The ESS's powerful linear accelerator can additionally be an ideal ground to produce intense neutrino beam for the ESSnuSB experiment. In order to achieve this dual purpose several key upgrades are required in the existing facility [157].

The planned upgrades in the project has its focus on four main regions as highlighted in figure 43. The first upgrade is in the accelerator where H^- ions are introduced to the existing proton pulse. The original proton pulse of 14 Hz remains for the neutron production and on top of it 14 additional H^- pulses are interleaved, resulting in 28 Hz pulse frequency. At the injection point to the accumulator ring H^- ions are stripped

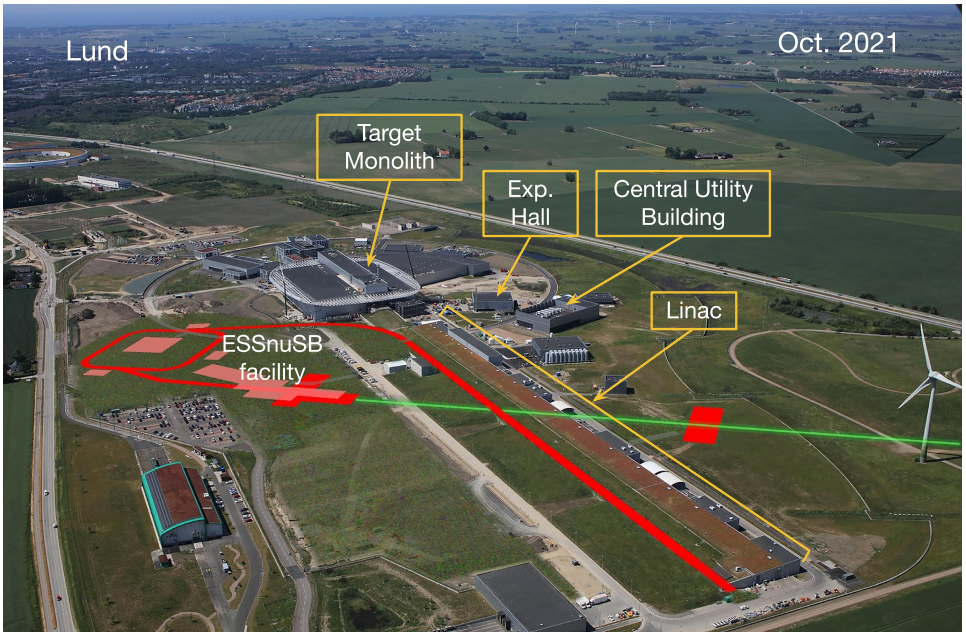

Figure 42: Layout of the ESS facility accommodating the ESSnuSB. The yellow labels represent the component of the ESS facility and to the left is the proposed ESSnuSB facility with the accumulator ring [158].

of their electrons to produce protons that are trapped in the magnetic field, resulting in high intensity beam. The second upgrade is to build the accumulator ring (circumference = 384 m). The main function of the ring it compress the 2.86 ms long pulse to appoximately 1.2 μs. This is done with the motive to minimize the atmospheric neutrino background in detector and help in improving the signal to noise ratio. The compressed signal is then directed to the neutrino target station, which is the third upgrade. A switchyard will be developed to distribute compressed pulses from the accumulator ring to the station. The station will have four identical horn systems each designed to receive 1.25 MW from the 5 MW beam. The target will be cylindrical (length = 78 cm, diameter = 3 cm) with packed titanium spheres (diameter

= 3 m) cooled by pressurized helium. This configuration will allow efficient handling the intense beam power. As the proton beam strikes the target, the horn focuses the secondary particles (pions) into the decay tunnel. In the tunnel the pions decay producing muons and their corresponding (anti)neutrinos. This creates the intense beam required for the experiment. As a final upgrade, a near detector will be built to monitor the neutrino beam and to measure its flux and energy spectra. As the focus of the study is ESSnuSB+, a detailed explanation of ESSnuSB detectors is beyond the scope of this thesis but for more informantion, please refer to [149].

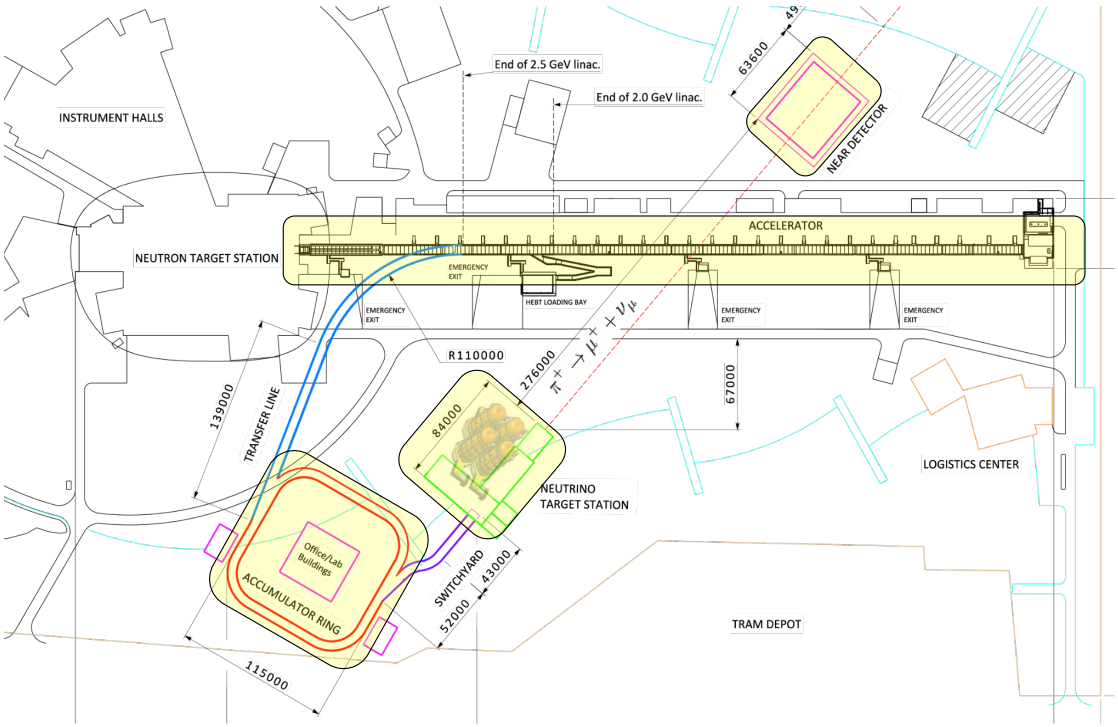

Figure 43: The figure illustrates the modifications in the ESS layout to cater to ESSnuSB. The parts highlighted with yellow are the new requirements. This include: upgrading the linac, building an accumulator ring, neutrino target station and a near detctor [149].

ESSnuSB+ is an extension of the original ESSnuSB project, designed to enable high precision measurements for the low energy neutrino interaction cross section. The upgrade proposes to build an R&D target station operating at 1.25 MW with only one horn/target system and facilities for low energy (0.2-0.6 MeV) measurements: LEnuSTORM and LEMNB. As illustrated in figure 44 the experiment begins with a proton beam from the upgraded ESS-linac striking the Titanium target to produce pion. Theses pions are focused by a magnetic horn that either selects positive or negative pions based on its polarity. The desired pions are focused and passed into the pion tunnel while the pions with the opposite sign (wrong sign) get deflected away from the beam axis and out of the decay tunnel. This helps in maintaining beam purity and reduces undesirable neutrino flavor contamination. Additionally, the pions with

the correct charge but the wrong energy/momentum (E/P) are also eliminated by a dipole. Meanwhile, the quadrupole magnets focus the pions with the right energy and send them to the LEnuSTORM racing track. This refinement of the pion beam is very crucial for ESSnuSB+ to achieve its physics goals. The LEnuSTORM (muon storage ring) is a racetrack shaped ring that allows the pions to decay into muons as they circulate. The muons further decay to (positrons)electrons and muon (anti)neutrino and electron (anti)neutrino depending upon the charge of the muons.

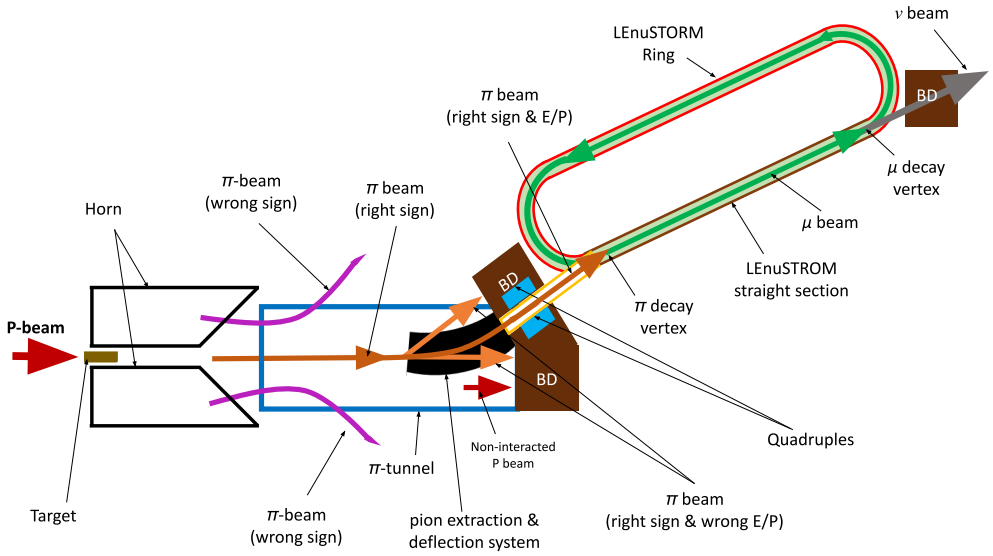

Figure 44: Schematic Overview of the ESSnuSB+ experiment. The diagram illustrates the flow of the experiment, from initial proton beam to the final neutrino production in the LEnuSTORM muon storage ring and various stages in between that involves refining the beam [159].

Parallel to the LEnuSTORM is the LEMNB facility that aims to measure neutrino flux by tracking charged leptons produced alongside neutrinos by using an instrumented decay tunnel. The iron scintillator calorimeters in the tunnel help reconstruct the energy and direction of these decay products, allowing a precise determination of the corresponding neutrino flux.

6.3 Motivation to Optimize Horn Geometry

The magnetic horn is a very vital part of the ESSnuSB+ experiment as it aims to efficiently to focus the produced secondary pion beam. The horn is primarily composed of aluminum (95.5%) with small additions of silicon, magnesium, chromium, manganese, iron, zinc, and copper. The current horn design has a baseline length of about 2.5 m and a radius of about 60 cm and will operate at a high current of about 350 kA to generate strong magnetic fields of about 1.97 T. Figure 45 shows a 3D time-dependent simulation of the trajectories of positive pions propagated through the magnetic field of the horn that is resulted from applying 350 kA to the horn

conductors. The current flows radially inward through the horn's conductor, creating a toroidal magnetic field that focuses charged pions. Pions with low energy or larger scattering angles are dispersed (as they are not affected by the magnetic field), whereas the higher energy ones are concentrated into a beam. This selective focusing effect of the horn is vital for shaping the pion beam. An optimized horn geometry and magnetic field configuration can aid in maximizing the pion focused in the desired direction. To optimize the horn geometry, a wide parameter range must be explored. The genetic algorithm can be used to investigate the design space of the horn. The goal is to identify a design that maximizes physics performance while satisfying practical constraints. The following section describes the implementation of the genetic algorithm to optimize the horn geometry to maximize the pion flux.

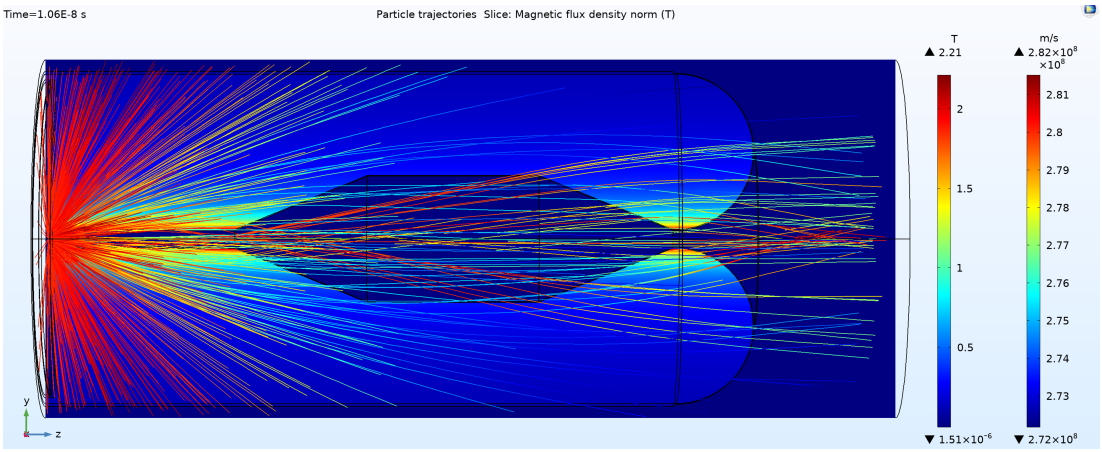

Figure 45: The COMSOL simulation visualizes the pion profile at the interaction point for a particular horn configuration. The color bars represent the magnetic field strength in Tesla (T) and the velocity of pions in meters per second (m/s). The increased charge concentration at the inner horn edges results in a stronger magnetic field in these regions. The field deflects lower-velocity pions while focusing higher-velocity pions towards the target.

6.4 Implementation of GA

As explained in chapter 4 genetic algorithms are optimization methods inspired by biological evolution and are well suited to handle multiple optimization parameters with complex correlations. The horn geometry involves multiple interdependent parameters like lengths, radii and currents that can affect the pion flux in complex nonlinear ways. GAs are efficient in navigating complex design spaces like that of the horn geometry without getting stuck in a local optima. It evaluates the solution candidate (individual) that has unique parameter values (genes) based on its fitness. The process involves generating a random initial population , evaluating fitness, and applying section, crossover and mutations to produce several generations. The algorithm converges when the maximum fitness ceases to improve.

6.4.1 Work Flow

For this study, a combination of FLUktuierende KAskade (FLUKA) and Python was used to generate the pion flux for different horn configurations and to optimize its shape respectively. For this study, the Python toolkit DEAP library [160] is utilized to create the framework for genetic algorithm.

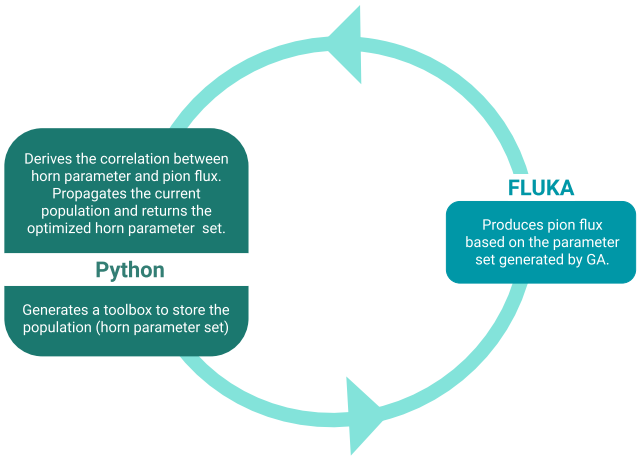

Figure 46: Workflow: The initial horn configuration is generated by FLUKA simulations. The simulated pion flux from FLUKA is analyzed in Python using the genetic algorithm to identify potential improvements in the configuration. The optimized configuration is then fed back into FLUKA and the process iterates until convergence is reached.

The workflow as illustrated in figure 46 is an iterative optimization process. As shown, a toolbox is created in Python to manage the population of individuals (horn parameter set). The initial horn configuration comes from the FLUKA simulations that produce pion profile (intensity of flux and its spatial distribution) corresponding to the initial configuration. The produced profile is sent to Python where each individual is analyzed. The individual having relatively higher pion fluxes (fitness) is selected to propagate the individuals of the next generation. For propagation, crossover and mutation operators that are registered in the toolbox are used. The newly formed individuals are passed onto FLUKA to study their pion fluxes, and this iterative process continues when significant improvement is seen over several generations. The final configuration that yields the maximum flux is identified as optimal.

6.4.2 Definition of Individuals

The horn design has complex dimensions. These dimensions (parameters) play a crucial role in extracting and focusing the dense pion beam for neutrino production. As shown in figure 47 the parameters used for this study can be categorized into length parameters $(\mathrm{L}_1, \mathrm{L}_2, \mathrm{L}_3, \mathrm{L}_4, \mathrm{L}_5)$, height parameters $(\mathrm{h}_0, \mathrm{h}_1)$, radius parameter (R_0),

target parameter (z_{off}), and current parameter (I_0). The length parameters design the longitudinal section of the horn that is most critical in optimizing the collection and focusing of the pion beam. The height parameters design the vertical dimensions along the geometry and may affect the electromagnetic properties that are important for pion focusing. The radius parameter impacts the focusing strength, which determines how well pions are directed through the system. The target position along the z-axis is important for the optimization of proton interactions with the target, so it affects the pion production rates. The current parameter is the peak current flowing through the horn to generate magnetic fields that focus pions. The details of all the parameters with their baseline value and their range are summarized in table table 4. Each parameter is a gene, and together they contribute an individual. For this study, each generation was populated with 10 individuals and 50 such generations were studied. The first generation was created by picking a random value for each parameter (gene) within the intervals shown in table 4.

Table 4: The parameter definition and range for the ESSnuSB+ horn design

Parameter (Unit) Description	Baseline Value	Range
L_1 (cm): Length of the initial section	63.98	[31.99, 159.95]
L_2 (cm): Length of the upstream section	46.8	[23.4, 117]
L_3 (cm): Length of the main focusing section	60.3	[30.15, 150.75]
L_4 (cm): Length of the downstream section	47.5	[23.75, 118.75]
L_5 (cm): Length of the final section	1.08	1.08 (fixed)
h_0 (cm): Height at the narrowest point	3.3	3.3 (fixed)
h_1 (cm): Height at the widest point	22.4	[11.2, 56]
R_0 (cm): Initial radius at the downstream end	27.2	[13.6, 68]
z_{off}(cm): Position of the target along the z-axis	6.8	[3.4, 17]
I_0 (kA): Peak current flowing through the horn	350	[175, 875]

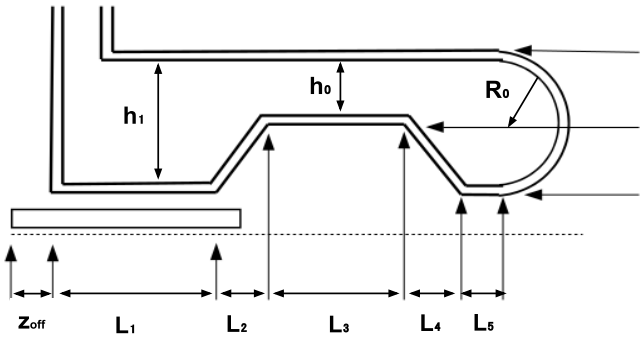

Figure 47: Transverse view of the horn with the key geometric parameters that influence its performance.

6.4.3 Evaluation & Propagation of Individuals

The intensity of the pion flux emerging from the horn is an important factor to decide on the fitness score of each individual. For this study we formulate the individual fitness score as the detection efficiency of each configuration

$$\epsilon = \frac{N_{\text{det}}}{N_{\text{tot}}}, \tag{6.2}$$

where $\{N_{det}$ is the pions detected in the specific region of interest, for this study a distance, z = 10 m from the horn with a cross section of x=y=2 m and $\mathrm{N_{tot}}$ is the total pion flux generated from the target. The choice of 10 m is to study horn's focusing ability at reasonable distance. By evaluating the beam profile at this distance one can determine the optimal location for additional beam elements such as dipole magnets to deflect the pion beam into LEnuSTORM facility. The pion flux density within a 10 m region and the total flux density are illustrated in Figure 48 for a horn with baseline parameters in table 4. The ratio of these distributions represents the detection efficiency of the configuration, which in this case is 0.537, calculated as the ratio of pions within 10 meters (333,076) to the total number of pions (619,988).

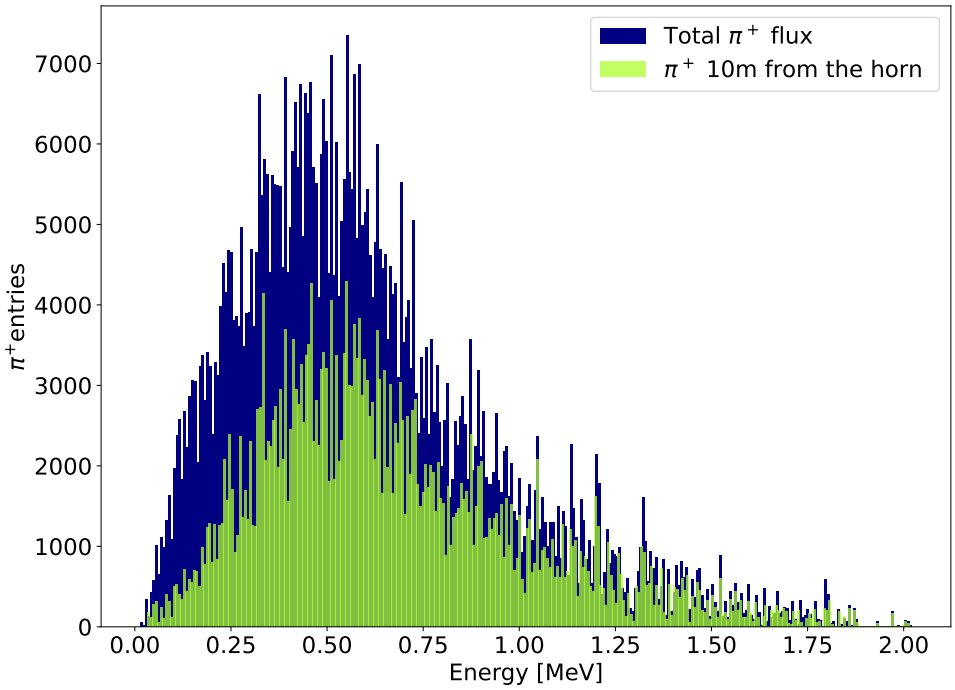

Figure 48: Total pion flux as a function of energy measured 10 meters from the horn, illustrating the distribution and intensity of pions produced across various energy levels.

Following the fitness evaluation is the selection of the individual to propagate the next generation. This is done by choosing individuals with higher fitness score in the current generation. The horn configurations that have higher detection efficiency are chosen to propagate individuals for the next generation. The selected individuals were propagated using crossover and mutation methods as explained in chapter 4. To illustrate the evaluation and propagation process, consider the example in table 5. Two parents are selected based on their fitness scores and undergo crossover and mutation to produce a offspring. In crossover, the first three genes $(\mathrm{L}_1, \mathrm{L}_2, \mathrm{L}_3)$ are exchanged between parents to create offspring 1. In mutation, two genes $(\mathrm{h}_1, \mathrm{z_off})$ of parent 1 are randomly replaced to generate offspring 2. This is just an example, crossover and mutation can occur randomly at any gene location. The resulting offspring contribute to a new generation and would continue to propagate until there is no any significant improvement in the detection efficiencies of individuals over a few generations.

Table 5: Crossover and Mutation of horn configurations

Individual	L_1	L_2	L_3	L_4	L_5	R_0	h_0	h_1	z_{off}	Fitness
Parent 1	75.49	107.63	126.63	115.89	1.08	27.2	3.3	51.07	16.86	0.6011
Parent 2	80.22	98.45	130.01	110.50	1.08	30.5	3.3	48.92	15.73	0.5895
Offspring 1 (Crossover)	**75.49**	**107.63**	**126.63**	110.50	1.15	30.5	3.3	48.92	15.73	0.6053
Offspring 2 (Mutation)	75.49	107.63	126.63	115.89	1.08	27.2	3.3	**57.03**	**17.01**	0.6025

6.4.4 Optimization results

To optimize the horn geometry, 50 generations were studied with each generation having 10 individuals. Three independent runs were carried out to see how the fitness improved with generations and the results are presented below. For a single run, the pion profile is examined before and after optimization. This comparison improves the understanding of the process. Figure 49 conveys the impact o the horn optimization on the spatial distribution of pions. Both plots are fitted to a 2D Gaussian with mean centered around (100 cm, 100 cm). The color bars represent the distance from the mean. The distribution before optimization has a wider spread with the sigma ring (contour in the 2D Gaussian distribution that shows the spread from mean) having a radius of about 48 cm (x=47.98 cm, y=48.03 cm) containing about 9870 pions within the ring. After optimization, the sigma ring shrinks significantly to a radius of about 20 cm (x=19.98 cm, y=20.05 cm) containing 11,806 pions within. The optimization resulted in a more concentrated Gaussian peak showing the improved focusing of the pion beam resulting an increase of about 20 % in pion concentration. Possible tuning of the magnetic field profile (from the current running) with proper adjustments of the horn dimensions results in an effective shaping of pion trajectories, increasing the particle flux and reducing dispersion.

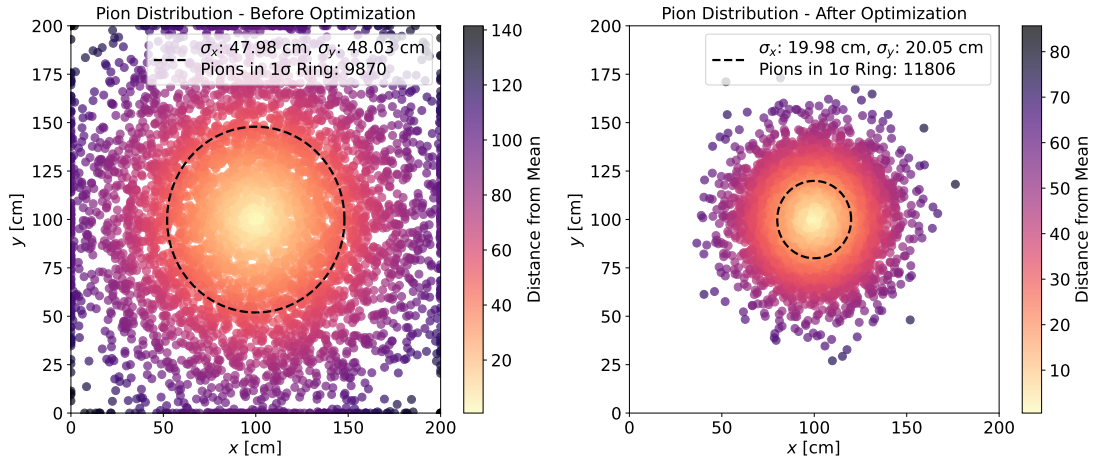

Figure 49: Comparative analysis of the cross sectional pion distribution that falls at distance of z=10 m from the horn before (left) and after (right) optimization of the horn configuration. The optimization process has effectively improved the spatial confinement of the pions, leading to a more concentrated and focused distribution.

Also, a comparison of the optimized parameter to the baseline parameter is listed in table 6. The comparison of optimized values presented in the table indicate strategic adjustments made to various parameters that directly influence pion flux production. The optimized length L_1 is shorter, which may improve pion convergence toward the detector and reduce beam divergence. An increase in L_2 , L_3 and decrease in L_4 allows for better focusing of the pion beam, potentially capturing more pions. R_0 is significantly larger, increasing the collection area for pions and improving overall flux. A decrease in h_1 optimizes pion trajectories by reducing losses due to misalignment. The increased z-offset helps in aligning the target along the z-axis to ensure more pions reach the horn. Also, the increased current I_0 enhances magnetic field strength, resulting in a denser beam thereby improving the overall flux. A comparison between the baseline values and the optimized values for all the three runs are shown in figure 50. The optimized values are almost similar across all three runs, suggesting a reliable optimization.

Table 6: Comparison of Optimized Parameters run1 with its Baseline Values

Parameter	L_1	L_2	L_3	L_4	L_5	R_0	h_0	h_1	z_{off}	I_0
Optimized Value	47.39	73.02	96.39	42.60	1.08	63.65	3.30	12.54	15.23	473.00
Baseline Value	63.98	46.80	60.30	47.50	1.08	27.20	3.30	22.40	6.80	350.00

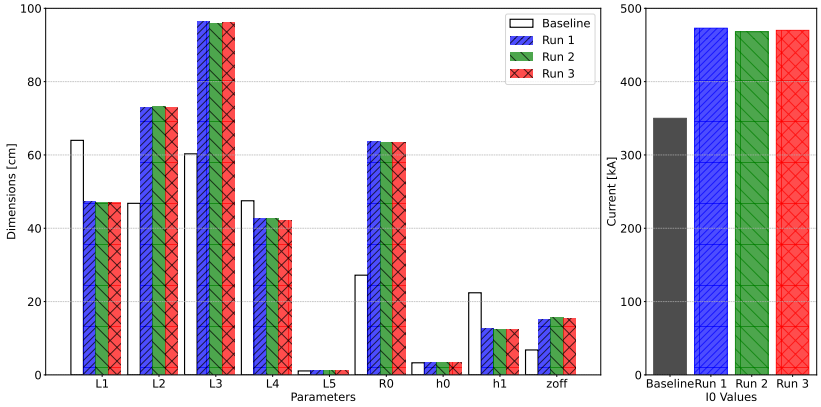

Figure 50: Comparison of optimized values and baseline values for all parameters: length dimensions (left) and current (right) across three runs.

The assessment of the fitness values across generations provides an evaluation of the optimization process. Figure 51 illustrates the change of fitness values over 50 generations or 3 different trials. It can be seen that performance measures improve up to about twenty generations, it is at this turning point where a lot of changes take place during the optimization process. Once 20 generations have lapsed, the measure rests comfortably within the bandwidth of 0.860 and 0.875 with little or no improvement further.

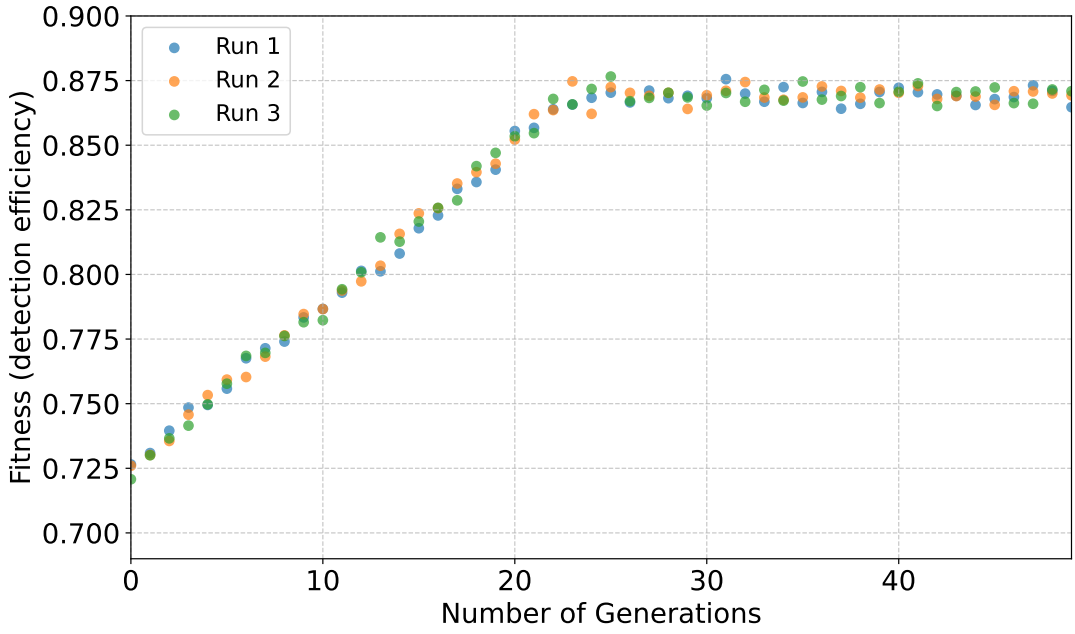

Figure 51: Fitness Progression Across Generations: This plot illustrates the fitness values of each generation's best individual for three distinct runs. Each run exhibits a steep initial rise in fitness, reaching a peak of 0.860 by the twentieth generation, followed by a sustained plateau.

Overall, this analysis highlights how genetic algorithm can be used in optimizing horn geometry, thereby enhancing the pion detection efficiency. Key modifications in the horn parameters collectively resulted in a more concentrated pion beam distribution. The radius of the sigma contour (20 cm) can be important to decide the distance between the dipoles placed after the horn geometry to deflect the pion beam towards the nuSTORM ring. The fitness value, which is a measure of detection efficiency, improved from approximately 0.725 to a plateau of about 0.860 by 20 generations, suggesting an improvement of approximately 20 % in pion detection. The almost constant detection efficiency until the 50 generations indicates that the algorithm has converged to an optimal solution. The optimization of horn geometry in ESSnuSB+ resulted in a focused pion beam which can significantly enhance neutrino flux, allowing for more precise measurements of neutrino cross-sections.

7 Results and Conclusions

The JUNO experiment is designed to resolve the neutrino mass ordering through high precision measurements of reactor antineutrino. Nevertheless, to accomplish its science objectives, JUNO depends on TAO for precise measurements of the reactor antineutrino spectrum. In TAO, the reactor electron antineutrinos undergo the IBD as they interact with the LS in TAO and produce prompt positron and delayed neutrons. The focus of the thesis was to reconstruct the vertex and energy of positron events using Graph Convolutional Networks. Vertex reconstruction was done with an aim to accurately determine the interaction point's spatial coordinates using the first hit time and hit counts from Silicon Photomultipliers (SiPMs). The quality of this reconstruction is evaluated by the vertex resolution, which is how well the true interaction points match the predicted positions. Accurate vertex reconstruction is important for the application of fiducial volume cuts, excluding background events at the detector edges and maximizing the usable volume. This is very important for TAO, being a reference detector for JUNO, in producing a high-quality, model-independent reactor antineutrino spectrum.

The reconstruction uses GCNs in a PyTorch environment. The detector is modeled as a spherical graph with 4024 nodes, each representing a SiPM, and each node has two features: first hit time and hit counts. The graph is subjected to convolution and pooling to predict the vertices. The model was trained using 3.5 million events and validated using 1.5 million events. For the vertex reconstruction the model stabilized after 39 epochs, demonstrating good generalization to both training and validation data. Evaluating the model on a 1 MeV subset showed strong linear correlation between predicted and true vertex positions, with a vertex resolution of approximately 8 mm at 1 MeV and improving for higher energies. The radial distance resolution was 9.5 mm, which is crucial for applying fiducial volume cuts and improving event selection near the detector edges. Compared to the center of chagre reconstruction method, the GCN-based method achieved a significantly better vertex resolution of 7 mm vs 44 mm. However, the center of charge method was used on neutrino events whereas GCN used only positron events, so the resolution could differ if neutrino events were included in future comparisons. The energy reconstruction was performed with an objective of precise prediction of the energy at the point of interaction. The energy resolution was calculated with the same model and results are compared with those predicted by TAO. At 1 MeV, the GCN method had an energy resolution of 1.8 %, which increases to 0.8 % at 10 MeV. This is because at higher energies the relative fluctuations in energy deposition are smaller. Also, the increased signal-to-noise ratio enables more precise energy measurements. However, the predicted energy resolution as foreseen in TAO seemed to be have a constant resolution

of 0.3 % across all energy values.

The event reconstruction efforts using GCN have shown promising results with vertex resolution of 8 mm and energy resolution of about 1.8 % at 1 MeV for positron events. However, there are several important steps to enhance the realism of the analysis. Future steps will include neutrino events in the reconstruction chain. This will require the use of classification algorithms to deal with neutrino interaction signatures, like charged and neutral current processes, that are quite different from simple positron events. The improved particle identification coupled with energy reconstruction techniques will be essential in providing precision analyses for neutrino-induced signals. Also, updating the vertex reconstruction algorithms for neutrino events will give a better understanding of the spatial resolution of the detector. Besides that, including the electronic simulation in the TAO analysis will enable considerable improvement in realism with respect to the detector performance evaluation. This important step will introduce the following key electronic effects inherent to SiPM and other electronic components: Dark Count Rates (DCR), cross-talk, and waveform distributions. Simulation of these electronic effects will provide a truer representation of the detector response and allow for refined calibration of the reconstruction algorithms and a more realistic assessment of TAO's energy and spatial resolution capabilities. Further studies may include improvements to the reconstruction algorithms for different event topologies, and tuning model hyperparameters using Bayesian optimization to achieve the best overall performance in event reconstruction. These steps will allow TAO to exploit its full detection capabilities and hence make more significant contribution to facilitate precise reactor antineutrino spectrum measurements.

The thesis also focuses on the ESSnuSB+ experiment, which aims to precisely measure neutrino interaction cross sections below 600 MeV, supporting the broader ESSnuSB project's goal of investigating leptonic CPV at the second oscillation maximum. Using the ESS in Lund, Sweden, a high-energy proton beam strikes a titanium target, generating a secondary pion beam. These pions are focused by magnetic horns so as to direct them effectively toward the neutrino facility.

The magnetic horn within the ESSnuSB+ experiment plays a vital role in focusing the secondary pion beam used in neutrino production. In order to optimize its design, a Genetic Algorithm (GA) was utilized and key parameters, such as horn lengths, heights, radius, and current were optimized to maximize pion flux. The GA iteratively refined the horn's geometry using Fluka simulations, to generate the pion flux profiles, and Python's DEAP library to facilitate the optimization process. This resulted in a 20 %, increase in the pion concentration, with the optimized horn producing a more focused beam. The most important variations included a reduction in section lengths, an increase in the horn radius, and a higher current to improve beam focusing. The fitness score, as a measure of detection efficiency, increased from 0.725 to 0.860, indicating a significant optimization. This improved focusing will enhance neutrino

flux and precision in neutrino cross-section measurements, thus enhancing the overall physics performance of the ESSnuSB+ experiment.

Future studies include further pursuit in the direction of alternative geometries for horns, like parabolic or elliptical shapes, which might ensure even higher focusing efficiency. Besides, multi-horn systems or variation in the relative spacing between horns can be explored for optimizations in pion capture and transport. Beyond the horn itself, consideration might be given to a design of the dipole magnets required for the steering the secondary pion beam with minimum divergence and for maximum alignment to the neutrino facility. Such studies may be done in state-of-the-art simulation tools, like Fluka or GEANT4, in order to model beam dynamics and study the impact of different geometries on neutrino flux. Continued advances, such as these, in the design of horns and beamlines will be crucial for ESSnuSB+ to realize maximum physics potential in precision neutrino cross-section measurements.

List of Algorithms

1 Training, Validation, and Testing of a Neural Network 43
2 GA Workflow 50

List of Figures

Figure 1: A schematic view of the Standard model that illustrates elementary particles and their interactions [17]. 4
Figure 2: The pp chain is illustrated, outlining the primary branches and their respective distribution ratios. Neutrinos released in this sequence of reactions are identified as pp (stemming from the reaction at the upper left), Be-7 (in the pp II branch), B-8 (pp III), pep (upper right), and hep (center right). [41] 12
Figure 3: The light blue band represents the electron neutrino survival probability, as predicted by MSW-LMA effect [48]. The flux is based on Standard solar model with black point indicating the Borexino neutrino data and the red point ins the combined SNO+Super-Kamiokande data. 13
Figure 4: Illustration of cosmic rays producing atmospheric neutrinos after colliding with an air nucleus in the atmosphere [52]. 14
Figure 5: Detection of the coincidence signal of prompt positron and delayed neutron signal confirms a neutrino candidate. The bottom part shows the reactor neutrino flux for different isotopes. The inverse beta decay reaction's cross-section is the blue curve and the outcome (interaction spectrum) detected by the detectors is indicated by the red curve [60]. 15
Figure 6: This illustration shows the neutrino mass ordering and the unknown absolute mass scale. On the left, it displays the squared neutrino masses for the Normal Mass Ordering , while on the right, it shows them for the Inverted Mass Ordering. Violet, red, and yellow mark the admixtures of ν_e, ν_μ, and ν_τ to the mass states, respectively [79]. 18
Figure 7: Schematic representation of the JUNO detector. The central acrylic sphere contains 20 kt of liquid scintillator, surrounded by PMTs. This is supported by a stainless steel structure, immersed in water tank with veto PMTs. A Top Tracker and calibration house complete the setup that is designed for precise neutrino measurements [92]. . 26
Figure 8: The expected antineutrino energy spectrum for NO, IO, and no oscillation for 6 years of data taking. The curves that correspond to oscillation are obtained by applying survival probability of electron antineutrinos on their original energy spectrum. [93] 27
Figure 9: Schematic view of the TAO detector, indicating the liquid scintillator target located in the middle of the spherical copper shell and the stainless steel tank, with the external water tank surrounding it. It consists of a top veto tracker for cosmic ray muon detection an ACU for precise calibration. 28

Figure 10: The figure compares the observed reactor antineutrino spectrum to Huber Mueller model predictions. The Left panel shows the predicted and measured prompt energy spectra. On the right panel the extracted spectra of $^{235}\mathrm{U}$ and $^{239}\mathrm{Pu}$ is compared to model predictions (using best-fit normalization factors (0.92 and 0.99)) [98]. . . 33
Figure 11: Calculated antineutrino energy spectra from many fission products in a commercial reactor [100]. 34
Figure 12: The statistical uncertainty of TAO & JUNO with three & six year's of data taking respectively [10]. 35
Figure 13: The plot shows mass ordering sensitivity for different reference spectra (represented by different markers) for JUNO. The χ^2 value quantifies the sensitivity where higher values indicate better discrimination between normal and inverted orderings [7]. 36
Figure 14: A representation of a neuron that sums up weighted inputs x_i, applies an activation function to modulate the weighted sum to yield the output of the neuron. [108]. 38
Figure 15: The plot shows the the learning progression of the model across 80 epochs. The first ten epochs indicates a clear case of underfitting. From epochs 10 to 60 the training and validation loss tend to converge, indicating learning. After 60 epochs the increasing validations loss signals the onset of overfitting. 42
Figure 16: A representation of graph with it's nodes and edges. Each node represents a variable or operations and the edges represent the connection between the nodes [116]. 44
Figure 17: The graph is partitioned using K-Means algorithm and is subjected to max-aggregation. Nodes that belong to the same partition have similar color and their size is proportional to the signal strength [125]. 46
Figure 18: The residual unit is composed of the residual function $F(x)$ and the identity operator. The output at every layer adds up the input x passed through the identity operator [128]. 47
Figure 19: Fully connected dense network where each each neuron in a particular layer is connected to every other neurons in the next layer. This architecture was generated using [129] 47
Figure 20: Components of a genetic population. Each individual is identified by their chromosome which is a unique combination of their genes. 49
Figure 21: Fitness Evaluation and Selection of Individuals. 50
Figure 22: Illustration of one-point, two-point and uniform crossover operators. 51
Figure 23: Illustration of mutation of an individual. A random gene position is selected and altered to produce the offspring. 52

Figure 24: Components of the TAO offline software [10]. The JUNO Offline Software is a data processing environment with components of physics generators, detector simulation, and event reconstruction. The TAO Offline Software that has been tailored specifically for reactor antineutrino detection utilizing similar structures to JUNO Offline Software but focusing on the unique requirements of the TAO experiment. The SNiPER Framework serves as the backbone for the software of both JUNO and TAO providing an extensible architecture for efficient event data management and the External Libraries that consist of mainly Geant4 for simulating interactions of particles and ROOT for data handling and visualization. 57
Figure 25: The TAO event display software displaying a gamma event. The visualization effects of the event and detector components can be controlled on the right panel through the functional buttons available [147]. 59
Figure 26: A positron event with deposited energy of 1.512 MeV. Only fired SiPMs are shown. (Left) Distribution of the number of hits with yellow points representing more hits and red points representing fewer hits. (Right) The first hit time (FHT) is represented where the lighter blue represents earlier first hit arrivals. The grey sphere represents the primary vertex. 60
Figure 27: Architecture used for reconstruction. The graph with its features (SiPM data) is fed as input into the NN. The first layer is a single graph convolution layer where the feature dimension is indicated using filters. Following all convolutional layers are residual blocks that vary across the network. After every residual unit is a partition pooling layer that reduces the number of nodes. After the fourth convolution the graph is flattened to a fully connected layer with linear activation that outputs the three vertex coordinates x,y,z. . 62
Figure 28: Training (green line) and validation loss (blue line) over number of epochs. An initial drop suggests that the learning has began and with increasing epochs the validation loss converges around the training loss. 64
Figure 29: Comparision of the true and predicted values of vertices (x, y, z). The predicted values shows a clear linear trend, suggesting that the model's predictions align closely with actual measurements. 65
Figure 30: Difference between the predicted and true event vertices for each coordinate x (top), y (middle) and z (bottom) at 1 MeV. The distributions are fitted to a gaussian and the sample mean μ and the standard deviation σ are indicated in the graphics. The fitted σ value is the resolution of the vertex. 66
Figure 31: A histogram of the differences between true and reconstructed R at 1 MeV, fitted to a gaussian. The width of the gaussian determines the resolution. 67

Figure 32: Heatmap of $R_{pred} - R_{true}$ versus R^3 for events at 1 MeV. The cental yellow band indicates events whose predicted values closely match the true values. The uniform distribution across the detector volume shows unbiased reconstruction. 68
Figure 33: The plot illustrates the relationship between energy (measured in MeV) and vertex resolution (measured in mm) for the reconstructed coordinates x, y, z as well as the overall radial resolution (R).The individual resolutions for x, y, and z coordinates show a consistent improvement with increasing energy. The radial resolution which combines the contributions from all three dimensions, also reflects this trend. 68
Figure 34: Comparison of the z_{res} obtained from center of charge method (using neutrino events) [10] and GCN (positron events). The GCN achieved a better resolution of 7 mm as compared to center of charge method that obtained 44 mm. 69
Figure 35: Training and validation loss vs. epochs for energy reconstruction. The initial decrease in training loss is accompanied by fluctuating validation loss. From epoch 25, both losses converge, indicating optimal model performance. 71
Figure 36: Distribution of energy resolution at 1 MeV, fitted to a Gaussian. A slight positive bias is observed. 71
Figure 37: Heatmap of $(E_{pred} - E_{dep})/E_{dep}$ at 1 MeV across detector volume. The cental yellow band indicates events whose predicted values closely match the true values. A slight positive bias is observed . . 72
Figure 38: Comparison of the energy resolution of antineutrino events E_{res} as foreseen in TAO[10] with positron events reonstructed by GCN. While TAO predicts a constant 0.3 % resolution for all energies, GCN shows a gradual improvement from 1.8 % at 1 MeV to 0.8 % at 10 MeV. 73
Figure 39: The plot shows the probabilities for $\nu_e \to \nu_\mu$ and $\nu_e \to \nu_\tau$ transitions for a fixed distance of 360 km. The solid lines represent the probabilities in vacuum, while the dashed lines show the effect of matter on these probabilities [150]. 77
Figure 40: The plot illustrates the potential to discover CPV as a function of the true value of the δ_{CP} . This analysis assumes a baseline length of 360 km (Zinkgruvan mine) and a total run time of 10 years, with 5 years of neutrino mode and 5 years of antineutrino mode. The different lines represent different levels of uncertainty in the normalization of the neutrino flux [149]. 78
Figure 41: The plot explains the precision of ESSnuSB's measurement on δ_{CP} by comparing its sensitivity to δ_{CP} as a function of its true value. The plot shows $\chi^2 = 1$ contour for different normalization percentages.[149]. 79
Figure 42: Layout of the ESS facility accommodating the ESSnuSB. The yellow labels represent the component of the ESS facility and to the left is the proposed ESSnuSB facility with the accumulator ring [158]. . . 80

Figure 43: The figure illustrates the modifications in the ESS layout to cater to ESSnuSB. The parts highlighted with yellow are the new requirements. This include: upgrading the linac, building an accumulator ring, neutrino target station and a near detctor [149]. 81
Figure 44: Schematic Overview of the ESSnuSB+ experiment. The diagram illustrates the flow of the experiment, from initial proton beam to the final neutrino production in the LEnuSTORM muon storage ring and various stages in between that involves refining the beam [159]. 82
Figure 45: The COMSOL simulation visualizes the pion profile at the interaction point for a particular horn configuration. The color bars represent the magnetic field strength in Tesla (T) and the velocity of pions in meters per second (m/s). The increased charge concentration at the inner horn edges results in a stronger magnetic field in these regions. The field deflects lower-velocity pions while focusing higher-velocity pions towards the target. 83
Figure 46: Workflow: The initial horn configuration is generated by FLUKA simulations. The simulated pion flux from FLUKA is analyzed in Python using the genetic algorithm to identify potential improvements in the configuration. The optimized configuration is then fed back into FLUKA and the process iterates until convergence is reached. 84
Figure 47: Transverse view of the horn with the key geometric parameters that influence its performance. 85
Figure 48: Total pion flux as a function of energy measured 10 meters from the horn, illustrating the distribution and intensity of pions produced across various energy levels. 86
Figure 49: Comparative analysis of the cross sectional pion distribution that falls at distance of z=10 m from the horn before (left) and after (right) optimization of the horn configuration. The optimization process has effectively improved the spatial confinement of the pions, leading to a more concentrated and focused distribution. . . 88
Figure 50: Comparison of optimized values and baseline values for all parameters: length dimensions (left) and current (right) across three runs. 89
Figure 51: Fitness Progression Across Generations: This plot illustrates the fitness values of each generation's best individual for three distinct runs. Each run exhibits a steep initial rise in fitness, reaching a peak of 0.860 by the twentieth generation, followed by a sustained plateau. 89

List of Tables

Table 1: Oscillation parameters obtained via nu-fit in September 2024 using Super Kamiokande atmospheric data for three flavor neutrino mixing. The best fit point (bfp) is the parameter value of those providing the best fit of models to data and the $s\sigma$ range is the range about this where we expect true parameter values will lie with around 99.7% confidence. It should be noted that for NO, $\Delta m^2_{3l} \equiv \Delta m^2_{31} > 0$, while for IO, $\Delta m^2_{3l} \equiv \Delta m^2_{32} < 0$ [39]. 11
Table 2: Summary of the IBD signal and background simulation results [97] [10]. 32
Table 3: Tuned hyperparameters used in the training. *Is the changed parameter in the energy reconstruction. 63
Table 4: The parameter definition and range for the ESSnuSB+ horn design . 85
Table 5: Crossover and Mutation of horn configurations 87
Table 6: Comparison of Optimized Parameters run1 with its Baseline Values . 88

List of Abbreviations

JUNO Jiangmen Underground Neutrino Observatory
TAO Taishan Antineutrino Observatory
SNO Sudbury Neutrino Observatory
NMO Neutrino Mass Ordering
IBD Inverse Beta Decay
GCNs Graph Convolutional Networks
ESSnuSB+ European Spallation Source neutrino Super Beam+
GA Genetic Algorithm
SM Standard Model
QCD Quantum Chromodynamics
CC Charged Current
NC Neutral Current
MSW Mikhaev, Smirnov, and Wolfenstein
NH Normal Hierarchy
IH Inverted Hierarchy
PMNS Pontecorvo, Maki, Nakagawa, and Sakata
GUT Grand Unified Theory
LS Liquid Scintillator
CD Central Detector
TT Top Tracker
PMTs Photomultiplier Tubes
SiPM Silicon Photomultipliers
FEE Frontend Electronics
ACU Automated Calibration Unit
HDPE High Density Polyethylene
LAB Liquid Alkyl Benzene
SST Stainless Steel Tank
GdLS Gadolinium-doped liquid scintillator
FPGAs Field Programmable Gate Arrays
FEB Front-End Board
ReLU Rectified Linear Unit
SELU Scaled Exponential Linear Unit

MSE Mean Squared Error

MC Monte Carlo

SNiPER Software for Non-collider Physics Experiments

EDM Event Data Model

Detsim detector simulation

Elecsim electronics simulation

ESS European Spallation Source

ESSnuSB European Spallation Source neutrino Super Beam

CPV Charge Parity Violation

LEnuSTORM Low Energy Neutrinos from STORed Muons

LEMNB Low Energy Monitored Neutrino Beam

FLUKA FLUktuierende KAskade

CLs Confidence Level with a signal hypothesis

CLS Cable Loop System

SPAD Single Photon Avalanche Diodes

LAPPD Large Area Picosecond Photodetectors

TTS Transit Time Spread

PDE Photon Detection Efficiency

Bibliography

[1] W. Pauli. "Offener Brief an die Gruppe der Radioaktiven. (Dec. 19)". In: (Dec. 1930).

[2] C. L. Cowan et al. "Detection of the Free Neutrino: a Confirmation". In: *Science 124.3212* (1956). DOI: 10.1126/science.124.3212.103.

[3] Q. R. Ahmad et al. "Measurement of the Rate of $e + d \rightarrow p + p + e$ Interactions Produced by 8 B Solar Neutrinos at the Sudbury Neutrino Observatory". In: *Science 191.4224* (7 July 2001). DOI: 10.1103/PhysRevLett.87.071301.

[4] Y. Ashie et al. "Evidence for an Oscillatory Signature in Atmospheric Neutrino Oscilla- tions". In: *Phys. Rev. Lett. 93* (10 Sept. 2004). DOI: 10.1103/PhysRevLett.93.101801.

[5] Nobel Foundation. "The Nobel Prize in Physics". In: *Phys. Rev. Lett. 93* (2015). URL: https://www.nobelprize.%20org/prizes/physics/2015/.

[6] T. Adam, F. An, G. An, et al. "JUNO Conceptual Design Report". In: (2015). arXiv: 1508.07166 [physics.ins-det].

[7] Fengpeng An et al. "Neutrino Physics with JUNO". In: *Journal of Physics G: Nuclear and Particle Physics* (2016). DOI: 10.1088/0954-3899/43/3/030401.

[8] G. Bak et al. "Measurement of Reactor Antineutrino Oscillation Amplitude and Frequency at RENO." In: *Phys. Rev. Lett.* (2018).

[9] H. de Kerret et al. "First Double Chooz 13 Measurement via Total Neutron Capture Detection". In: (2019). URL: arXiv:1901.09445.

[10] JUNO Collaboration, Angel Abusleme, Thomas Adam, et al. "TAO Conceptual Design Report: A Precision Measurement of the Reactor Antineutrino Spectrum with Sub-percent Energy Resolution". In: (May 2020).

[11] Roland Garoby, A Vergara, H Danared, et al. "The European Spallation Source Design". In: *Physica Scripta* 93.1 (Dec. 2017), p. 014001. DOI: 10.1088/1402-4896/aa9bff. URL: https://dx.doi.org/10.1088/1402-4896/aa9bff.

[12] A. Ferrari, P.R. Sala, A. Fasso, et al. In: *Fluka: A multi-particle transport code* (Dec. 2005). DOI: 10.2172/877507.

[13] M. Tanabashi, K. Hagiwara, K. Hikasa, et al. "Review of Particle Physics". In: *Phys. Rev. D* 98 (3 Aug. 2018), p. 030001. DOI: 10.1103/PhysRevD.98.030001. URL: https://link.aps.org/doi/10.1103/PhysRevD.98.030001.

[14] M. Tanabashi and et al. "Review of Particle Physics". In: *Phys. Rev. D* 98.3 (Aug. 2018), p. 030001. DOI: 10.1103/PhysRevD.98.030001. URL: https://link.aps.org/doi/10.1103/PhysRevD.98.030001.

[15] Peter W. Higgs. "Broken Symmetries and the Masses of Gauge Bosons". In: *Phys. Rev. Lett.* 13 (16 Oct. 1964), pp. 508–509. DOI: 10.1103/PhysRevLett.13.508. URL: https://link.aps.org/doi/10.1103/PhysRevLett.13.508.

[16] F. Englert and R. Brout. "Broken Symmetry and the Mass of Gauge Vector Mesons". In: *Phys. Rev. Lett.* 13 (9 Aug. 1964), pp. 321–323. DOI: 10.1103/PhysRevLett.13.321. URL: https://link.aps.org/doi/10.1103/PhysRevLett.13.321.

[17] Cush. *Standard Model of Elementary Particles*. https://en.wikipedia.org/wiki/File:Standard_Model_of_Elementary_Particles.svg. Image from Wikimedia Commons, License: Public Domain. 2024. (Visited on 12/19/2024).

[18] R. Ansari. "Measurement of the standard model parameters from a study of W and Z bosons". In: *Physics Letters B* 186.3 (1987), pp. 440–451. ISSN: 0370-2693. DOI: 10.1016/0370-2693(87)90324-8. URL: https://www.sciencedirect.com/science/article/pii/0370269387903248.

[19] P. Schmueser. "Feynman graphs and gauge theories for experimental physicists ". In: *Springer* (1995).

[20] B. Pontecorvo. "Inverse beta processes and nonconservation of lepton charge". In: *Zhur. Eksptl'. i Teoret. Fiz.* 34 (1958). URL: https://www.osti.gov/biblio/434923.

[21] Bruno Pontecorvo. "Neutrino experiments and the problem of conservation of leptonic charge". In: *Sov. Phys. JETP* 26.984-988 (1968), p. 165.

[22] Raymond Davis. "A review of the homestake solar neutrino experiment". In: *Progress in Particle and Nuclear Physics* 32 (1994), pp. 13–32. ISSN: 0146-6410. DOI: https://doi.org/10.1016/0146-6410(94)90004-3. URL: https://www.sciencedirect.com/science/article/pii/0146641094900043.

[23] S. M. Bilenky. "Prehistory of Neutrino Oscillations". In: *arXiv e-prints* (Feb. 2019). arXiv: 1902.10052 [physics.hist-ph]. URL: https://arxiv.org/abs/1902.10052.

[24] Y. Fukuda, T. Hayakawa, E. Ichihara, et al. "Measurements of the Solar Neutrino Flux from Super-Kamiokande's First 300 Days". In: *Phys. Rev. Lett.* 81

(6 Aug. 1998), pp. 1158–1162. DOI: 10.1103/PhysRevLett.81.1158. URL: https://link.aps.org/doi/10.1103/PhysRevLett.81.1158.

[25] S. N. O. Collaboration. "Direct Evidence for Neutrino Flavor Transformation from Neutral-Current Interactions in the Sudbury Neutrino Observatory". In: *Phys. Rev. Lett.* 89.1 (June 2002), p. 011301. DOI: 10.1103/PhysRevLett.89.011301. URL: https://link.aps.org/doi/10.1103/PhysRevLett.89.011301.

[26] K. Eguchi and et al. "First Results from KamLAND: Evidence for Reactor Antineutrino Disappearance". In: *Phys. Rev. Lett.* 90.2 (Jan. 2003), p. 021802. DOI: 10.1103/PhysRevLett.90.021802.

[27] K. Abe and et al. Abgrall. "Indication of Electron Neutrino Appearance from an Accelerator-Produced Off-Axis Muon Neutrino Beam". In: *Phys. Rev. Lett.* 107 (4 July 2011), p. 041801. DOI: 10.1103/PhysRevLett.107.041801. URL: https://link.aps.org/doi/10.1103/PhysRevLett.107.041801.

[28] F. P. An and et al. Bai. "Observation of Electron-Antineutrino Disappearance at Daya Bay". In: *Phys. Rev. Lett.* 108 (17 Apr. 2012), p. 171803. DOI: 10.1103/PhysRevLett.108.171803. URL: https://link.aps.org/doi/10.1103/PhysRevLett.108.171803.

[29] Y. Abe and et al. Aberle. "Indication of Reactor $\overline{\nu}_e$ Disappearance in the Double Chooz Experiment". In: *Phys. Rev. Lett.* 108 (13 Mar. 2012), p. 131801. DOI: 10.1103/PhysRevLett.108.131801. URL: https://link.aps.org/doi/10.1103/PhysRevLett.108.131801.

[30] J. K. Ahn and et al. Chebotaryov. "Observation of Reactor Electron Antineutrinos Disappearance in the RENO Experiment". In: *Phys. Rev. Lett.* 108 (19 May 2012), p. 191802. DOI: 10.1103/PhysRevLett.108.191802. URL: https://link.aps.org/doi/10.1103/PhysRevLett.108.191802.

[31] M. C. Gonzalez-Garcia and Yosef Nir. "Neutrino masses and mixing: evidence and implications". In: *Reviews of Modern Physics* 75.2 (2003), pp. 345–402. DOI: 10.1103/RevModPhys.75.345.

[32] S. M. Bilenky and S. T. Petcov. "Massive Neutrinos and Neutrino Oscillations". In: *Reviews of Modern Physics* 59.3 (1987), pp. 671–707. DOI: 10.1103/RevModPhys.59.671.

[33] L. Wolfenstein. "Neutrino oscillations in matter". In: *Phys. Rev. D* 17 (9 May 1978), pp. 2369–2374. DOI: 10.1103/PhysRevD.17.2369. URL: https://link.aps.org/doi/10.1103/PhysRevD.17.2369.

[34] Shawn Westerdale. "Neutrino Mass Problem: Masses and Oscillations". In: *URl: http://web. mit. edu/shawest/Public/8.06/termPaperDraft. pdf* (2010).

[35] G. Barenboim. "Neutrinos Matter". In: *CERN Yellow Report* P159 (2006), pp. 1–40. URL: https://cds.cern.ch/record/1114392/files/p159.pdf.

[36] L. Wolfenstein. "Neutrino oscillations in matter". In: *Phys. Rev. D* 17 (9 May 1978), pp. 2369–2374. DOI: 10.1103/PhysRevD.17.2369. URL: https://link.aps.org/doi/10.1103/PhysRevD.17.2369.

[37] S. M. Bilenky. "Neutrino masses, mixing and oscillations". In: (2000). arXiv: hep-ph/0001311 [hep-ph].

[38] NuFIT Collaboration. *v5.3: Three-neutrino fit based on data available in March 2024*. http://www.nu-fit.org/?q=node/278. Accessed on December 19, 2024. Mar. 2024.

[39] Ivan Esteban, M. C. Gonzalez-Garcia, Michele Maltoni, et al. "NuFit-6.0: updated global analysis of three-flavor neutrino oscillations". In: *Journal of High Energy Physics* 2024.12 (Dec. 2024). ISSN: 1029-8479. DOI: 10.1007/jhep12(2024)216. URL: http://dx.doi.org/10.1007/JHEP12(2024)216.

[40] J. N. Bahcall and M. H. Pinsonneault. "Solar Models and Solar Neutrinos: A Review". In: *Physics Reports* 333.2 (1995), pp. 121–170. DOI: 10.1016/0370-1573(00)00030-5.

[41] E. G. Adelberger and et al. García. "Solar fusion cross sections. II. The pp and CNO cycles". In: *Reviews of Modern Physics* 83.1 (Apr. 2011), pp. 195–245. ISSN: 1539-0756. DOI: 10.1103/RevModPhys.83.195. URL: http://dx.doi.org/10.1103/RevModPhys.83.195.

[42] Raymond Davis, Don S. Harmer, and Kenneth C. Hoffman. "Search for Neutrinos from the Sun". In: *Phys. Rev. Lett.* 20 (21 May 1968), pp. 1205–1209. DOI: 10.1103/PhysRevLett.20.1205. URL: https://link.aps.org/doi/10.1103/PhysRevLett.20.1205.

[43] K. S. Hirata, T. Kajita, T. Kifune, et al. "Observation of ^{8}B solar neutrinos in the Kamiokande-II detector". In: *Phys. Rev. Lett.* 63 (1 July 1989), pp. 16–19. DOI: 10.1103/PhysRevLett.63.16. URL: https://link.aps.org/doi/10.1103/PhysRevLett.63.16.

[44] J. N. Abdurashitov, V. N. Gavrin, V. V. Gorbachev, et al. "Measurement of the solar neutrino capture rate with gallium metal. III. Results for the 2002–2007 data-taking period". In: *Phys. Rev. C* 80 (1 July 2009), p. 015807. DOI: 10.1103/PhysRevC.80.015807. URL: https://link.aps.org/doi/10.1103/PhysRevC.80.015807.

[45] W. Hampel, J. Handt, G. Heusser, et al. "GALLEX solar neutrino observations: results for GALLEX IV". In: *Physics Letters B* 447.1 (1999), pp. 127–133. ISSN: 0370-2693. DOI: https://doi.org/10.1016/S0370-2693(98)01579-2. URL: https://www.sciencedirect.com/science/article/pii/S0370269398015792.

[46] B. Aharmim, S. N. Ahmed, A. E. Anthony, et al. "Combined analysis of all three phases of solar neutrino data from the Sudbury Neutrino Observatory". In: *Phys. Rev. C* 88 (2 Aug. 2013), p. 025501. DOI: 10.1103/PhysRevC.

88.025501. URL: https://link.aps.org/doi/10.1103/PhysRevC.88.025501.

[47] G. Bellini, J. Benziger, D. Bick, et al. "Final results of Borexino Phase-I on low-energy solar neutrino spectroscopy". In: *Phys. Rev. D* 89 (11 June 2014), p. 112007. DOI: 10.1103/PhysRevD.89.112007. URL: https://link.aps.org/doi/10.1103/PhysRevD.89.112007.

[48] Borexino Collaboration. "Direct Detection of Solar CNO Neutrinos". In: *Physical Review Letters* 123.14 (2020), p. 141802. DOI: 10.1103/PhysRevLett.123.141802.

[49] Jai Sam Kim and C. W. Kim. *Full Numerical Estimation of Neutrino Mixing Parameters from Solar Neutrino Data*. 1999. arXiv: hep-ph/9909428 [hep-ph].

[50] A. Gando, Y. Gando, K. Ichimura, et al. "Constraints on θ_{13} from a three-flavor oscillation analysis of reactor antineutrinos at KamLAND". In: *Phys. Rev. D* 83 (5 Mar. 2011), p. 052002. DOI: 10.1103/PhysRevD.83.052002. URL: https://link.aps.org/doi/10.1103/PhysRevD.83.052002.

[51] F. Capozzi. "DUNE as the Next-Generation Solar Neutrino Experiment". In: *Physical Review Letters* 123.13 (2019), p. 131803. DOI: 10.1103/PhysRevLett.123.131803. URL: https://link.aps.org/doi/10.1103/PhysRevLett.123.131803.

[52] Takaaki Kajita. "Atmospheric neutrinos and discovery of neutrino oscillations". In: *Proc. Japan Acad. B* 86 (2010), pp. 303–321. DOI: 10.2183/pjab.86.303.

[53] K. Abe, C. Bronner, Y. Haga, et al. "Atmospheric neutrino oscillation analysis with external constraints in Super-Kamiokande I-IV". In: *Phys. Rev. D* 97 (7 Apr. 2018), p. 072001. DOI: 10.1103/PhysRevD.97.072001. URL: https://link.aps.org/doi/10.1103/PhysRevD.97.072001.

[54] R. Becker-Szendy et al. "A Search for muon-neutrino oscillations with the IMB detector". In: *Phys. Rev. Lett.* 69 (1992), pp. 1010–1013. DOI: 10.1103/PhysRevLett.69.1010.

[55] M. G. Aartsen, M. Ackermann, J. Adams, et al. "Measurement of atmospheric tau neutrino appearance with IceCube DeepCore". In: *Phys. Rev. D* 99 (3 Feb. 2019), p. 032007. DOI: 10.1103/PhysRevD.99.032007. URL: https://link.aps.org/doi/10.1103/PhysRevD.99.032007.

[56] S. Adrián-Martínez, I. Al Samarai, A. Albert, et al. "Measurement of atmospheric neutrino oscillations with the ANTARES neutrino telescope". In: *Physics Letters B* 714.2 (2012), pp. 224–230. ISSN: 0370-2693. DOI: https://doi.org/10.1016/j.physletb.2012.07.002. URL: https://www.sciencedirect.com/science/article/pii/S037026931200740X.

[57] P. Adamson, L. Aliaga, D. Ambrose, et al. "Measurement of the Neutrino Mixing Angle θ_{23} in NOvA". In: *Phys. Rev. Lett.* 118 (15 Apr. 2017), p. 151802.

DOI: 10.1103/PhysRevLett.118.151802. URL: https://link.aps.org/doi/10.1103/PhysRevLett.118.151802.

[58] K. Abe, J. Amey, C. Andreopoulos, et al. "Updated T2K measurements of muon neutrino and antineutrino disappearance using 1.5×10^{21} protons on target". In: *Phys. Rev. D* 96 (1 July 2017), p. 011102. DOI: 10.1103/PhysRevD.96.011102. URL: https://link.aps.org/doi/10.1103/PhysRevD.96.011102.

[59] T. Thakore et al. "DUNE atmospheric neutrinos: Earth Tomography". In: *arXiv* 2110.00003 (2021). URL: https://arxiv.org/abs/2110.00003.

[60] P. Vogel, L.J. Wen, and C. Zhang. "Neutrino oscillation studies with reactors". In: *Nature Communications* 6.1 (Apr. 2015). ISSN: 2041-1723. DOI: 10.1038/ncomms7935. URL: http://dx.doi.org/10.1038/ncomms7935.

[61] H. de Kerret et al. "First Double Chooz θ_{13} Measurement via Total Neutron capture Detection". In: *Nature Physics* (2020).

[62] Fengpeng An et al. "Measurement of the Reactor Antineutrino Flux and Spectrum at Daya Bay." In: *Phys. Rev. Lett.* (2017).

[63] Fengpeng An et al. "Measurement of the Reactor Antineutrino Oscillation Amplitude and requency at RENO." In: *Phys. Rev. Lett.* (2018).

[64] Nikolaos Charitonidis, Andrea Longhin, Michelangelo Pari, et al. "Design and Diagnostics of High-Precision Accelerator Neutrino Beams". In: *Applied Sciences* 11.4 (Feb. 2021), p. 1644. ISSN: 2076-3417. DOI: 10.3390/app11041644. URL: http://dx.doi.org/10.3390/app11041644.

[65] K. Abe, N. Akhlaq, R. Akutsu, et al. "Measurement of the charged-current electron (anti-)neutrino inclusive cross-sections at the T2K off-axis near detector ND280". In: *Journal of High Energy Physics* 2020.10 (Oct. 2020). ISSN: 1029-8479. DOI: 10.1007/jhep10(2020)114. URL: http://dx.doi.org/10.1007/JHEP10(2020)114.

[66] Sowjanya Gollapinni. *Accelerator-based Short-baseline Neutrino Oscillation Experiments*. 2015. arXiv: 1510.04412 [hep-ex].

[67] X.-G. Lu, Z. Ahmad Dar, F. Akbar, et al. "Exploring neutrino–nucleus interactions in the GeV regime using MINERvA". In: *The European Physical Journal Special Topics* 230.24 (Nov. 2021), pp. 4243–4257. ISSN: 1951-6401. DOI: 10.1140/epjs/s11734-021-00296-6. URL: http://dx.doi.org/10.1140/epjs/s11734-021-00296-6.

[68] Pedro A.N. Machado, Ornella Palamara, and David W. Schmitz. "The Short-Baseline Neutrino Program at Fermilab". In: *Annual Review of Nuclear and Particle Science* 69.1 (Oct. 2019), pp. 363–387. ISSN: 1545-4134. DOI: 10.1146/annurev-nucl-101917-020949. URL: http://dx.doi.org/10.1146/annurev-nucl-101917-020949.

[69] J. G. Walsh. *CP-violation search with T2K data*. 2022. arXiv: 2208.01164 [hep-ex].

[70] Son Cao. *Long Baseline Neutrino Oscillation Results (T2K and NOvA)*. 2023. arXiv: 2310.09855 [hep-ex].

[71] B. Abi, R. Acciarri, Mario A. Acero, et al. "Deep Underground Neutrino Experiment (DUNE), Far Detector Technical Design Report, Volume I: Introduction to DUNE". In: (2020). arXiv: 2002.02967 [physics.ins-det].

[72] Mehedi Masud, Animesh Chatterjee, and Poonam Mehta. "Probing the CP violation signal at DUNE in the presence of non-standard neutrino interactions". In: *Journal of Physics G: Nuclear and Particle Physics* 43.9 (Aug. 2016), p. 095005. ISSN: 1361-6471. DOI: 10.1088/0954-3899/43/9/095005. URL: http://dx.doi.org/10.1088/0954-3899/43/9/095005.

[73] A. Alekou, E. Baussan, A. K. Bhattacharyya, et al. "The ESSnuSB Design Study: Overview and Future Prospects". In: *Universe* 9.8 (July 2023), p. 347. ISSN: 2218-1997. DOI: 10.3390/universe9080347. URL: http://dx.doi.org/10.3390/universe9080347.

[74] A. Gando, Y. Gando, T. Hachiya, et al. "Search for Majorana Neutrinos Near the Inverted Mass Hierarchy Region with KamLAND-Zen". In: *Physical Review Letters* 117.8 (Aug. 2016). ISSN: 1079-7114. DOI: 10.1103/physrevlett.117.082503. URL: http://dx.doi.org/10.1103/PhysRevLett.117.082503.

[75] S. Abe, T. Araki, K. Chiba, et al. *Search for Majorana Neutrinos with the Complete KamLAND-Zen Dataset*. 2024. arXiv: 2406.11438 [hep-ex]. URL: https://arxiv.org/abs/2406.11438.

[76] J. Bernabéu, Sergio Palomares-Ruiz, and S.T. Petcov. "Atmospheric neutrino oscillations, 13 and neutrino mass hierarchy". In: *Nuclear Physics B* 669.1 (2003), pp. 255–276.

[77] Amol S. Dighe and Alexei Yu. Smirnov. "Identifying the neutrino mass spectrum from a supernova neutrino burst". In: *Phys. Rev. D* 62 (3 July 2000), p. 033007.

[78] S.T. Petcov and M. Piai. "The LMA MSW solution of the solar neutrino problem, inverted neutrino mass hierarchy and reactor neutrino experiments". In: *Physics Letters B* 533.1 (2002), pp. 94–106.

[79] Pablo F. de Salas, Stefano Gariazzo, Olga Mena, et al. "Neutrino Mass Ordering from Oscillations and Beyond: 2018 Status and Future Prospects". In: *Frontiers in Astronomy and Space Sciences* 5 (Oct. 2018). ISSN: 2296-987X. DOI: 10.3389/fspas.2018.00036. URL: http://dx.doi.org/10.3389/fspas.2018.00036.

[80] S. Aiello, A. Albert, S. Alves Garre, et al. "Determining the neutrino mass ordering and oscillation parameters with KM3NeT/ORCA". In: *The European Physical Journal C* 82.1 (Jan. 2022). ISSN: 1434-6052. DOI: 10.1140/epjc/

s10052-021-09893-0. URL: http://dx.doi.org/10.1140/epjc/s10052-021-09893-0.

[81] PINGU Collaboration. "Letter of Intent: The Precision IceCube Next Generation Upgrade (PINGU)". In: (2017). arXiv: 1401.2046 [physics.ins-det].

[82] Ke. Abe, H. Aihara, A. Aimi, et al. "Hyper-Kamiokande Design Report". In: (May 2018). working paper or preprint. URL: https://hal.science/hal-01801891.

[83] J. H. Christenson, J. W. Cronin, V. L. Fitch, et al. "Evidence for the 2π Decay of the K_2^0 Meson". In: *Phys. Rev. Lett.* 13 (4 July 1964), pp. 138–140. DOI: 10.1103/PhysRevLett.13.138. URL: https://link.aps.org/doi/10.1103/PhysRevLett.13.138.

[84] NOvA Collaboration, M. A. Acero, B. Acharya, et al. "Search for CP-violating Neutrino Non-Standard Interactions with the NOvA Experiment". In: (2024). arXiv: 2403.07266 [hep-ex].

[85] A. Aguilar, L. B. Auerbach, R. L. Burman, et al. "Evidence for neutrino oscillations from the observation of $\overline{\nu}_e$ appearance in a $\overline{\nu}_\mu$ beam". In: *Phys. Rev. D* 64 (11 Nov. 2001), p. 112007.

[86] A. Aguilar-Arevalo et al. "Excess in the MiniBooNE Search for $\overline{\nu}_\mu \to \overline{\nu}_e$ Oscillations". In: *Physical Review Letters* 121.22 (2021), p. 221801. DOI: 10.1103/PhysRevLett.121.221801.

[87] Joachim Kopp, Pedro AN Machado, Michele Maltoni, et al. "Sterile neutrino oscillations: the global picture". In: *Journal of High Energy Physics* 2013.5 (2013), pp. 1–52.

[88] C Giunti, M Laveder, YF Li, et al. "Pragmatic view of short-baseline neutrino oscillations". In: *Physical Review D* 88.7 (2013), p. 073008.

[89] P. Minkowski. "The neutrino mass and the seesaw mechanism". In: *Physics Letters B* 67.5 (1977), pp. 421–428. DOI: 10.1016/0370-2693(77)90665-7.

[90] Sebastian Böser, Christian Buck, Carlo Giunti, et al. "Status of light sterile neutrino searches". In: *Progress in Particle and Nuclear Physics* 111 (Mar. 2020), p. 103736. ISSN: 0146-6410. DOI: 10.1016/j.ppnp.2019.103736. URL: http://dx.doi.org/10.1016/j.ppnp.2019.103736.

[91] J. B. Birks. "Scintillations from Organic Crystals: Specific Fluorescence and Relative Response to Different Radiations". In: *Proceedings of the Physical Society A* 64.10 (1951), pp. 874–877. DOI: 10.1088/0370-1298/64/10/303.

[92] C. Cao et al. "Mass production and characterization of 3-inch PMTs for the JUNO experiment". In: *Nuclear Instruments and Methods in Physics Research Section A* 1005 (2021), p. 165347. DOI: 10.1016/j.nima.2021.165347. eprint: arXiv:2102.11538.

[93] A. Abusleme et al. "Sub-percent Precision Measurement of Neutrino Oscillation Parameters with JUNO". In: *Chin. Phys. C* 46.12 (2022), p. 123001. DOI: 10.1088/1674-1137/ac82d2. arXiv: 2204.13249 [hep-ex].

[94] X. Chen, G.F. Cao, M.H. Qu, et al. "Burn-in Test and Thermal Performance Evaluation of Silicon Photomultipliers for the JUNO-TAO Experiment". In: *Journal of Instrumentation* 19 (July 2024), p. C07008. DOI: 10.1088/1748-0221/19/07/C07008.

[95] J. Liu, B. Cai, R. Carr, et al. "Automated Calibration System for a High-Precision Measurement of Neutrino Mixing Angle θ_{13} with the Daya Bay Antineutrino Detectors". In: *Nucl. Instrum. Meth. A* 750 (2014), pp. 19–37. DOI: 10.1016/j.nima.2014.02.049.

[96] Hangkun Xu, Angel Abusleme, Nikolay V. Anfimov, et al. "Calibration strategy of the JUNO-TAO experiment". In: *The European Physical Journal C* 82.12 (Dec. 2022). ISSN: 1434-6052. DOI: 10.1140/epjc/s10052-022-11069-3. URL: http://dx.doi.org/10.1140/epjc/s10052-022-11069-3.

[97] Ruhui Li et al. "Detector optimization to reduce the cosmogenic neutron backgrounds in the TAO experiment". Version 4. In: *arXiv preprint arXiv:2206.01112* (Aug. 2022). arXiv: 2206.01112 [physics.ins-det].

[98] D. Adey, F. P. An, A. B. Balantekin, et al. "Extraction of the 235U and 239Pu Antineutrino Spectra at Daya Bay". In: *Physical Review Letters* 123.11 (Sept. 2019). ISSN: 1079-7114. DOI: 10.1103/physrevlett.123.111801. URL: http://dx.doi.org/10.1103/PhysRevLett.123.111801.

[99] M. Estienne et al. "Updated Summation Model: An Improved Agreement with the Daya Bay Antineutrino Fluxes". In: *Phys. Rev. Lett.* 123.2 (2019), p. 022502. DOI: 10.1103/PhysRevLett.123.022502. arXiv: 1904.09358 [nucl-ex].

[100] A. A. Sonzogni, M. Nino, and E. A. McCutchan. "Revealing fine structure in the antineutrino spectra from a nuclear reactor". In: *Physical Review C* 98.1 (July 2018). ISSN: 2469-9993. DOI: 10.1103/physrevc.98.014323. URL: http://dx.doi.org/10.1103/PhysRevC.98.014323.

[101] Francesco Capozzi, Eligio Lisi, and Antonio Marrone. "Mapping reactor neutrino spectra from TAO to JUNO". In: *Physical Review D* 102.5 (Sept. 2020). ISSN: 2470-0029. DOI: 10.1103/physrevd.102.056001. URL: http://dx.doi.org/10.1103/PhysRevD.102.056001.

[102] Alexander L Read. "Presentation of search results: The CL(s) technique." In: *J. Phs. G* (2002).

[103] Thomas Junk. "Confidence level computation for combining searches with small statistics". In: *Nucl. Instrum. Meth. A* (1999).

[104] P. Adamson et al. "Improved Constraints on Sterile Neutrino Mixing from Disappearance Searches in the MINOS, MINOS+, Daya Bay, and Bugey-3 Experiments". In: *Nucl. Instrum. Meth. A* (2020).

[105] D. Adey, F. P. An, A. B. Balantekin, et al. "Improved measurement of the reactor antineutrino flux at Daya Bay". In: *Physical Review D* 100.5 (Sept. 2019). ISSN: 2470-0029. DOI: 10.1103/physrevd.100.052004. URL: http://dx.doi.org/10.1103/PhysRevD.100.052004.

[106] Warren S. McCulloch and Walter Pitts. " A logical calculus of the ideas immanent in nervous activity. " In: *The bulletin of mathematical biophysics, 5(4):115– 133* (1943).

[107] Ian Goodfellow, Yoshua Bengio, and Aaron Courville. *Deep Learning*. http://www.deeplearningbook.org. MIT Press, 2016.

[108] Venkata Sasank Mudigonda. *A Quick Hands-on Intro to Deep Learning — mvshashank08*. https://medium.com/@mvshashank08/a-quick-hands-on-intro-to-deep-learning-f12cd5cbf2f9. [Accessed 18-07-2024].

[109] Aurélien Géron. *Hands-on machine learning with Scikit-Learn and TensorFlow : concepts, tools, and techniques to build intelligent systems*. Sebastopol, CA: O'Reilly Media, 2017. ISBN: 978-1491962299.

[110] Shiv Ram Dubey, Satish Kumar Singh, and Bidyut Baran Chaudhuri. "A Comprehensive Survey on Activation Functions in Neural Networks". In: *Neurocomputing* (2021). DOI: 10.1016/j.neucom.2021.09.14545. URL: https://arxiv.org/pdf/2109.14545.pdf.

[111] Abien Fred Agarap. *Deep Learning using Rectified Linear Units (ReLU)*. 2019. arXiv: 1803.08375 [cs.NE]. URL: https://arxiv.org/abs/1803.08375.

[112] Günter Klambauer, Thomas Unterthiner, Andreas Mayr, et al. *Self-Normalizing Neural Networks*. 2017. arXiv: 1706.02515 [cs.LG]. URL: https://arxiv.org/abs/1706.02515.

[113] Nitish Srivastava, Geoffrey Hinton, Alex Krizhevsky, et al. "Dropout: A Simple Way to Prevent Neural Networks from Overfitting". In: *Journal of Machine Learning Research* 15 (June 2014), pp. 1929–1958.

[114] Michaël Defferrard, Xavier Bresson, and Pierre Vandergheynst. *Convolutional Neural Networks on Graphs with Fast Localized Spectral Filtering*. 2017. arXiv: 1606.09375 [cs.LG]. URL: https://arxiv.org/abs/1606.09375.

[115] Jie Zhou, Ganqu Cui, Shengding Hu, et al. "Graph neural networks: A review of methods and applications". In: *AI Open* 1 (2020), pp. 57–81. ISSN: 2666-6510. DOI: https://doi.org/10.1016/j.aiopen.2021.01.001. URL: https://www.sciencedirect.com/science/article/pii/S2666651021000012.

[116] Bharti Khemani, Shruti Patil, Ketan Kotecha, et al. "A review of graph neural networks: concepts, architectures, techniques, challenges, datasets, applications, and future directions". In: *Journal of Big Data* 11.1 (Jan. 2024), p. 18. ISSN: 2196-1115. DOI: 10.1186/s40537-023-00876-4. URL: https://doi.org/10.1186/s40537-023-00876-4.

[117] Guohao Li, Chenxin Xiong, Ali Thabet, et al. *Deeper{GCN}: Training Deeper {GCN}s with Generalized Aggregation Functions*. 2021. URL: https://openreview.net/forum?id=dmCL033_YwO.

[118] Thomas N. Kipf and Max Welling. *Semi-Supervised Classification with Graph Convolutional Networks*. 2017. arXiv: 1609.02907 [cs.LG]. URL: https://arxiv.org/abs/1609.02907.

[119] William L. Hamilton, Rex Ying, and Jure Leskovec. *Inductive Representation Learning on Large Graphs*. 2018. arXiv: 1706.02216 [cs.SI]. URL: https://arxiv.org/abs/1706.02216.

[120] Yue Wang, Yongbin Sun, Ziwei Liu, et al. *Dynamic Graph CNN for Learning on Point Clouds*. 2019. arXiv: 1801.07829 [cs.CV]. URL: https://arxiv.org/abs/1801.07829.

[121] Madeleine Udell. *Introduction to spectral graph theory*. 2011.

[122] Mingguo He, Zhewei Wei, and Ji-Rong Wen. *Convolutional Neural Networks on Graphs with Chebyshev Approximation, Revisited*. 2024. arXiv: 2202.03580 [cs.LG]. URL: https://arxiv.org/abs/2202.03580.

[123] Ron Levie, Federico Monti, Xavier Bresson, et al. *CayleyNets: Graph Convolutional Neural Networks with Complex Rational Spectral Filters*. 2018. arXiv: 1705.07664 [cs.LG]. URL: https://arxiv.org/abs/1705.07664.

[124] Mingguo He, Zhewei Wei, and Ji-Rong Wen. *Convolutional Neural Networks on Graphs with Chebyshev Approximation, Revisited*. 2024. arXiv: 2202.03580 [cs.LG]. URL: https://arxiv.org/abs/2202.03580.

[125] M. Bachlechner, T. Birkenfeld, P. Soldin, et al. "Partition pooling for convolutional graph network applications in particle physics". In: *Journal of Instrumentation* 17.10 (Oct. 2022), P10004. ISSN: 1748-0221. DOI: 10.1088/1748-0221/17/10/p10004. URL: http://dx.doi.org/10.1088/1748-0221/17/10/P10004.

[126] David Arthur and Sergei Vassilvitskii. "K-Means++: The Advantages of Careful Seeding". In: vol. 8. Jan. 2007, pp. 1027–1035. DOI: 10.1145/1283383.1283494.

[127] Yangqing Jia, Chang Huang, and T. Darrell. "Beyond spatial pyramids: Receptive field learning for pooled image features". In: June 2012, pp. 3370–3377. ISBN: 978-1-4673-1226-4. DOI: 10.1109/CVPR.2012.6248076.

[128] Kaiming He, Xiangyu Zhang, Shaoqing Ren, et al. "Deep Residual Learning for Image Recognition". In: vol. abs/1512.03385. 2015. arXiv: 1512.03385. URL: http://arxiv.org/abs/1512.03385.

[129] Alex Lenail. *NN-SVG: Publication-ready NN-architecture schematics*. https://alexlenail.me/NN-SVG/index.html. Accessed: 2024-11-25.

[130] D. E. Goldberg. *Genetic Algorithms in Search, Optimization, and Machine Learning*. Addison-Wesley., 1989.

[131] R. Haupt and S. E. Haupt. *Practical Genetic Algorithms*. 2nd ed. John Wiley Sons, 2004. ISBN: 0-471-45565-2.

[132] M. Mitchell. *An introduction to genetic algorithms*. The MIT Press., 1996.

[133] Charles Peck and Atam Dhawan. "Genetic Algorithms as Global Random Search Methods: An Alternative Perspective". In: *Evolutionary Computation - EC* 3 (Mar. 1995), pp. 39–80. DOI: 10.1162/evco.1995.3.1.39.

[134] Charles Peck and Atam Dhawan. "Genetic Algorithms as Global Random Search Methods: An Alternative Perspective". In: *Evolutionary Computation - EC* 3 (Mar. 1995), pp. 39–80. DOI: 10.1162/evco.1995.3.1.39.

[135] Ali Ghaheri, Saeed Shoar, Mohammad Naderan, et al. "The applications of genetic algorithms in medicine". In: *Oman medical journal* 30.6 (2015), p. 406.

[136] Sourabh S. Patil and A. S. Bhalchandra. "Pattern recognition using genetic algorithm". In: *2017 International Conference on I-SMAC (IoT in Social, Mobile, Analytics and Cloud) (I-SMAC)*. 2017, pp. 310–314. DOI: 10.1109/I-SMAC.2017.8058361.

[137] Mrinalini Rana and Jimmy Singla. "A Systematic Review on Data Mining Rules Generation Optimizing via Genetic Algorithm". In: *SSRN Electronic Journal* (Jan. 2020). DOI: 10.2139/ssrn.3564032.

[138] Marcello Fera, Fabio Fruggiero, A Lambiase, et al. "A modified genetic algorithm for time and cost optimization of an additive manufacturing single-machine scheduling". In: *International Journal of Industrial Engineering Computations* 9.4 (2018), pp. 423–438.

[139] Rui Dilao. "From Charles Darwin to evolutionary genetic algorithms". In: Jan. 2009, pp. 1–11.

[140] S. Sivanandam and S N Deepa. *Introduction to Genetic Algorithms*. Jan. 2008. ISBN: 978-3-540-73189-4. DOI: 10.1007/978-3-540-73190-0.

[141] R. Salomon. "Evolutionary algorithms and gradient search: similarities and differences". In: *IEEE Transactions on Evolutionary Computation* 2.2 (1998), pp. 45–55. DOI: 10.1109/4235.728207.

[142] J. Zou, Xiang-Jie Huang, W.D. Li, et al. "SNiPER: an offline software framework for non-collider physics experiments". In: *Journal of Physics: Conference Series* 664 (Dec. 2015), p. 072053. DOI: 10.1088/1742-6596/664/7/072053.

[143] Xing-tao Huang, Teng Li, Jiaheng Zou, et al. "Offline Data Processing Software for the JUNO Experiment". In: (Feb. 2017), p. 1051. DOI: 10.22323/1.282.1051.

[144] J. Allison, K. Amako, J. Apostolakis, et al. "Recent developments in Geant4". In: *Nuclear Instruments and Methods in Physics Research Section A: Accelerators, Spectrometers, Detectors and Associated Equipment* 835 (2016), pp. 186–225. ISSN: 0168-9002. DOI: https://doi.org/10.1016/j.nima.

2016.06.125. URL: https://www.sciencedirect.com/science/article/pii/S0168900216306957.

[145] R. Brun and F. Rademakers. "ROOT: An object oriented data analysis framework". In: *Nucl. Instrum. Meth. A* 389 (1997). Ed. by M. Werlen and D. Perret-Gallix, pp. 81–86. DOI: 10.1016/S0168-9002(97)00048-X.

[146] C. Andreopoulos et al. "The GENIE Neutrino Monte Carlo Generator". In: *Nucl. Instrum. Meth. A* 614 (2010), pp. 87–104. DOI: 10.1016/j.nima.2009.12.009. arXiv: 0905.2517 [hep-ph].

[147] Minghua Liao, Kaixuan Huang, Yumei Zhang, et al. *A ROOT based detector geometry and event visualization system for JUNO-TAO*. 2024. arXiv: 2406.16431 [physics.ins-det]. URL: https://arxiv.org/abs/2406.16431.

[148] Adam Paszke, Sam Gross, Soumith Chintala, et al. "Automatic differentiation in PyTorch". In: (2017).

[149] A. Alekou, E. Baussan, A. K. Bhattacharyya, et al. "The European Spallation Source neutrino super-beam conceptual design report". In: *The European Physical Journal Special Topics* 231 (2022), pp. 3779–3955. DOI: 10.1140/epjs/s11734-022-00664-w.

[150] A. Alekou, E. Baussan, A. K. Bhattacharyya, et al. "The ESSnuSB Design Study: Overview and Future Prospects". In: *Universe* 9.8 (July 2023), p. 347. ISSN: 2218-1997. DOI: 10.3390/universe9080347. URL: http://dx.doi.org/10.3390/universe9080347.

[151] J. A. Formaggio and G. P. Zeller. "From eV to EeV: Neutrino cross sections across energy scales". In: *Reviews of Modern Physics* 84.3 (Sept. 2012), p. 1307. DOI: 10.1103/RevModPhys.84.1307.

[152] Stephen Parke. "Neutrinos: Theory and Phenomenology". In: (). P. O. Box 500, Batavia, IL 60510, USA. URL: https://arxiv.org/pdf/1310.5992.

[153] Peter B. Denton and Stephen J. Parke. "Simple and Precise Factorization of the Jarlskog Invariant for Neutrino Oscillations in Matter". In: FERMILAB-PUB-19-072-T (2019). arXiv: 1902.07185 [hep-ph]. URL: https://arxiv.org/abs/1902.07185.

[154] N. Nayak, M. Nebot-Guinot, L. Necib, et al. "Long-baseline neutrino oscillation physics potential of the DUNE experiment". In: *European Physical Journal C* 80.10 (2020), p. 978. DOI: 10.1140/epjc/s10052-020-08456-z. URL: https://link.springer.com/article/10.1140/epjc/s10052-020-08456-z.

[155] K. Abe and the Hyper-Kamiokande Proto-Collaboration. "Physics potentials with the second Hyper-Kamiokande detector in Korea". In: *PTEP* 2018.6 (2018), p. 063C01. DOI: 10.1093/ptep/pty044. URL: https://academic.oup.com/ptep/article/2018/6/063C01/5041972.

[156] Mauricio Bustamante and Amy Connolly. "The ultra-high-energy neutrino-nucleon cross section: measurement forecasts for an era of cosmic EeV-neutrino discovery". In: *Annual Review of Nuclear and Particle Science* 73 (2022), pp. 181–208. DOI: 10.1146/annurev-nucl-111422-040200.

[157] B. Gålnander, M. Eshraqi, C. Martins, et al. "Status of ESS Linac Upgrade Studies for ESSnuSB". In: *10th International Particle Accelerator Conference*. IPAC2019. 2019, pp. 1038–1041. DOI: 10.18429/JACoW-IPAC2019-MOPTS082. URL: https://inspirehep.net/files/75a13c59522b57c9b3db7fe14ef962bb.

[158] CERN Courier. *ESS under construction*. Accessed: [Insert Date]. 2020. URL: https://cerncourier.com/a/ess-under-construction/.

[159] Eric Baussan Tamer Tolba. "[ORCID]". In: *Physical Sciences Forum* 8.1 (2023). Presented at the 23rd International Workshop on Neutrinos from Accelerators, Salt Lake City, UT, USA, 30–31 July 2022, p. 57. DOI: 10.3390/psf2023008057.

[160] DEAP Development Team. *DEAP: Distributed Evolutionary Algorithms in Python*. Accessed: 2024-11-07. 2023. URL: https://pypi.org/project/deap/.

Declaration on oath

I hereby declare and affirm that this doctoral dissertation is my own work and that I have not used any aids and sources other than those indicated.

If electronic resources based on generative artificial intelligence (gAI) were used in the course of writing this dissertation, I confirm that my own work was the main and value-adding contribution and that complete documentation of all resources used is available in accordance with good scientific practice. I am responsible for any erroneous or distorted content, incorrect references, violations of data protection and copyright law or plagiarism that may have been generated by the gAI.

27.03.2025

Date

Signature of doctoral candidate